GAMMA-RAY BURST EARLY OPTICAL AFTERGLOW MODELLING

Richard Michael Harrison

A thesis submitted in partial fulfilment of the requirements of
Liverpool John Moores University
for the degree of
Doctor of Philosophy.
January 30, 2014

Declaration

The work presented in this thesis was carried out in the Astrophysics Research Institute, Liverpool John Moores University. Unless otherwise stated, it is the original work of the author.

Whilst registered as a candidate for the degree of Doctor of Philosophy, for which submission is now made, the author has not been registered as a candidate for any other award. This thesis has not been submitted in whole, or in part, for any other degree.

Richard Harrison
Astrophysics Research Institute
Liverpool John Moores University
IC2, Liverpool Science Park
Liverpool
L3 5RF
UK

October 2013

GAMMA-RAY BURST EARLY OPTICAL AFTERGLOW MODELLING

RICHARD HARRISON

Submitted for the Degree of Doctor of Philosophy

ASTROPHYSICS RESEARCH INSTITUTE

October 2013

Abstract

We discuss the evolution of a relativistic outflow responsible for producing the emission associated with GRBs. We investigate how afterglows are produced in the interaction between the outflow and the ambient medium. Understanding the properties of the outflow from afterglow emission can be coupled with information obtained from the prompt component to constrain the magnetisation of the outflow. We analytically and numerically evaluate the relative strength of the reverse shock emission as the outflow propagates into either a wind or ISM -type environment. We find that previous estimates of magnetisation based on the relative strength of forward and reverse shock emission had been underestimated by up to a factor of 100. We then apply our revised magnetisation estimate to a sample of 10 GRBs and find that 5 of the 10 events can be described by the ISM model. As recent studies have indicated that the fraction of energy stored in the magnetic fields are small, our findings would suggest that the ejecta is driven by thermal pressure. Finally we consider how inhomogeneities present in the outflow can lead to variations in the very early afterglow. Considering small gradient in the ejecta density profile modifies the rising index of the afterglow and can be equivalent to changing the dimensionless parameter ξ by a factor of 2. Uncertainties in determining the width of the ejecta present difficulties in understanding the distribution of GRBs afterglow rising index.

Publications

In the course of completing this thesis work, the contents of science chapters come from papers that are accepted and in preparation:

- Harrison, R. & Kobayashi, S. 2013, "Magnetization Degree of Gamma-Ray Burst Fireballs: Numerical Study" ApJ, 772, 101
- Harrison & Kobayashi "Magnetization Degree of a Reverse Shock Selected Sample of GRBS: Wind vs ISM External Density" in prep.
- Harrison & Kobayashi "Effect of Fireball Density Profile on Afterglow Evolution" in prep.
- Harrison & Kobayashi "Polarization in Early GRB Afterglows" in prep.

Additional work carried out during the PhD has lead to the inclusion on a number of research papers:

- Virgili, F.J. et al. (7^{th} author) "GRB 091024A and the Nature of Ultra-Long Gamma-Ray Bursts" accepted in ApJ, arXiv:1310.0313
- Guidorzi, C. et al. (3^{rd} author) "Constraints on GRB Jet Geometry and Relativistic Shock Physics" submitted to MNRAS.
- Japelj, J. et al. (5^{th} author) "In the Search for Reverse Shock Emission in GRBs: A Holy Grail?" in prep

- Maselli, A. et al. (37^{th} author) “GRB 130427A: a Nearby Ordinary Monster” submitted to Science.

- Mundell, C. et al. (7^{th} author) “Highly Polarized Light from Stable Ordered Magnetic Fields in GRB 120308A” submitted to Nature..

Acknowledgements

The success of this PhD could not have been achieved without the guidance and support of my supervisor Shiho Kobayashi. I would like to thank Ehud Nakar and Elena M. Rossi for useful discussion leading to the work presented in chapter 2, Hendrik van Eerten and Lucas Uhm for discussions related to chapter 4 of this thesis.

I would also like to thank Caterina for her support during my PhD, and Jdog et al. for making days in the office bearable. Without the aid of Phil James this work would be riddled with grammatical errors. However, in my defence I cannot help being born and raised in Ull. I also appreciate the services of the Soccerdome and the Stork for providing football and beer within a 10 minute walk of the department. There are many people, who have been at the ARI over the years I would like to thank, but my thesis is allowed only one page of acknowledgements. Bad luck!

“If the facts don’t fit the theory, change the facts.”

(probably not) Albert Einstein (1879 - 1955)

Contents

List of Tables

List of Figures

Chapter 1

Introduction

As implied by their names, gamma-ray bursts (GRBs) are short bursts of soft gamma-rays. These events can last from fractions of a second up to 10^4 seconds in the most extreme cases (Gendre et al. 2013). The equivalent isotropic energy associated with these events lie in the range $10^{52} - 10^{54}$ ergs. However we know that this energy is beamed, and the total gamma-ray energy released could be equivalent to the explosion energy of a supernovae (i.e. $10^{50} - 10^{51}$ ergs).

The gamma-ray component is known as the prompt emission. GRBs also have a longer lasting multi-wavelength afterglow component. Observations of the afterglow emission place stringent constraints on the position accuracy of the event. This allows association with the host galaxy, and therefore accurate distance determination via spectroscopy.

First I will discuss observational properties associated with GRBs followed by a detailed discussion of the fireball model, which has stood the test of observational GRB properties, and is the main focus of this thesis.

1.1 Prompt Component

The prompt component consists of the gamma-ray emission, along with any lower energy emission occurring simultaneously. In particular early X-ray emission is attributed to the low energy tail of the prompt emission, although X-ray emission generally also has a strong afterglow component.

The distribution of GRB durations span many orders of magnitude and are typically denoted by the value T_{90}, which corresponds to the observer time in which 90% of counts arrive from the GRB. During the BATSE era it became apparent that there were two distributions of GRB durations (Kouveliotou et al. 1993). The general consensus is that GRBs are classified as long if $T_{90} \geq 2$ seconds, although there is overlap between the two populations. GRBs with $T_{90} \leq 2$ seconds are called short GRBs. This separation can be seen in Figure 1.1. Given the large energies and short timescales associated with GRBs, it is likely that these events arise from the formation of a black hole via collapse of a massive star (Woosley et al 1993) or compact stellar merger such as neutron star- neutron star/black hole (Paczyński 1991; Narayan et al. 1992; Mochkovitch et al. 1993). The association of long bursts with collapse of a massive star is supported by GRBs being good tracers of star formation, and association with supernovae emission. From this arose the need for two progenitor types leading to the current idea that long bursts are associated with the collapse of a massive star and that short bursts come from the merger of compact stellar objects. This idea is supported by the observation of long GRBs associated with galaxies with strong star formation and potentially trace the star formation rate (e.g. Titani 1997; Wijers et al. 1998). Whereas short duration GRBs can be found in all galaxies including large ellipticals, strengthening the idea that long GRBs are associated with young stellar objects and short GRBs associated with longer lived stellar process. The association of short GRBs with a compact binary merger would be proved/disproved upon detection of such an event in gravitational waves. Here one would expect to detect the characteristic chirp associated with rapid rotation of two massive bodies as they coalesce.

Figure 1.2 (NASA/HEASARC image by J.T. Bonnell), shows an example sample of

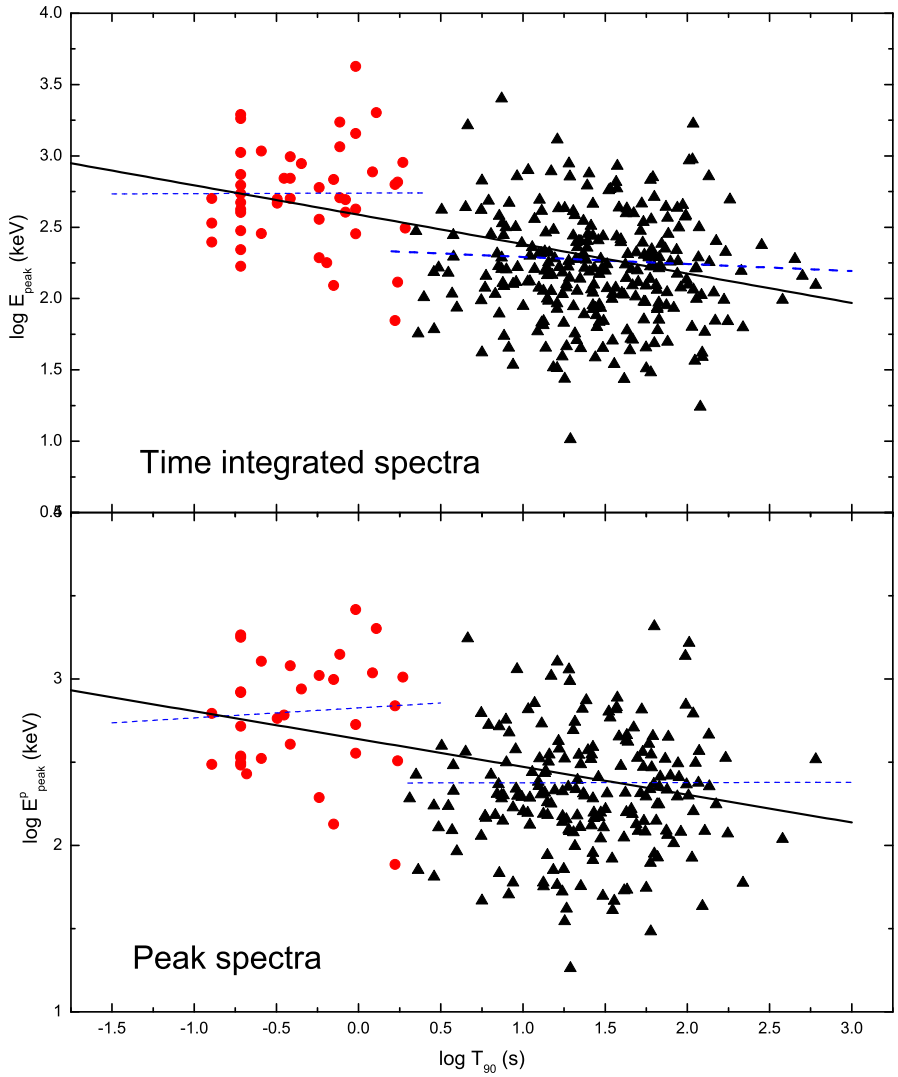

Figure 1.1: Correlations between integrated spectral peak energy and peak flux spectral peak energies with GRB duration (T_{90}). Black points represent long duration GRBs and red points denote short GRBs. Figure taken from Zhang et al. 2012.

GRB prompt light curves. As can be seen although a burst may be defined as long or short by T_{90}, it is still possible to have much shorter variability timescale depending on pulses generated during the central engine activity. Generally if no substructure is detected then the burst can be well described by a fast-rise exponential decay (FRED) form. It was shown by Fenmore & Ramirez-Ruiz (2000) that there was a correlation between the variability timescale (pulse width) and the luminosity. This was the first indication that a GRBs overall structure is built from the superposition of individual pulses.

The prompt spectrum is non thermal and also has a high energy tail that can extend up to GeV, with a peak energy in the keV-MeV range. The spectral shape is well approximated by a Band function (Band et al. 1993), with two separate power laws joined smoothly. We note here that the function is purely empirical and not predicted theoretically, although it does provide a useful parameterisation, such as the peak energy E_p. We see in Figure 1.1 that in terms of long and short GRBs, short GRBs tend to be harder (higher E_p) when compared to long GRBs. Individual pulses described in the previous paragraph show a hard to soft evolution with E_p decreasing across each pulse.

1.1.1 Compactness Problem

The relativistic nature of GRBs was first indicated by the compactness problem (Ruderman, M. 1975). Concerning the observed GRB we see a non-thermal spectrum with a high energy tail, however a simple calculation shows that the source should be optically thick. The GRB is seen to fluctuate on short timescales dt implying that the source is smaller than cdt. Given that we measure flux F over a timescale T at a distance D we can measure the arriving gamma-ray photon energy $E_\gamma \sim 4\pi D^2 FT$. Providing that the gamma-ray energy is above $2m_e c^2$, with m_e being the electron mass and c the speed of light, it is possible for two photons to annihilate producing electron-positron

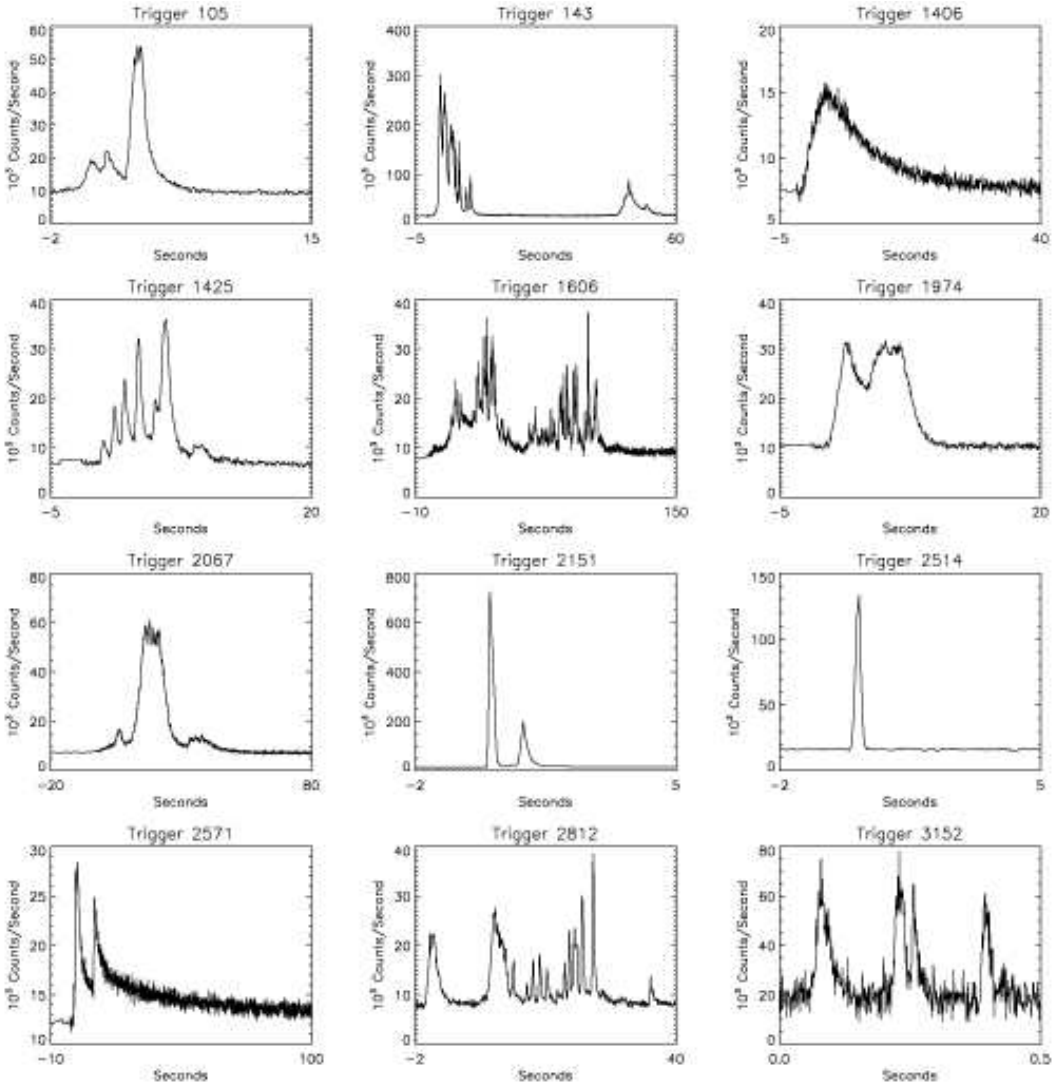

Figure 1.2: Here we show several GRB prompt light curves observed by BATSE demonstrating the variation in temporal evolution. Image by J.T. Bonnell NASA/HEASARC.

pairs. The optical depth for pair creation is given by

$$\tau_{\gamma\gamma} \sim \frac{f_{e\pm}\sigma_T D^2 F}{(cdt)^2 m_e c^2} \tag{1.1}$$

with σ_T is the Thompson cross section and $f_{e\pm}$ denoting the fraction of photon pair with energy sufficient to produce e^+e^- pairs. For a typical GRB the optical depth is very large $\tau_{\gamma\gamma} \sim 10^{15}$ (Piran, T. 1995), which is inconsistent with the observed non-thermal spectrum.

It is possible to solve this problem by considering that the photons are emitted by a relativistically expanding source. Let the Lorentz factor of the expansion be Γ_0 in the following discussion. First we need to account for photons being blue shifted, therefore the energy in the rest frame is smaller by a factor Γ_0. Relativistic effects allow the radius from which the radiation is emitted to be larger than the original estimate by a factor Γ_0^2. The first factor changes the collision probability, $f_{e\pm}$, by a factor $\Gamma_0^{-2\alpha}$, with α being the index of the photon energy number density distribution. The second factor decreases the density by Γ_0^4 and therefore decreases the optical depth by a factor Γ_0^2. In total the optical depth is decreased by a factor $\Gamma_0^{2+2\alpha}$. If we consider the case with $\alpha = 2$, then we require that $\Gamma_0 > 100$ for the source to be optically thin ($\tau_{\gamma\gamma} \leq 1$; e.g. Piran 2004).

Due to the fact we observe a non-thermal spectrum, the property that the source must be optically thin allows for constraints to be placed on the Lorentz factor of the emitting material. Accurate estimation requires integration over angular scales and the gamma-ray annihilation cross section. Such a calculation was performed by Lithwick and Sari (2001), improving on Equation 1.1.

1.2 Afterglow

The second emission component associated with a GRB is the multi-wavelength afterglow. The primary detection comes from the X-ray as Swift detects this afterglow component for most cases. There are traces of prompt signal at very early times (label

0, see Figure 1.3 for subsequent discussion). Generally after the prompt phase there is a steep decay region (I) although evidence indicates that this may not be part of the standard afterglow model (Zhang et al. 2006 and references therein). II and III show the shallow to normal transition where the emission evolves towards the standard afterglow decay of $t^{\sim -1}$. At later time there can be a further break (IV) due to a loss in flux from a jet break (this will be discussed later). The jet break is expected to be achromatic. It is possible to have flares (V) typically occurring hundreds of seconds after the burst trigger.

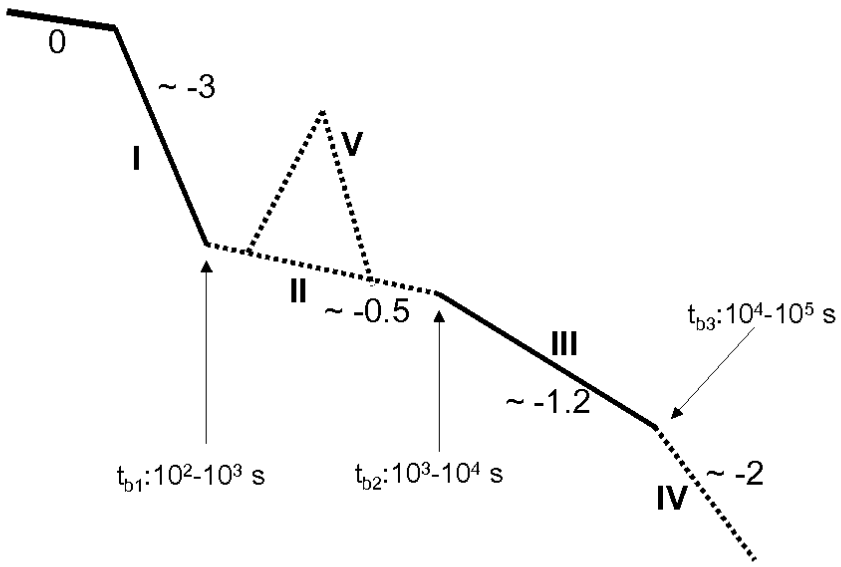

Figure 1.3: Figure from Zhang et al. (2006) showing the template for a canonical X-ray afterglow. See text for description of various phases. This light curve is shown in log-log space.

Around half of all GRBs also show afterglow emission at optical and IR wavelengths, although this is typically weaker and difficult to observe quickly and deep enough. Generally the emission is seen as a simple power law $t^{\sim -1}$ evolving to a steeper slope at later times due to the jet break. Occasionally optical flares are observed and in a

handful of cases an additional steep decay component at early times (different from the X-ray steep decay phase). This part of the afterglow can generally be seen for up to a few weeks after the trigger, at which point the afterglow becomes fainter than the host, although there are exceptions (e.g. Fruchter et al. 1998).

The final afterglow component we will consider is the radio band (typically observed at $5-8$ GHz). Given that the afterglow is generated via a synchrotron spectrum it takes time for the typical frequency to decay into the radio frequency range, meaning that it can generally be observed peaking roughly a week after trigger. The early radio flux can be dampened as the synchrotron self absorption features usually lie in this domain. As the radio emission is very long lived it is possible to even observe the transition from the outflow being relativistic to Newtonian, which can allow accurate calculation of energy in the ejecta.

1.3 Fireball Model

Given that evidence indicates that GRBs have very high Lorentz factors $\Gamma_0 >> 1$, this implies that the rest mass within the region of energy release is much smaller than the amount of energy ($Mc^2 = E/\Gamma_0$). This means that the region of energy release is radiation dominated rather than matter dominated, which is why we use the fireball model. The radiation-pair plasma in a purely radiative fireball that initially behaves as a fluid and expands/accelerates due to its high pressure (Cavallo & Rees 1978; Goodman 1986; Paczyński 1986). When the local temperature reaches ~ 20 keV, the system becomes optically thin and will continue to coast as internal energy has been converted to kinetic energy (Shemi & Piran 1990).

To interpret the different components of GRB emission, we use the fireball model. This does a good job of reproducing various features. The basic model goes as follows. Consider a hot fireball, surrounded by cold interstellar medium (ISM). The hot fireball ($p >> \rho$ with p being the pressure and ρ the density of the fireball) expands (Goodman 1986; Paczyński 1986; Shemi & Piran 1990) and internal energy is converted into

kinetic energy of the baryons. When the internal energy is used up, the fireball is no longer hot and acceleration stops. Although the fireball is homogeneous in the lab frame, relativistic transformation means the observer sees the system as a thin shell with width equal to the size of the initial fireball. The acceleration process does not create a perfectly homogeneous profile of the fireball. The leading edge travels slightly faster than the region immediately behind, and so on, such that the inner region is travelling the slowest (but is still ultra-relativistic). This will cause the fireball to spread at late times. If the fireball is highly irregular (e.g. formation of multiple shells), shocks happen inside the fireball and these are responsible for the prompt emission component (Kobayashi et al. 1997; Daigne & Mochkovitch 1998; Piran, T. 2005; Maxham & Zhang 2009; Vlasis et al. 2011).

At this stage we can consider the expanding uniform shell to be cold, as is the ISM (although this is much less dense). When the shell sweeps up mass equal to the mass of the outflow divided by the shell Lorentz factor (M/Γ_0), the ISM is sufficient to decelerate the system. When such a collision occurs it is known that two shocks form consisting of a forward shock (propagating into ISM) and reverse shock (propagating through fireball) separated by a contact discontinuity (Landau & Lifshitz 1959; Sari & Piran 1995; see also Figure 1.4).

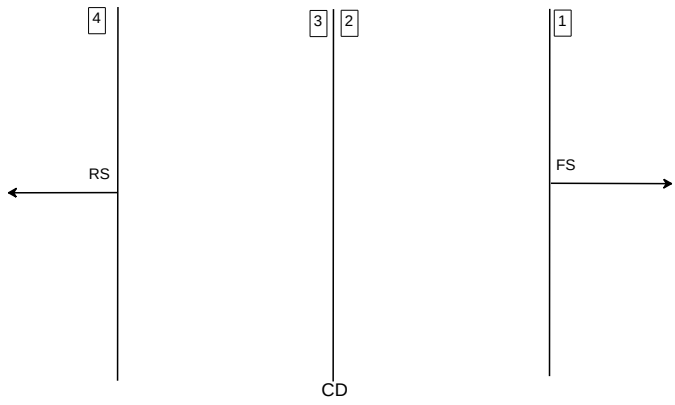

Figure 1.4: Here we show the four regions created when forward and reverse shocks form at a contact discontinuity.

As the reverse shock propagates through the shell we have four distinct regions: (1) the external medium (ISM), (2) shocked ISM region, (3) shocked shell and (4) unshocked shell, with three interfaces separating the different regions: (2)→(1) forward shock propagating into external medium, (3)→(4) reverse shock propagating into the shell and (3)↔(2) contact discontinuity separating the two shocked regions. The contact discontinuity represents the leading head of the shell.

At the interface between regions (2)→(1) and (3)→(4) we have conditions for continuity in particle number (n), momentum and energy flux densities[1].

$$[n^x] = [nu^x] = 0, \quad [T^{xx}] = [w(u^x)^2 + p] = 0, \quad c[T^{0x}] = c[wu^0u^x] = 0 \tag{1.2}$$

The gas moves in the x direction at right angles to the shock. T^{ik} is the energy-momentum tensor, u^i is the 4-velocity vector and w is the heat function per unit volume ($w = e + p$) and e is the internal energy. By substitution of 4-velocity components we arrive at the shock jump conditions for the rest frame of the shock,

$$\upsilon_1\gamma_1/V_1 \;=\; \upsilon_2\gamma_2/V_2 \;\equiv\; j, \tag{1.3}$$

$$w_1\upsilon_1^2\gamma_1^2/c^2 + p_1 \;=\; w_2\upsilon_2^2\gamma_2^2/c^2 + p_2, \tag{1.4}$$

$$w_1\upsilon_1\gamma_1^2 \;=\; w_2\upsilon_2\gamma_2^2, \tag{1.5}$$

υ is the velocity relative to the contact discontinuity, V is equivalent to density ($n = 1/V$) and γ is the Lorentz factor of the region ($\gamma = 1/\sqrt{1-\beta^2}$). Here we are considering the boundary (2)→(1) with the subscript denoting the region. The same argument can be carried forward for the other shock interface. The Lorentz factor of the shocked region (γ_2) is related to the bulk Lorentz factor of the system (Γ) by,

$$\Gamma^2 \;=\; \frac{(1-4\gamma_2^2)^2(\gamma_2^2-1)}{8\gamma_2^2 + 2\gamma_2 - 10} \tag{1.6}$$

Here it is important to note that in the ultra relativistic regime (i.e. when $\gamma_2 \gg 1$)

[1] Using the ultra-relativistic equation of state $p = e/3$

the equation simplifies to $\Gamma \approx \sqrt{2}\gamma_2$. If we consider the two shock boundaries and the above shock jump conditions (Equations 1.3-1.5) we arrive at relationships between the number and energy density on either side of the shock related by the relative Lorentz factor. This is achieved by considering a slab of material (2) travelling with velocity υ_2 into a low density medium ($1/V_1 \sim 1$). By conservation laws we arrive at Equations 1.7 and 1.8.

$$n_2/n_1 \;=\; 4\gamma_2 + 3 \;\cong\; 4\gamma_2, \quad e_2/n_2 m_p c^2 \;=\; \gamma_2 - 1 \;\cong\; \gamma_2, \tag{1.7}$$

$$n_3/n_4 \;=\; 4\bar{\gamma_3} + 3, \quad e_3/n_3 m_p c^2 \;=\; \bar{\gamma_3} - 1, \tag{1.8}$$

where $\bar{\gamma_3}$ is the Lorentz factor of the shocked shell material relative to the unshocked shell material and m_p being the proton.

Equating pressure and velocity across the contact discontinuity gives,

$$e_2 = e_3, \quad \bar{\gamma_3} = \frac{1}{2}\left(\frac{\gamma_2}{\gamma_4} + \frac{\gamma_4}{\gamma_2}\right) \tag{1.9}$$

completing the set of equations for hydrodynamic dependencies at shock fronts.

1.4 Synchrotron Emission

As we have discussed, it is possible to have two processes converting the kinetic energy of the outflow into internal energy. The prompt emission arises due to an inelastic collision of faster regions with slower regions, with the afterglow component arising due to shocks formed when the outflow interacts with the surrounding medium. If we assume that the outflow has magnetic fields (expected to be imprinted from the central black hole or generated by local instabilities) and contains electrons, then deceleration of the outflow will cause the electrons to radiate. The electrons (and other particles in the shocked region) are accelerated through a process called “Diffuse Shock Acceleration” also known as “Fermi Acceleration”. The electrons are accelerated each time they cross the shock and local magnetic fields cause them to scatter back and forth.

There is a probability that the electron will be scattered across the shock (gaining energy) and a probability that the electron will escape P_{esc} (Fermi 1949, 1954). This creates a power law spectrum of electrons with energy E, see Equation 1.10.

$$N(E)dE \propto E^{-\hat{p}}dE \tag{1.10}$$

As we have a highly relativistic system, more specifically, the electrons will emit via the synchrotron radiation. A thorough discussion of this process can be found in Rybicki & Lightmann (1979), which we will follow loosely here.

Consider a relativistic shock wave propagating through some medium of density n with particle number density ρ and internal energy density e. The electrons are assumed to be accelerated into power law distribution of Lorentz factors given by $Ne(\gamma)d\gamma \propto \gamma^{-\hat{p}}d\gamma$. The distribution has electrons in the range $\gamma_{min} \leq \gamma \leq \gamma_{max}$. This gives an energy distribution as roughly $(m_e c^2\gamma)N_e(\gamma)d\gamma \propto \gamma^{-(\hat{p}-1)}d\gamma$. If we consider that $\hat{p} > 2$ then most of the energy will be carried by electrons with $\gamma \sim \gamma_{min}$. Here the Lorentz factor is the random Lorentz factor of an electron. Let us consider that γ_e is the random Lorentz factor and γ is the bulk Lorentz factor.

If we consider that a constant fraction of the shock energy ϵ_e goes into the electrons, then

$$\gamma_m = \epsilon_e \frac{e}{\rho}\frac{m_p}{m_e}\frac{(\hat{p}-2)}{(\hat{p}-1)} \tag{1.11}$$

Taking the forward shock jump condition that $e/\rho \sim \gamma$ recovers the case discussed in Sari et al. (1998). The power and frequency of synchrotron emission from a randomly oriented electron in a magnetic field is

$$P(\gamma_e) = \frac{4}{3}\sigma_T c\gamma^2\gamma_e^2\frac{B^2}{8\pi} \tag{1.12}$$

$$\nu(\gamma_e) = \gamma\gamma_e^2\frac{q_e B}{2\pi m_e c}. \tag{1.13}$$

q_e is the electron charge. The bulk Lorentz factors γ^2 and γ transform from the shocked fluid frame quantities to the observer's frame. The spectral power varies as $P_\nu \propto \nu^{1/3}$ for $\nu < \nu\gamma_e$ and then cuts off exponentially for higher frequencies. Therefore the peak of this spectral power is

$$P_{\nu,max} = \frac{P(\gamma_e)}{\nu(\gamma_e)} = \frac{m_e c^2 \sigma_T}{3q_e}\gamma B. \tag{1.14}$$

Note that this value is independent of the electron Lorentz factor γ_e.

The number of electrons at a given γ_e is given by $N \sim \int N e_{\gamma_e} d\gamma_e \propto \gamma_e^{-(\hat{p}-1)}$, which has power (in the local shock frame, denoted by $'$) $P' = P(\gamma_e)/\gamma^2$. If we combine these two we get the total power of electrons NP'. We can then describe the power per unit frequency as

$$P'_{\nu'} = \frac{NP'}{\nu'} \propto \nu'^{-(\hat{p}-1)/2} \tag{1.15}$$

recovering the frequency dependencies of the spectral power around the frequency $\nu(\gamma_e)$ described in Sari et al. (1998). This is only the case when the electron does not lose a large amount of its energy to radiation. Electrons with a Lorentz factor above γ_c cool and lose energy, where $\gamma\gamma_c m_e c^2 = P(\gamma_c)t$.

$$\gamma_c = \frac{3m_e}{16\epsilon_B \sigma_T m_p c}\frac{1}{t_s \gamma^3 \rho} \tag{1.16}$$

t_s is the observer time since the electron was shocked and ϵ_B is the fraction of shock energy stored in magnetic fields, defined as

$$\frac{B^2}{8\pi} = \epsilon_B e m_p c^2. \tag{1.17}$$

We now have two cases, either $\gamma_m > \gamma_c$ and the electrons cool down to γ_c in time t_s and we have fast cooling. Alternatively $\gamma_c > \gamma_m$ and most of the electrons are not able

to cool within a time t. This thesis will primarily consider the final condition, as this is typical for GRBs.

1.5 Inverse Compton Process

An alternative process to synchrotron emission is the Inverse Compton (IC) process, especially the synchrotron self-inverse Compton process (e.g. Sari & Esin 2001). The inverse compton process takes low energy (seed) synchrotron photons that are up scattered to higher energies by relativistic electrons. The significance of the IC process depends on the comptonisation parameter, which is the ratio of energy in the synchrotron photons relative to that of magnetic fields (e.g. Rybicki & Lightman 1979). The issue with this model lies in the predicted prompt emission. Optical seed photons produce soft gamma ray emission from the first IC scattering and TeV photons on the second scattering. However, using the current upper limits on the prompt optical emission, the IC mechanism suffers from an ”energy crisis” (Piran et al. 2009). Namely, IC will overproduce a very high energy component that would carry much more energy than the observed prompt gamma-rays, or alternatively it will require a low-energy seed that is more energetic than the prompt gamma-rays.

1.6 Acceleration Process

It is thought that the central engine for a GRB is a hyper-accreting black-hole (Narayan et al. 1992; Narayan et al. 2001). A key question, that we address in this thesis, is what mechanism launches/accelerates the jet to relativistic velocities? There are two competing arguments, which we will outline and are still under contest. The distinction between the two processes is generally understood through the σ parameter (Michel 1969; Goldreich & Julian 1970), which is the ratio of magnetic (E_B) to kinetic (E_K) energy.

$$\sigma = \frac{E_B}{E_K} \tag{1.18}$$

If $\sigma \leq 0.1$ the outflow is considered to be baryonic however if $\sigma \geq 0.1$ the outflow should be highly magnetised, and the magnetic pressure affects the dynamics of the reverse shock in the outflow.

1.6.1 Baryonic Jet

We consider a purely baryonic jet, as described by the fireball model. At the beginning of the evolution the material is accelerated by its own thermal pressure due to the high temperatures. It is then possible to explain the prompt emission due to inhomogeneities in the Lorentz factors of different regions in the outflow. As these regions collide, shock waves propagate into both shells accelerating the electrons. These electrons then emit radiation via the synchrotron process which after Doppler boosting, is observed in the gamma-rays. Although this model is widely accepted, it has sources of uncertainty. The energy released via internal shocks is equivalent to the relative kinetic energy of the two shells (Kobayashi et al. 1997). However the observed radiation efficiency is very small (Kumar 1999; Panaitescu et al. 1999; Spada et al. 2000) and the prompt-gamma ray energy is generally equivalent to the kinetic energy of the afterglow.

1.6.2 Magnetised Jet

We have a rotating hyper-accreting black hole at the centre of our system. This black hole is threaded with strong ordered magnetic fields from magnetic flux conservation (Zhang & Mészáros 2004). In this case it is possible to launch an electromagnetic jet through the Blandford-Znajek effect (Blandford & Znajek 1977). This model requires that large scale ordered magnetic fields connect the black-hole to the external medium. Analysis of such models requires magnetohydrodynamical simulations (MHD) as analytical studies are confined to special cases such that equations can be simplified (e.g. asymptotic solutions or specific magnetic field geometries). As discussed earlier the

compactness problem requires that we have large Lorentz factors. For some time MHD processes struggled to accelerate material to sufficiently high velocities (McKinney, J. C. 2006), however recent advances have shown that MHD processes can achieve the high Lorentz factors required for GRBs (Tchekhovskoy et al. 2008; Barkov & Komissarov 2008). The jet is accelerated via magnetic pressure in the form of electromagnetically driven material (e.g. Poynting flux dominated flow). The advantage of using a Poynting flux flow comes from it being able to transport large amounts of energy without carrying many baryons. Under this paradigm the prompt emission component can arise due to magnetic reconnection within the jet. The magnetic field structure of the jet will be imprinted from the central engine i.e. large scale and ordered.

1.7 Two Components

As described in our simple fireball model we expect that the interaction of the outflow with the surrounding medium causes the formation of two shock waves, (1) a forward shock that propagates into the surrounding medium and (2) a reverse shock that propagates into the outflow. These two shock waves have different dependencies as they propagate through different regions.

1.7.1 Forward Shock

The pressure and density evolution of the forward shock region is given by the shock jump conditions in Equation 1.7. As the forward shock expands into the surrounding ISM the number of electrons constantly increases as,

$$N_{e,fs} = n_1 4\pi R^3 \tag{1.19}$$

It is possible to estimate the Lorentz factor at deceleration by considering the point where the forward shock sweeps up mass M/Γ_0, with M being the mass of the shell.

At this location,

$$\gamma_2 = \frac{1}{\sqrt{2}} \left(\frac{l}{R} \right)^{3/2} \tag{1.20}$$

with $l = (3E/4\pi m_p c^2 n_1)^{1/3}$ being the Sedov length.

1.7.2 Reverse Shock

From the shock jump conditions we obtain that the reverse shock pressure and density are given by Equations 1.8, and $\bar{\gamma_3}$ is a function of the initial Lorentz factor and the shocked region Lorentz factor (Equation 1.9). To calculate the reverse shock flux we estimate the density of the unshocked shell n_4 by taking the density from the shell of a sphere,

$$n_4 = \frac{E^3}{4\pi (m_p c^2)^3 \Gamma_0 \Delta R^2} \tag{1.21}$$

with Δ being the shell width and R the shock radius. We calculate the the number of electrons by considering the rate at which the reverse shock propagates through the shell. Let us consider the shell at two times, between which the reverse shock moves a short distance dr. The shell has leading edge velocity β_2 and trailing edge velocity β_4. By simple mass conservation we arrive at

$$\frac{dR}{c} \simeq \Gamma_0 f^{1/2} \frac{dr}{c} \tag{1.22}$$

with $f = n_4/n_1$ and r is the distance between the reverse shock location and contact discontinuity. The number of electrons is given by the integral of Equation 1.23

$$dNe_{rs} = n_4 4\pi R^2 dr \tag{1.23}$$

The reverse shock evolution can be described by two extremes, either relativistic or Newtonian evolution with respect to the unshocked shell region (Sari & Piran 1995; Kobayashi 2000). These regimes are known as the thick and thin shell cases respectively. The forward shock is always considered to be highly relativistic, $\gamma_2 >> 1$.

There is a dimensionless parameter ξ (Sari & Piran 1995), which gives a handle on the relativistic nature of the reverse shock

$$\xi = \left(\frac{l}{\Delta}\right)^{1/2} \Gamma_0^{-4/3} \tag{1.24}$$

$\xi << 1$ indicates a relativistic (thick shell) reverse shock and $\xi >> 1$ indicates Newtonian (thin shell) reverse shock evolution. The parameter depends on the order of the deceleration radius ($R_\gamma = l/\Gamma_0^{2/3}$), shell crossing radius ($R_\Delta = l^{3/4}\Delta^{1/4}$), spreading radius ($R_s = \Delta_0\Gamma_0^2$) and the point at which the reverse shock becomes relativistic ($R_N = l^{3/2}/\Delta^{1/2}\Gamma_0^2$).

Thick Shell

In the thick shell regime $\bar{\gamma_3} >> 1$, meaning the reverse shock is also highly relativistic in the comoving frame of the unshocked shell. After a single crossing of the shell the reverse shock efficiently transfers energy to the surrounding medium and decelerates the shell. Once the shell has been crossed no new electrons are injected, meaning there is no reverse shock emission above ν_c. This frequency simply decays with time due to adiabatic cooling. The various Lorentz factors are given by

$$\bar{\gamma_3} = \frac{\Gamma_0}{\sqrt{2}f^{1/4}}, \;\; \gamma_2 = \gamma_3 = \frac{\Gamma_0^{1/2} f^{1/4}}{\sqrt{2}} \tag{1.25}$$

Thin Shell

For the Newtonian (thin shell) case,

$$\bar{\gamma_3} - 1 << 1, \;\; \gamma_2 = \gamma_3 \sim \Gamma_0 \tag{1.26}$$

Here we have a weak reverse shock that is inefficient at decelerating the material and crosses the shell many times to decelerate the shell if the shell width is constant. During the outflow acceleration phase a slight velocity gradient is developed across the shell. This causes the shell to spread such that $\Delta \sim R/\Gamma_0^2$ at radius $R_s = \Delta\Gamma_0^2$. This effect

makes the reverse shock becomes mildly relativistic. A single passage of the reverse shock then efficiently decelerates the shell.

As the Newtonian or mildly relativistic reverse shock cannot heat the shell sufficiently to have a relativistic temperature the Blandford & McKee solution (Blandford & McKee 1976) fails. Kobayashi & Sari (2000) accounted for this by assuming a dependence $\gamma_3 \propto R^{-g}$ with adiabatic expansion ($p_3 \propto n_3$), and found that $g \sim 2$ fits the overall post-deceleration evolution well.

1.8 Polarisation

As GRBs are believed to be described by the synchrotron shock model (Zhang & Mészáros 2004; Piran 2005), the model requires the presence of strong magnetic fields, the origin of these fields and their role in jet dynamics are still unknown. Relativistic ejecta from a GRB central engine is conventionally assumed to be a baryonic jet, which produces synchrotron emission from tangled magnetic fields generated locally by instabilities in shocks (Gruzinov & Waxman 1999; Medvedev & Loeb 1999; Nishikawa et al. 2003; Spitkovsky 2008). An alternative model is a magnetised jet. It is expected to be threaded with globally ordered magnetic fields which originate at the central engine, and are advected outwards with the expanding flow. An attractive aspect of the magnetic model is that the intrinsic magnetic fields might provide a powerful mechanism for collimating and accelerating a relativistic jet (Drenkhahn & Spruit 2002; Lyutikov et al. 2003; Komissarov et al. 2009).

Since the late-time afterglow is emitted from shock ambient medium, rather than the original fireball ejecta, the properties of GRB outflows can be examined only through the investigations of emission internal to the jet e.g. prompt gamma-rays, reverse shock emission and radio or possibly X-ray flares (Granot & Taylor 2005; Lazzati &Rosalba 2007). The detection of high polarisation (Yonetoku et al. 2011) along with the putative detection of high degrees of polarisation in the prompt gamma-rays (Coburn & Boggs 2003; Willis et al. 2005; see however Rutledge & Fox 2004; Wigger et al.

2004; Gotz et al. 2009) has stimulated interest in the magnetised jet model (Granot 2003; Nakar et al. 2003).

The first detection of ten percent polarisation of an optical afterglow just 160 sec after the explosion of GRB 090102 (Steele et al. 2009) opens the exciting possibility of directly measuring the magnetic properties of the GRB flow. A new polarimeter, RINGO3 on the Liverpool telescope allows detection of a larger number of fainter bursts and can measure the temporal evolution of the polarisation degree and position angle of early optical afterglow. The instrument also provides the added ability to produce simultaneous multicolour light curves. Polarimetry is a powerful tool to break the degeneracy in predicted observational signatures of different models, which are indistinguishable from light curves alone (Rossi et al. 2004). Polarisation measurements with RINGO3 and other optical/X-ray polarimeters will provide stringent tests on the magnetic and geometric properties of GRB jets.

Reverse shock emission from magnetised fireballs is expected to be highly polarised. However, a distinctive reverse shock component is detected only in a small fraction of GRBs (Melandri et al. 2008). Several afterglows show a flattening in the light curves, interpreted as the signature of the rapid fading of reverse shock combined with the gradual dominance of forward shock emission (Akerlof et al. 1999; Sari & Piran 1999). Afterglow modelling of such flattening cases implies that the magnetic energy density in a fireball, expressed as a fraction of the equipartition value of shock energy, is much larger than in the forward shock (but it still suggests a baryonic jet rather than a Poynting-flux dominated jet: Fan et al. 2002; Zhang et al. 2003; Kumar & Panaitescu 2003; Gomboc et al. 2008). The lack of optical flashes in most GRBs may be due to either high magnetic energy densities that suppress the reverse shock (Gomboc et al. 2008; Mimica et al. 2009) or forward shock emission with a low typical frequency that masks the reverse shock components (Mundell et al. 2007).

Mildly polarised emission would arise even in baryonic fireballs which generate random magnetic fields locally via shock instabilities. A possible scenario is that the coherence length of the magnetic fields could grow at about the speed of light in the local fluid frame. In this situation, polarised radiation would come from a number

of independent ordered magnetic field patches (Gruzinov & Waxman 1999). Another possibility is off-axis emission from a jet (Gruzinov 1999; Covino et al. 1999; Wijers et al. 1999; Waxman 2003; Fan et al. 2008). Since a part of the observable region around a line of sight is located outside the jet opening angle, the net polarisation would have a non-zero value. The optimal geometrical configuration is known for maximal polarisation occurs around a jet break (Sari 1999; Ghisellini & Lazzati 1999). Recent work by Wiersema et al (2012) provide evidence for this mechanism. Asymmetry around the line of sight also occurs in the structured jet model, in which GRB jets have angular structures in the energy and/or Lorentz factor distribution (Mészáros et al. 1999; Rossi et al. 2002, 2004; Zhang & Mészáros 2002). Since the Lorentz factor of fireball ejecta is insensitive to the initial value after the deceleration (e.g. Kobayashi et al. 1999), the initial Lorentz factor is not well constrained from late-time observations. Early polarisation measurements provide a constraint on the angular distribution of the initial Lorentz factor.

1.9 Additional Influences

1.9.1 Density Profile of Outflow and Ambient Medium

Rather than expanding into a homogeneous external medium the wind model $n_1 \propto R^{-2}$ is often discussed (Chevalier & Li 2000) with the medium generated by the progenitor star (Woosley 1993). We can follow through the standard afterglow theory described above and arrive at a new set of equations with dependencies on $\bar{p}$ and how relativistic the fireball is ξ. The general influence of a wind medium on the afterglow causes emission to become temporally steeper in the forward and reverse shocks after deceleration. Pre-deceleration emission is shallower/steeper in the thick/thin shell cases respectively. Work carried out by Heaton & Kobayashi (in prep), allows the generalisation of reverse shock emission considering a wind medium for varying ξ by using numerical simulations.

An alternative considration could be that the fireball itself has some non-uniform den-

sity profile $n_4 \propto R^{-2} r^n$. This will be the focus of Chapter 4 of this thesis.

1.9.2 Energy Injection

Classically, we assume that a relativistic shell of energy E, Lorentz factor Γ_0 and width Δ propagates into an external medium of density n_1. After the shell has swept up a large amount of the external medium, it decelerates and transfers kinetic energy into the surrounding medium through the generation of forward and reverse shocks (see Piran 2004 for a recent review). In the simple model the shell has a homogeneous velocity distribution. Instead, let us consider that the central engine initially ejects material with a range of Lorentz factors, such that when the fastest material decelerates, the slower moving material is able to catch up and supply additional energy. This profile in velocity space appears as a slope rather than the usual homogeneous distribution leading to the "refreshed" shock scenario (Rees & Mészáros 1998; Kumar & Piran 2000; Sari & Mészáros 2000; Zhang & Mészáros 2001; Genet et al. 2007). We follow the energy injection model presented by Sari & Mészáros (2000), such that there is mass $M(>\gamma) \propto \gamma^{-s}$ moving with Lorentz factor greater than γ. For a given burst, energy injection might occur until the central engine switches off at some time t_{inj}. In this case the total energy emitted is

$$E = E_{iso} = (t_{inj}/t_{dec})^{\frac{3(s-1)}{7+s}}. \tag{1.27}$$

Here $E_{iso,52}$ being the isotropic energy, t_{dec} is the deceleration time of the fireball and we have assumed that the fireball is expanding into an ISM type medium ($n_1 \sim$constant). It is then possible to estimate the spectral evolution of the forward shock (denoted by f),

$$\nu_{m,f} = 8 \times 10^9 (1+z)^{1/2} \epsilon_{B,-4}^{1/2} \epsilon_{e,-2} E_{52}^{1/2} t_{day}^{-3/2} \left(\frac{t}{t_{dec}}\right)^{\frac{3(s-1)}{2(7+s)}} Hz \tag{1.28}$$

$$F_{\nu,max,f} = 0.26(1+z) \epsilon_{B,-4}^{1/2} E_{52} n_0^{1/2} D_{28}^{-2} \left(\frac{t}{t_{dec}}\right)^{\frac{3(s-1)}{(7+s)}} mJy \tag{1.29}$$

ϵ_e and ϵ_B are the microphysical parameters denoting the fraction of energy stored in the electrons and magnetic field respectively. Throughout this thesis we will adopt the notation $A_X = A/10^X$. The reverse shock component is then given by

$$\nu_{m,r} = 3.6 \times 10^7 (1+z)^{-1/4} \epsilon_{B,-4}^{1/2} \epsilon_{e,-2}^{2} E_{52}^{1/4} n_0^{1/4} t_{day}^{-3/4} \left(\frac{t}{t_{dec}} \right)^{\frac{3(s-1)}{4(7+s)}} Hz \tag{1.30}$$

$$F_{\nu,max,r} = 1.2(1+z)^{11/8} \epsilon_{B,-4}^{1/2} E_{52}^{9/8} n_0^{3/8} D_{28}^{-2} t_{day}^{-3/8} \left(\frac{t}{t_{dec}} \right)^{\frac{27(s-1)}{8(7+s)}} mJy \tag{1.31}$$

1.9.3 Jet Break

In many GRB afterglows, at late times an achromatic break is seen (Rhoads 1999; Sari et al. 1999). If we consider that the cone of the relativistic jet launched by the central engine has finite size given by θ_{jet} then the observed light curve is dependent on the angle between the line of sight and the jet axis, along with the initial Lorentz factor. We can easily show, owing to Doppler boosting, that the angular size of the observable region surrounding the line of sight is given by $\theta \simeq 1/\gamma$. As the fireball decelerates we have $\gamma \propto t^{-3/8}$ such that the observable region expands as $\theta \propto t^{3/8}$. For simplicity we might take the jet to have a homogeneous structure such that all regions contribute equal flux. However at some point, as θ grows, we will reach the edge of the jet. From this point on the observable region loses a fraction of flux due to the boundary of the jet, causing the afterglow emission to steepen. Sari et al. (1999) show that from the break time (t_{jet}) it is possible to estimate the jet opening angle (see Equation 1.32).

$$\theta_j = 11.4 \left(\frac{t_{jet}}{1+z} \right)^{3/8} \left(\frac{n_0 \eta}{E_{iso,52}} \right)^{1/8} rad, \tag{1.32}$$

t_{jet} given in seconds and η giving the GRB efficiency. An extension of this system is to consider that the jet has some structure, where the kinetic energy and Lorentz factor have some angular dependence (e.g. Rossi et al. 2004). In this case we expect to see a somewhat softer break in the afterglow, however the break would still be achromatic. There have been no clear jet breaks observed during the Swift era (Racusin et al. 2009;

Cenko et al. 2010).

1.10 Optical Follow-up with the Liverpool Telescope

The Liverpool Telescope (LT) is a robotic 2m class Cassegrain telescope, which has been used to pioneer early optical detections of GRB afterglows. Along with the standard optical follow up capabilities, the LT has had a unique family of polarimeters fitted RINGO, RINGO2 and RINGO3 (Steele et al. 2006; Arnold et al. 2012). The most recent generation (RINGO3) is of unique design and consist of two dichroics that split the light into three passbands for simultaneous colour measurements. These are beamed onto three fast readout CCD cameras that take 8 exposures per second. Before the dichroics there is a rotating polaroid that rotates synchronously with the CCD readout ($8\times$ per second) to allow for polarisation detections (see Figure 1.5). This polarised emission is important in understanding the magnetic structure of the GRB outflow (e.g. Lazzati et al. 2004). The detection of early polarised emission is important as at early times we can still detect emission originating from internal process (e.g. reverse and prompt emission) which tells us about the magnetic field structure of the fireball. Late time polarimetry of forward shock emission provides insight into the magnetic field structure of the surrounding circumburst medium.

The LT is part of a larger group of robotic telescopes such as the Faulkes Telescopes North and South that help us to observe the full afterglow phase, due to the spread in observatory longitudes. This invaluable resource has lead to the development of this thesis to allow better understanding of early afterglow evolution, specifically refining what information can be extracted based on optical afterglows.

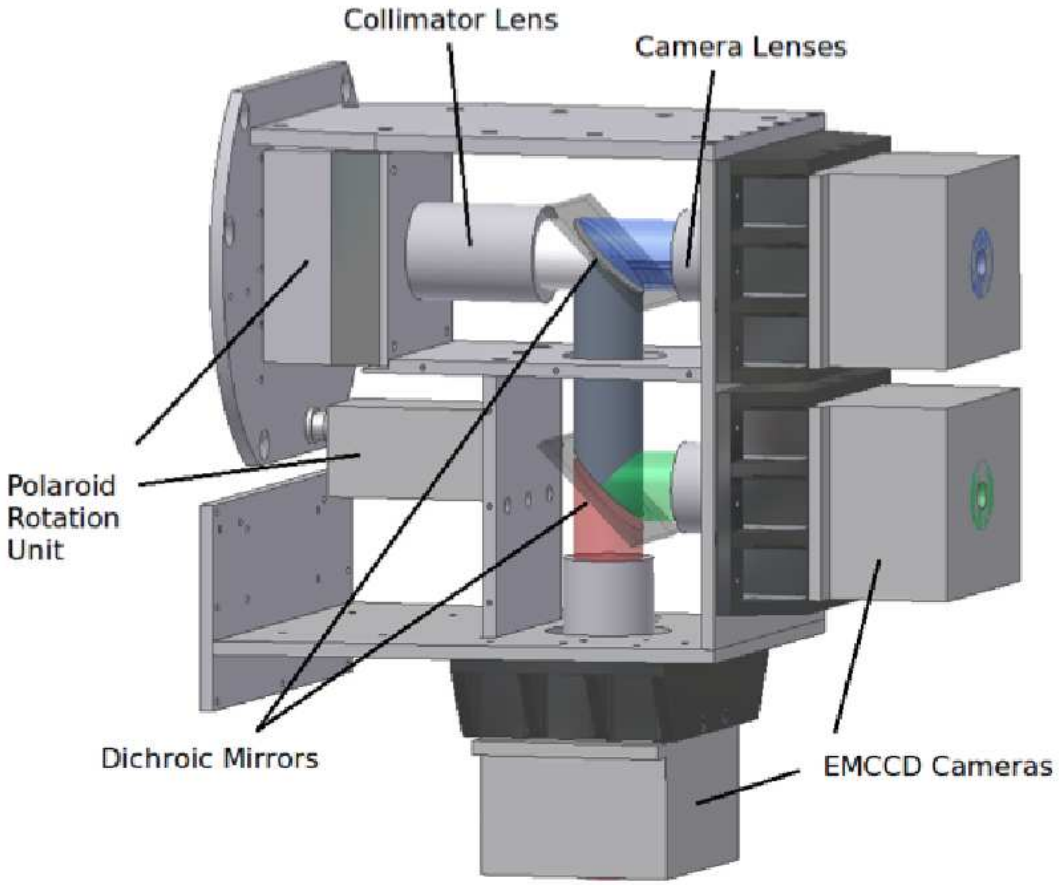

Figure 1.5: Here we see a schematic for the polarimeter RINGO3 described in the text.

The main goal of this thesis is to understand the energy content of the ejecta, whether the outflow can be described by the baryonic or magnetic scenario. This is understood by investigating the relative magnetisation between forward and reverse shock regions. Although this work has been carried out before (Zhang et al. 2003; Kobayashi & Zhang 2003), it has only been understood in the limits of reverse shock evolution. Here we focus on the intermediate regime where most observed GRBs reside and it has been shown that extension of the extreme limits fail (Nakar & Piran 2004). Coupling work on afterglow magnetisation estimates with polarisation measurements of GRB afterglows will allow the issue of the outflow energy content to be resolved.

Chapter 2

Magnetisation Degree of Gamma-Ray Burst Fireballs: Numerical Study

2.1 Introduction

A widely accepted model for producing GRBs is based on the dissipation of a relativistic outflow (e.g. Piran 2004; Zhang & Mészáros 2004). The internal energy produced by shocks is believed to be radiated via synchrotron emission. Although the presence of strong magnetic fields is crucial in the model, their origin and role in the dynamics are still unknown. Understanding the nature of the relativistic outflow, especially the energy content, acceleration and collimation, is a major focus of international theoretical and observational efforts.

Relativistic outflow from a GRB central engine is conventionally assumed to be a baryonic jet, producing synchrotron emission with tangled magnetic fields generated locally by instabilities in shocks (Medvedev & Loeb 1999; Nishikawa et al. 2005; Spitkovsky 2008). Recently an alternative magnetic model has attracted attention from researchers (e.g. Drenkhahn & Spruit 2002; Fan et al. 2004; Zhang & Kobayashi 2005; Lyutikov 2006; Giannios 2008; Mimica et al. 2009, 2010; Zhang & Pe'er 2009; Zhang & Yan 2011; Narayan et al. 2011; Granot 2012). The rotation of a black hole and

an accretion disk might cause a helical outgoing Magnetohydrodynamic (MHD) wave which accelerates material frozen into the field lines (Tchekhovskoy et al. 2008; McKinney & Blandford 2009; Komissarov et al. 2009). In the magnetic model, a fireball is expected to be endowed with primordial magnetic fields from the central engine.

The first detection of ten percent polarisation of an optical afterglow just 160 sec after the GRB explosion (Steele et al. 2009) opens the exciting possibility of directly measuring the magnetic properties of the GRB outflow. Recently polarisation measurements of the prompt gamma-ray emission were also reported (Kalemci et al. 2007; McGlynn et al. 2007; Götz et al. 2009; Yonetoku et al. 2011). Although these polarisation measurements suggest that at least some GRB outflows contain ordered magnetic fields and they are still baryonic, the sample is small and further observations will be necessary to confirm the magnetic model and/or to understand the role of magnetic fields in the dynamics. In this chapter, we revisit the magnetisation estimate of the GRB outflow (hereafter "fireball") based on photometric observations of early optical afterglow. It is more sensitive to the magnetic energy density, rather than the length scale of magnetic fields in the fireball, and it is complementary to polarimetric methods (e.g. Lazzati 2006; Toma et al. 2009).

A steep decay in early optical afterglow light curves is usually considered as a signature of the reverse shock emission (e.g. Akerlof et al.1999; Sari & Piran 1999; Meszaros & Rees 1999; Soderberg & Ramirez-Ruiz 2002; Li et al. 2003; Fox et al. 2003; Nakar & Piran 2005). The early emission contains precious information on the original ejecta from the central engine. The magnetisation of the fireball can be evaluated by using the relative strength of the forward and reverse shock emission (Fan et al. 2002, 2005; Zhang et al. 2003; Kumar & Panaitescu 2003; Gomboc et al. 2008). However, the standard method uses a simplified shock dynamics model, and Nakar & Piran (2004) have shown it is inaccurate in the intermediate regime between the thin and thick shell extremes. Since most observed events are in the intermediate regime, here we numerically re-examine the interplay between the forward and reverse shock emission at the onset of afterglow. In Section 2.2 we set out a simple conventional approach to understanding the two shock emissions and refine the definition of the magnetisation

parameter in Section 2.3. In Section 2.4 we consider a new approximation to discuss the reverse shock emission in the intermediate regime. In Section 2.5, we test these analytic approximations with numerical simulations. In Section 2.6 we present case studies of GRB 990123 and 090102 in terms of the magnetisation parameter. Finally in Section 2.7 we summarise the results.

2.2 Forward and Reverse Shock

We consider a homogeneous fireball [1] of energy E and a baryonic load of total mass M confined initially in a sphere of radius r_0. We define the dimensionless entropy $\Gamma_0 \equiv E/Mc^2 \gg 1$. This fireball expands into a homogeneous interstellar medium (ISM) of particle density n_1. This can be considered to be a free expansion in its initial stage. After a short acceleration phase, the motion becomes highly relativistic, and a narrow shell is formed. After the fireball shell uses up all its internal energy, it coasts with a Lorentz factor of Γ_0 and the radial width $\Delta_0 \sim r_0$.

The deceleration process of the shell is described with two shocks: a forward shock propagating into the ISM and a reverse shock propagating into the shell. The forward shock is always ultra-relativistic, while the evolution of the reverse shock is determined by a dimensionless parameter $\xi_0 = (l/\Delta_0)^{1/2}\Gamma_0^{-4/3}$ where $l = (3E/4\pi m_p n_1 c^2)^{1/3}$ is the Sedov length and m_p is the proton mass. If $\xi_0 < 1$ (so called thick shell case), the reverse shock becomes relativistic in the frame of the unshocked shell material and it drastically decelerates the shell. If $\xi_0 > 1$ (thin shell case), the reverse shock is inefficient at slowing down the shell. The deceleration radius r_d and the Lorentz factor Γ_d of the shocked material at r_d are usually approximated as $r_d \sim l^{3/4}\Delta_0^{1/4}$ and $\Gamma_d \sim (l/\Delta_0)^{3/8}$ for $\xi_0 < 1$, and $r_d \sim l/\Gamma_0^{2/3}$ and $\Gamma_d \sim \Gamma_0$ for $\xi_0 > 1$ (Sari and Piran 1995; Kobayashi et al. 1999). After the deceleration, the profile of the shocked ISM

[1] Since we assume that magnetic fields in the fireball do not affect the reverse shock dynamics, our magnetisation estimates are valid only when the fireball is weakly magnetised. The model consistency will be checked later when our results are applied to specific events (see Section 2.6). Because of the relativistic beaming effect, the radiation from a jet before the jet break can be described by a spherical model.

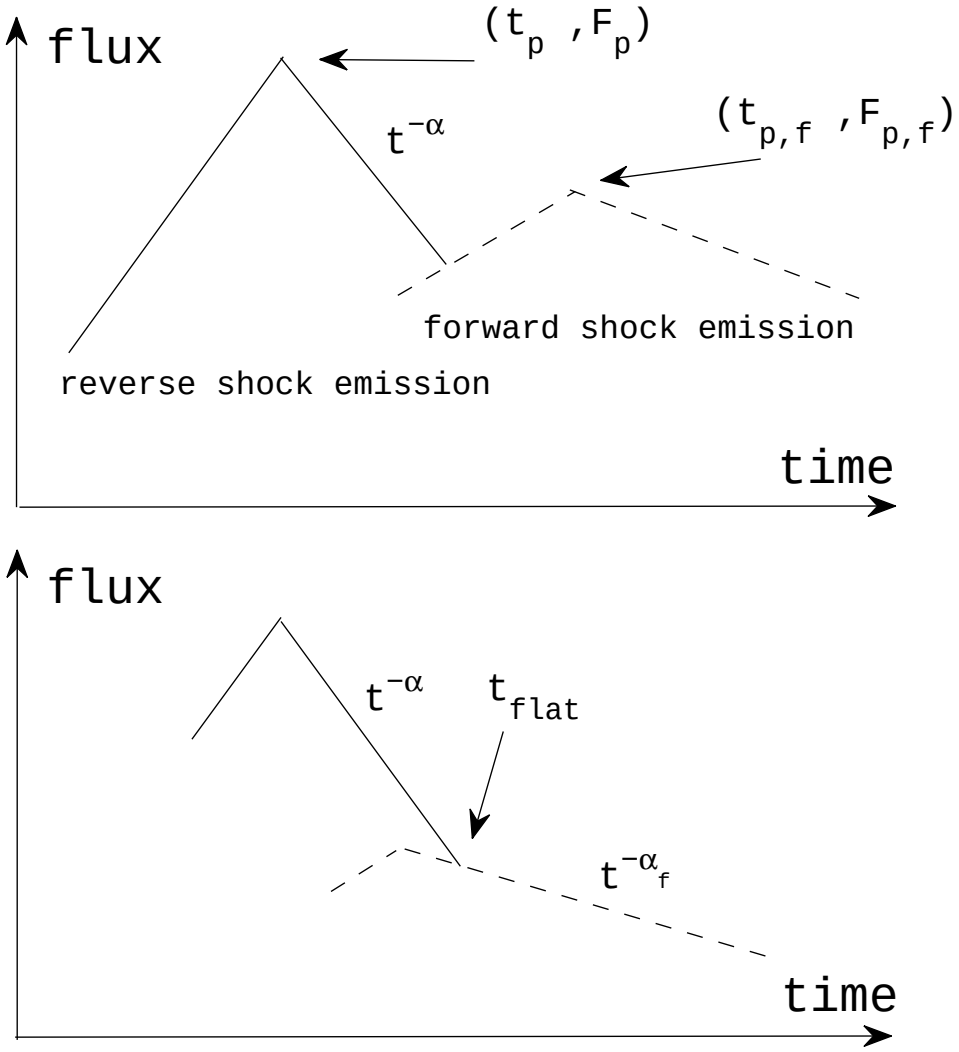

Figure 2.1: Early steep decay: optical afterglow, produced as a composition of the reverse shock emission (solid line) and forward shock emission (dashed line). Two peaks (top panel) and a flattening (bottom panel) can occur in the light curve.

medium begins to approach the Blandford & McKee (1977) solution.

We first discuss the forward and reverse shock emission by using these conventional estimates, and the accuracy (i.e. correction factors) will be numerically examined later. The deceleration of a shell happens at an observer time

$$t_d = C_t \frac{l}{c\Gamma_0^{8/3}}, \tag{2.1}$$

where $C_t \sim (\Gamma_d/\Gamma_0)^{-8/3} \sim \max(1, \xi_0^{-2})$ and all the correction factors in this chapter, including C_t, are defined as ones relative to the conventional thin shell estimates. At the deceleration time, the forward and reverse shock regions have almost the same Lorentz factor and internal energy density. However, the reverse shock region has a much larger mass density and therefore it has a lower temperature. Introducing a magnetisation parameter $R_B \equiv \epsilon_{B,r}/\epsilon_{B,f}$, it is shown that the typical frequencies ν_m and peak fluxes $F_{\nu,max}$ of the synchrotron emissions from the two shocks are related as

$$\frac{\nu_{m,r}(t_d)}{\nu_{m,f}(t_d)} = C_m \Gamma_0^{-2} R_B^{1/2}, \quad \frac{F_{\nu,max,r}(t_d)}{F_{\nu,max,f}} = C_F \Gamma_0 R_B^{1/2}, \tag{2.2}$$

(Kobayashi & Zhang 2003; Zhang et al. 2003) where $C_m \sim (\Gamma_d/\Gamma_0)^{-4} \sim \max(1, \xi_0^{-3})$ and $C_F \sim (\Gamma_d/\Gamma_0)^2 \sim \min(1, \xi_0^{3/2})$ are correction factors, the subscripts r and f indicate reverse and forward shock, respectively. We have assumed that the electron equipartition parameter ϵ_e and the electron power-law index $\hat{p}$ are the same for the two shock regions, but with different magnetic equipartition parameter ϵ_B as parametrised by R_B. The reason we introduce the R_B parameter is that the fireball might be endowed with primordial magnetic fields from the central engine. We can give a simple relation $\nu_{c,r}/\nu_{c,f} \sim R_B^{-3/2}$ between the cooling break frequencies of the two shock emissions (Zhang et al. 2003). As we will see in the next section, this simple estimate is good enough for the magnetisation estimate.

2.3 Magnetisation Estimates

For no or moderate primordial magnetic fields in a fireball [2], we expect $\nu_{m,r} \ll \nu_{m,f}$ and $\nu_{c,r} \lesssim \nu_{c,f}$ at the peak time of the reverse shock emission $t_p \sim t_d$. The optical band ν_{opt} should satisfy a relation $\nu_{m,r} < \nu_{opt} < \nu_{c,r}$ during the early steep decay phase of the reverse shock emission. Otherwise the decay is much slower or faster than the typical decay t^{-2} (Kobayashi 2000). There are four possible relations between the break frequencies and the optical band at the peak time t_p: (a) $\nu_{m,r} < \nu_{opt} < \nu_{m,f} < \nu_{c,r} < \nu_{c,f}$, (b) $\nu_{m,r} < \nu_{opt} < \nu_{c,r} < \nu_{m,f} < \nu_{c,f}$, (c) $\nu_{m,r} < \nu_{opt} < \nu_{c,r} < \nu_{c,f} < \nu_{m,f}$, and (d) $\nu_{m,r} < \nu_{m,f} < \nu_{opt} < \nu_{c,r} < \nu_{c,f}$. In the cases (a) and (b), the forward shock emission peaks at $t_{p,f}$ when the typical frequency $\nu_{m,f}$ goes through the optical band (the top panel in Figure 2.1). Using $\nu_{m,f} \propto t^{-3/2}$, we get the peak time and peak flux ratio

$$R_t \equiv t_{p,f}/t_p = (\nu_{m,f}(t_p)/\nu_{opt})^{2/3}, \tag{2.3}$$

$$R_F \equiv F_p/F_{p,f} = (F_{\nu,max,r}(t_p)/F_{\nu,max,f})(\nu_{opt}/\nu_{m,r}(t_p))^{-(\hat{p}-1)/2} \tag{2.4}$$

where F_p and $F_{p,f}$ are optical peaks in the time domain, while $F_{\nu,max,r}$ and $F_{\nu,max,f}$ are peaks in the spectral domain for a given time. The hydrodynamical evolution of a reverse shocked shell is investigated in Kobayashi & Sari (2000), and the decay index $\alpha \sim (3\hat{p}+1)/4 \sim 2$ of the reverse shock emission is found to be almost independent of ξ_0 when $\nu_{m,r} < \nu_{opt} < \nu_{c,r}$. Combining Equations 2.2, 2.3 and 2.4, we obtain

$$R_B = \left(\frac{R_F^3 \Gamma_0^{4\alpha-7}}{C_F^3 C_m^{2(\alpha-1)} R_t^{3(\alpha-1)}}\right)^{2/(2\alpha+1)} \sim \left(\frac{R_F^3 \Gamma_0}{C_F^3 C_m^2 R_t^3}\right)^{2/5}. \tag{2.5}$$

(Gomboc et al. 2008). At this stage, we assume that Γ_0 is a known quantity, and we will discuss how to estimate Γ_0 from early afterglow observations in Section 2.5.3. In the case (c), if the forward shock emission makes a transition from the fast cooling to

[2] Even if ϵ_B at the forward shock is very low (e.g. $\epsilon_{B,f} \sim 10^{-5}$; Kumar & Barniol Duran 2009), we expect the typical frequency of the reverse shock emission to be much lower than that of the forward shock emission $\nu_{m,r} \ll \nu_{m,f}$. For typical events ($\Gamma_0 > 10^2$ and $C_m \sim 1$), extreme magnetisation $R_B \sim \Gamma_0^4 > 10^8$ is needed to achieve $\nu_{m,r} \sim \nu_{m,f}$ at the peak time.

the slow cooling regime before it peaks, it becomes equivalent to the case (b). The Equation 2.5 is valid. On the other hand, if it is still in the fast cooling regime when $\nu_{c,f}$ crosses the optical band, the forward shock emission rises and decays very slowly as $t^{1/6}$ and $t^{-1/4}$ (Sari et al. 1998). Since this behaviour is not consistent with most early afterglows, we do not discuss the details [3]. Finally, in the case (d), the forward shock emission also peaks at the onset of afterglow, and it follows that $R_t = 1$. It is possible to show that Equation 2.5 is still valid.

When an early afterglow light curve shows a flattening at $t = t_{flat}$ after the steep decay phase (the bottom panel in Figure 2.1), the reverse shock emission dominates at early times. The forward shock peak is masked by the reverse shock emission, and the peak ($t_{p,f}$, $F_{p,f}$) is not observationally determined. In such a case, the upper limit $t_{p,f} = t_{flat}$ gives a rough estimate of R_B. Considering that the reverse and forward shock emission components are comparable at the flattening, we obtain $R_F \sim R_t^{\alpha}$. Substituting this relation into Equation 2.5, we get

$$R_B \sim \left(\frac{R_t^3 \Gamma_0^{4\alpha-7}}{C_F^3 C_m^{2(\alpha-1)}} \right)^{2/(2\alpha+1)} \sim \left(\frac{R_t^3 \Gamma_0}{C_F^3 C_m^2} \right)^{2/5} . \tag{2.6}$$

where $R_t = t_{flat}/t_p$. If the forward shock emission peaks earlier $t_{p,f} < t_{flat}$, the real value of R_B might be slightly different. To evaluate how R_B depends on $t_{p,f}$, we refer to the scalings $R_t \propto t_{p,f}$ and $R_F \propto t_{p,f}^{\alpha_f}$ where α_f is the decay index of the forward shock emission. Using these scalings, one finds that the dependence is weak: $R_B \propto t_{p,f}^{6(1+\alpha_f-\alpha)/(1+2\alpha)}$. If the forward shock decays as the theory suggests then $\alpha_f = 3(\hat{p}-1)/4$, a relation $1+\alpha_f - \alpha = 0$ holds, and R_B does not depend on $t_{p,f}$ (Gomboc et al. 2008).

For weakly magnetised fireballs, the ratio σ between the Poynting flux energy and the kinetic energy (the baryonic component) around t_p is expressed as a function of the

[3] In this case, we need an additional relation $\nu_{m,f}(t_p)/\nu_{c,f}(t_p) = (\gamma_m/\gamma_c)^2 \propto (\epsilon_e \epsilon_{B,r} \Gamma_d^4 t_p n_1)^2$ for the magnetisation estimate where γ_m and γ_c are the random Lorentz factors of electrons corresponding to the typical and cooling break frequencies, respectively.

magnetisation parameter R_B as

$$\sigma \sim \left(\frac{\bar{\Gamma}_d - 1}{\bar{\Gamma}_d} \right) \epsilon_{B,f} R_B, \tag{2.7}$$

where $\bar{\Gamma}_d$ is the Lorentz factor of shocked shell material relative to the unshocked shell.

2.4 Shocks in the intermediate regime

The simple estimates of r_d and Γ_d, which we have discussed in Section 2.2, provide useful insights into the fireball dynamics. However, these are order-of-magnitude estimates, and obtained by assuming that the reverse shock is ultra-relativistic or Newtonian. Since most observed bursts are actually in the intermediate regime $\xi_0 \sim 1$, we here consider a better approximation which is similar to one discussed by Nakar & Piran (2004).

The deceleration of an expanding shell happens when it gives a significant fraction of the kinetic energy to the ambient medium. Equating the energy in the shock ambient matter with $E/2$, we obtain $r_d = 2^{-1/3} l/\Gamma_d^{2/3}$. The Lorentz factor Γ_d in the shock regions is given as a function of the initial Lorentz factor Γ_0 and the density ratio n_4/n_1 between the unshocked shell material and the ambient medium (Sari & Piran 1995). For a homogeneous shell with width Δ, the particle density is $n_4 \sim (E/m_p c^2 \Gamma_0)/(4\pi r_d^2 \Delta \Gamma_0)$. Since the shock jump conditions and equality of pressure along the contact discontinuity give a relation $n_4/n_1 \sim 4\Gamma_d^2/\left[(4\bar{\Gamma}_d + 3)(\bar{\Gamma}_d - 1)\right]$, we get an equation [4] for $x \equiv \Gamma_d/\Gamma_0$ as

$$\xi^2 \sim \frac{24 x^{8/3}}{2^{2/3}(1-x)^2(2+3x+2x^2)}, \tag{2.8}$$

where $\xi = (l/\Delta)^{1/2} \Gamma_0^{-4/3}$ and we have used $\bar{\Gamma}_d \sim (x + 1/x)/2$. The corresponding results are shown in Figure 2.2. For $\xi \ll 1$, we obtain $x \sim 0.47 \xi^{3/4}$, while for $\xi \gg 1$, we obtain $x \sim 1$. In the rest of the chapter, we call the estimates obtained in

[4] Assuming $r_d = l^{3/4} \Delta^{1/4}$, Nakar & Piran (2004) have obtained a similar equation.

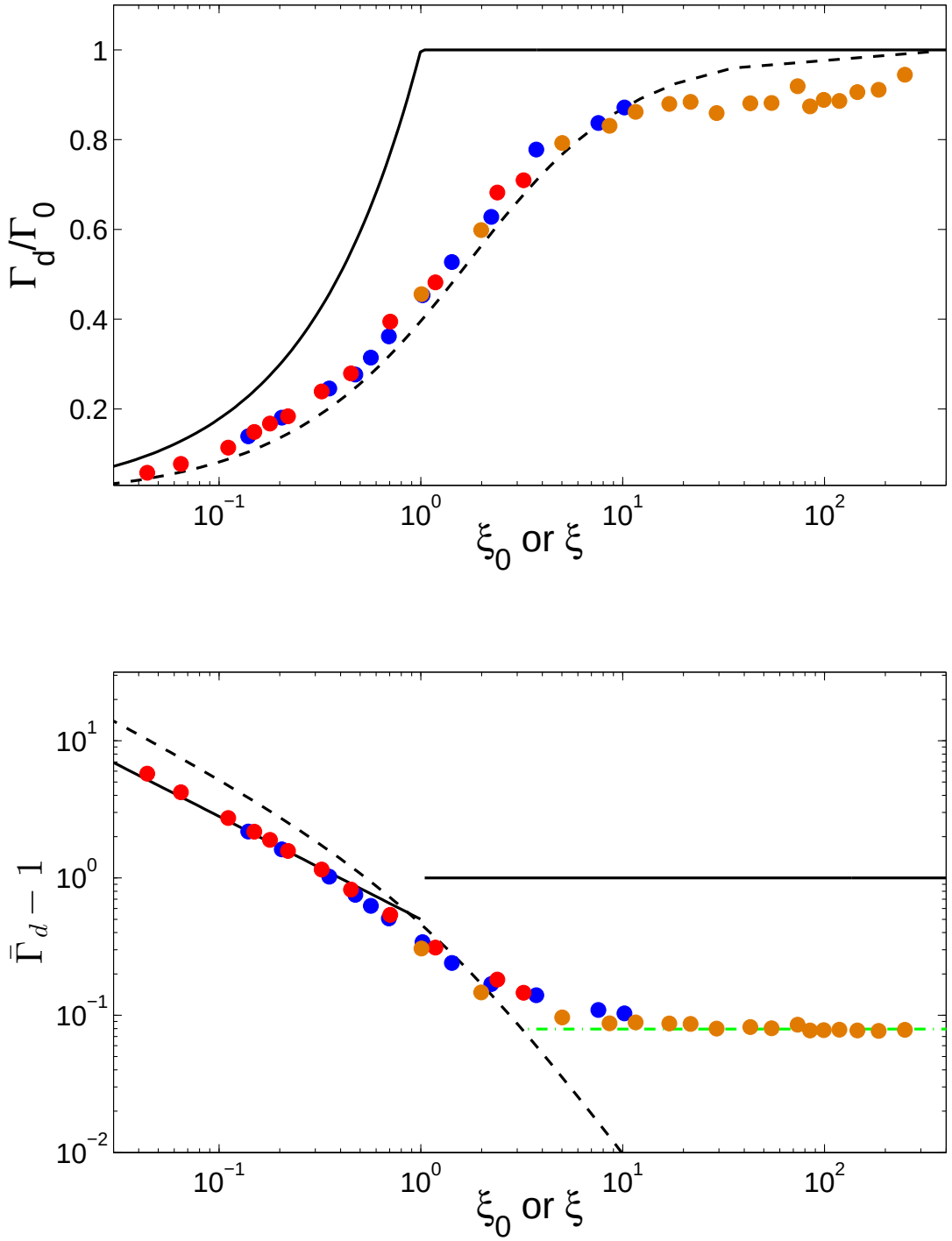

Figure 2.2: Γ_d/Γ_0 (top panel) and $(\bar{\Gamma}_d - 1)$ (bottom panel) as functions of ξ_0 or ξ, showing conventional estimates (black solid lines), the approximation 2.8 (black dashed lines), and the numerical results (orange dots: $r_0 = 10^9$cm, blue dots: 6×10^{11}cm, and red dots: 6×10^{12}cm). See the text concerning the choice of ξ_0 or ξ.

this section as the approximation 2.8 or the estimates based on Equation 2.8, while the estimates discussed in Section 2.2 are called the conventional estimates. Since Equation 2.8 gives x for a given ξ, to estimate x at the deceleration radius r_d, we need to use the value of ξ at r_d. In the thick shell regime $\xi_0 < 1$, ξ is a constant during the deceleration process and we can use the initial value ξ_0. However, in the thin shell regime $\xi_0 \gg 1$ and due to the shell's spreading $\Delta \sim \Delta_0 + r_d/\Gamma_0^2 \sim \Delta_0(1+\xi_0^2)$, the value $\xi \sim \xi_0(1+\xi_0^2)^{-1/2}$ is always about unity at r_d (Sari & Piran 1995). Then, if we plot x and the reverse shock temperature $(\bar{\Gamma}_d - 1)$ as functions of the initial value ξ_0, they are expected to flatten in the intermediate regime. Since $\xi \sim \xi_0$ in the thick shell and intermediate regime, we can directly compare the two approximations, and we find that the conventional approximation overestimates x and $(\bar{\Gamma}_d - 1)$ in the intermediate regime. The conventional estimates are $x = \xi_0^{3/4}$ and $(\bar{\Gamma}_d - 1) = \xi_0^{-3/4}/2$ for $\xi_0 < 1$ and $x \sim 1$ and $(\bar{\Gamma}_d - 1) \sim 1$ for $\xi_0 > 1$.

Using the deceleration radius r_d and the Lorentz factor Γ_d, the deceleration time is $t_d \sim r_d/(2c\Gamma_d^2) = l/(2^{4/3}c\Gamma_d^{8/3})$. For the solution of Equation 2.8, we have an estimate of the correction factor $C_t = 2^{-4/3}x^{-8/3}$. Assuming no gradients in the distribution functions of the pressure and velocity in the shock regions, we obtain $\nu_{m,r}/\nu_{m,f} \sim (\bar{\Gamma}_d - 1)^2/\Gamma_d^2$ and $F_{\nu,max,r}/F_{\nu,max,f} \sim \Gamma_d^2/\Gamma_0$ where we have assumed $R_B = \epsilon_{B,r}/\epsilon_{B,f} = 1$. Then, we get the correction factors $C_m \sim (1-x)^4/(4x^4)$ and $C_F \sim x^2$.

2.5 Numerical Simulation

The two analytic estimates which we have discussed include approximations (e.g. a simplified shock approximation and no gradients in the distribution functions of hydrodynamical quantities in the shock regions). Furthermore, the estimate 2.8 gives the Lorentz factor Γ_d for a given ξ at the deceleration radius r_d, instead of the initial value ξ_0. Since the typical frequency of the reverse shock emission is sensitive to the temperature $(\bar{\Gamma}_d - 1)$, it is important to investigate how ξ at r_d depends on ξ_0 (or where ξ becomes a constant) and what asymptotic value the reverse shock temperature takes in

the thin shell regime. To examine the accuracy of the approximations and evaluate the shock Lorentz factors and the corrections factors C_t, C_m and C_F, we employ a spherical Lagrangian code based on the Godunov method with an exact Riemann solver (Kobayashi et al. 1999; Kobayashi & Sari 2000; Kobayashi & Zhang 2007; see also appendix A). No MHD effects are included in our purely hydrodynamic calculations. However, if the magnetisation of a fireball is not too large (i.e. the ratio of magnetic to kinetic energy flux $\sigma \lesssim 0.1$; Giannios et al. 2008; Mimica et al. 2009), the dynamics of shocks is not affected by magnetic fields, and our numerical results can be used to model the synchrotron emission from forward and reverse shocks. We will evaluate the correction factors for $R_B = \epsilon_{B,r}/\epsilon_{B,f} = 1$.

The initial configuration for our simulations is a static uniform fireball surrounded by a uniform cold ISM. The hydrodynamic evolution is evaluated through the stages of initial acceleration, coasting, energy transfer to the ISM and deceleration. The evolution of a fireball is fully discussed in Kobayashi et al. (1999). We assume explosion energy $E_0 = 10^{52}$ ergs and ambient density $n_1 = 1$ proton cm^{-3} for all the simulations, while we vary the dimensionless entropy ($40 < \Gamma_0 < 10^3$) and the initial fireball size ($r_0 = 10^9$cm, 6×10^{11}cm, or 6×10^{12}cm) to cover a wide rage of ξ_0.

2.5.1 Spectra and Light Curves

We evaluate shock emission as a sum of photons from Lagrangian cells (fluid cells) in numerical calculations. First consider a single fluid cell with Lorentz factor Γ, internal energy density e, particle density n and mass m in a shocked region (forward or reverse shock). Electrons are assumed to be accelerated in the shock to a power-law distribution with index $\hat{p} = 2.5$ above a minimum Lorentz factor γ_m. We assume that constant fractions $\epsilon_e = 6 \times 10^{-2}$ and $\epsilon_B = 6 \times 10^{-3}$ of the shock energy are given to electrons and magnetic fields, respectively. Our results are insensitive to the exact values of the microphysical parameters as long as $R_B = 1$, but they are included here for completeness. The typical random Lorentz factor and the energy of magnetic fields evolve as $\gamma_m \propto e/n$ and $B^2 \propto e$. The typical synchrotron frequency in the observer

frame is $\nu_m \propto \Gamma\gamma_m^2 B$, and the peak spectral power is $F_{\nu,max} \propto N_e \Gamma B$ for a total number $N_e \sim m/m_p$ of electrons in the cell. As we use a Lagrangian code, N_e remains constant throughout the numerical evolution. The flux at a given frequency above ν_m is $F_\nu = F_{\nu,max}(\nu/\nu_m)^{-(\hat{p}-1)/2} \propto m\Gamma^{(\hat{p}+1)/2} e^{(5\hat{p}-3)/4} n^{1-\hat{p}}$, while below ν_m we have a synchrotron low-energy tail as $F_\nu = F_{\nu,max}(\nu/\nu_m)^{1/3} \propto m\Gamma^{2/3} e^{-1/3} n^{2/3}$. Then, the emission from a cell can be estimated by using hydrodynamic quantities. Here we give the description for slow cooling regime as this is typical for ISM external medium events, however we note that this choice is driven from the hydrodynamical properties and the code can handle fast cooling regime also.

We treat a fluid cell as a particle that continually emits photons. However, we only have the locations of the cell $\{r_j\}$ and flux estimates $\{F_{\nu,j}\}$ at discrete timesteps $\{t_{lab,j}\}$ where the subscript j indicates quantities at lab timestep j and r_j indicates the inner boundary of the cell. We assume all the photons are emitted from the inner boundary (i.e. we neglect the radial width of the cell). Prior to the light curve construction we generate a series of logarithmic bins with boundaries $\{t_k\}$ in the observer time domain, and we assume bin k is bounded by t_k and t_{k+1}. We now consider the emission from a single fluid cell between two consecutive lab timesteps: j and $j+1$. Since a photon emitted at timestep j arrives at the observer at $t_j \equiv t_{lab,j} - r_j/c$, photons spread over observer time bins between t_j and t_{j+1}. Note that the observational time t_j monotonically increases with j. Assuming that the observed flux F_ν evolves linearly between t_j and t_{j+1}, and that the observer detects photons between ν_R and $\nu_R + d\nu$, we can estimate the amount of energy deposited in each time bin.

By monitoring the entropy evolution of a fluid cell, we can determine when the cell is heated by a forward or reverse shock. Then, we take into account all the timesteps after the shock heating for the construction of the light curve of the single fluid cell. We can apply this technique to all the cells inside (or outside) the contact discontinuity, and the total energy from all the cells in each time bin is divided by the bin size to get the reverse (or forward) shock light curve. It is then the simple matter of finding the maximum flux to obtain the peak time t_p of the reverse shock emission.

To numerically define a property f of the fireball shell at the peak time, we consider

an average value

$$\langle f \rangle = \frac{\sum f_i \delta E_i}{\sum \delta E_i}. \tag{2.9}$$

where the summation is taken over all the fluid cells $\{i\}$ which are inside the contact discontinuity (i.e. in the reverse shock region) and which have contributed to the peak flux and δE_i is the contribution from fluid cell i to the peak time bin.

At the peak time, we construct the spectrum. For this purpose, we set up a series of bins $\{\nu_q\}$ in the frequency domain. For the peak time bin (i.e. the time bin which gives the peak flux), we know which fluid cells have contributed, and at which lab timestep it has happened. Let us assume that a fluid cell deposits energy between lab timestep j and $j+1$. Assuming a linear evolution of the luminosity $\int_{\nu_q}^{\nu_{q+1}} F_\nu d\nu$ between the timesteps, we can estimate how much energy is deposited in each frequency bin at the peak time (the peak time bin). After summing up all the energy deposited by the relevant fluid cells in each frequency bin, we divide the energy by the frequency bin size to get the spectrum at the peak time.

2.5.2 Comparison of the Estimates and the Correction Factors

Figure 2.2 shows the Lorentz factor Γ_d and the reverse shock temperature $(\bar{\Gamma}_d - 1)$ at the peak time t_p. For the numerical results (the dots), we have used Equation 2.9 with $(\bar{\Gamma}_d - 1) = e/nm_pc^2$ to obtain the average values, and we have assumed $\Delta_0 = r_0$ to estimate ξ_0. The numerical results and the conventional approximation are plotted against ξ_0, while the approximation 2.8 is plotted against ξ. As we have discussed in Section 2.4, when the initial value is high, $\xi_0 \gg 1$ and the ξ parameter is expected to decrease to order-of-unity during the evolution. One finds that such flattening in the numerical results occurs at a rather high value $\xi_0 \sim$ several. The approximation 2.8, especially for $(\bar{\Gamma}_d - 1)$ in the intermediate regime and for Γ_d over almost the whole range, is in better agreement with the numerical results, compared to the conventional estimates. The green dashed-dotted line in the bottom panel indicates the numerical asymptotic value: $\left\langle \bar{\Gamma}_d - 1 \right\rangle \sim 8 \times 10^{-2}$.

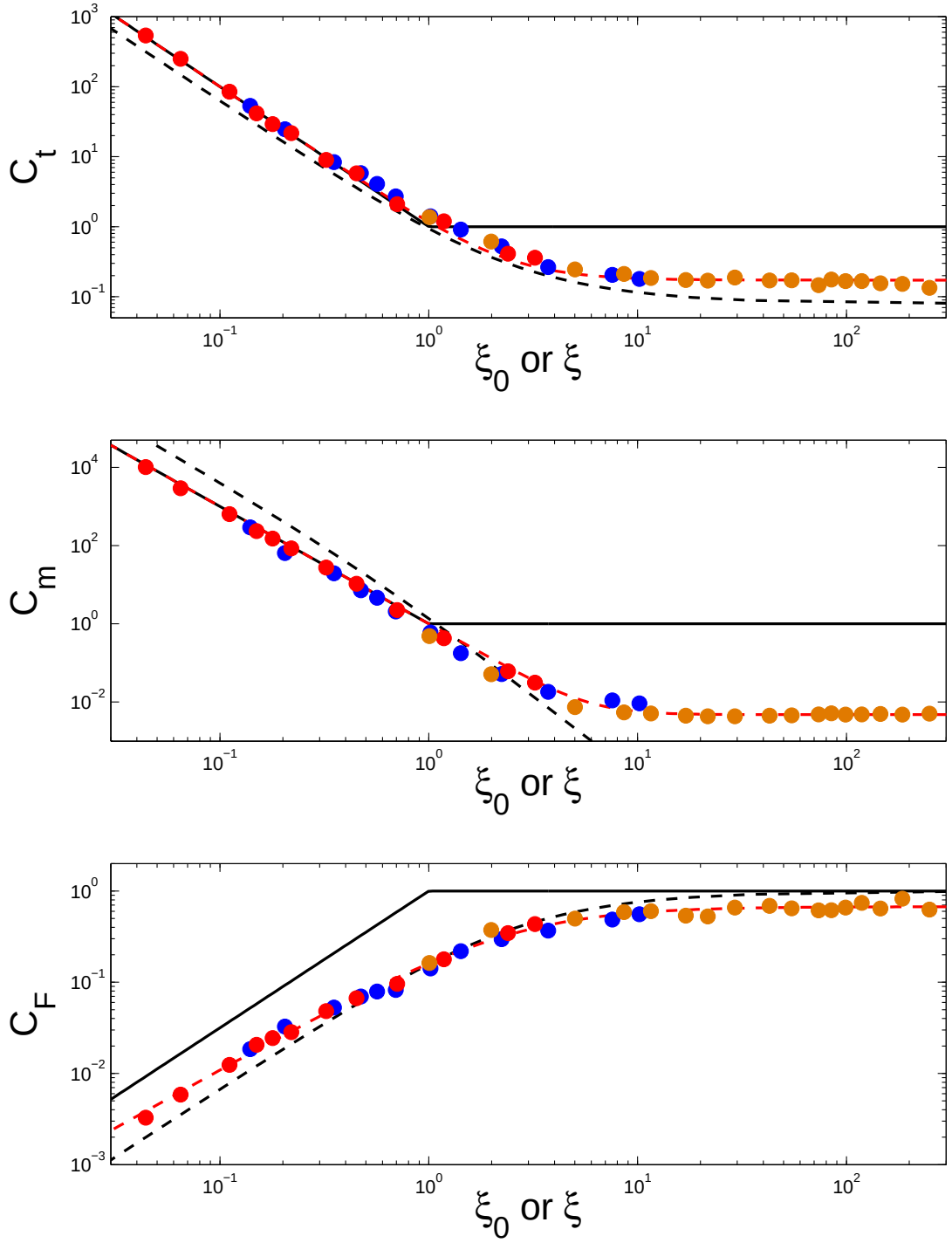

Figure 2.3: The correction factors as a function of ξ_0 or ξ. Top panel: The normalised peak time C_t, middle panel: The normalised typical frequency ratio C_m, and bottom panel: The normalised peak flux ratio C_F. The panels show the conventional estimates (black solid lines), the estimate based on the approximation 2.8 (black dashed lines), the numerical results (blue, red and orange dots are the same as in Figure 2.2), and numerical fitting formulae (red dashed lines).

Using a numerical peak time t_p, we estimate the correction factor $C_t = ct_p\Gamma_0^{8/3}/l$ as a function of ξ_0. The results are shown in the top panel of Figure 2.3. The conventional approximation well explains the numerical results in the thick shell regime $\xi_0 < 1$ but it breaks down in the thin shell regime $\xi_0 > 1$. In the thin shell regime, the numerical C_t is lower by a factor of ~ 5 than the conventional estimate which is equivalent to the numerical peak time being earlier than expected. Since for simplicity we have neglected a factor of 2 in the conventional estimate as $t_d = l/c\Gamma_0^{8/3}$ instead of $l/2c\Gamma_0^{8/3}$, $C_t = 0.5$ would be more appropriate for the conventional estimate in the thin shell regime. However, the numerical results are still smaller. This is in part due to the gradients in the distribution functions of hydrodynamical quantities in the reverse shock region. The numerical distributions have a higher value at the contact discontinuity, and they decrease toward the tail (see Figure 3 in Kobayashi & Zhang 2007). It makes the contribution of photons from the inner parts of the fireball shell less significant, reducing the effective width of the emission region in the shell, and the shock emission peaks earlier than in the homogeneous shell case. Since as we will see later, the magnetisation estimate is rather insensitive to C_t (and the peak time), we discuss only the line-of-sight emission in this chapter. However, it is possible to include the high latitude emission at expense of computational time, and we have obtained very similar results for several selected cases. With the addition of the high latitude emission the overall light curve appears smoother with slightly shallower decay features. The position of the peak time increases by $\sim 50\%$.

Using the numerical values of the typical frequency ratio at the peak time, we estimate the correction factor $C_m = \Gamma_0^2\,[\nu_{m,r}(t_p)/\nu_{m,f}(t_p)]$ as a function of ξ_0. The results are shown in the middle panel of Figure 2.3. The conventional estimate is in good agreement with the numerical results in the thick shell regime, but as we expect from $C_m \propto (\bar{\Gamma}_d - 1)^2$, it overestimates C_m by a factor of $\sim 10^2$ in the thin shell regime. Finally the bottom panel of Figure 2.3 shows the results for $C_F = \Gamma_0^{-1}\,[F_{\nu,max,r}(t_p)/F_{\nu,max,f}(t_p)]$. The conventional approximation overestimates the amount of flux emitted by the reverse shock especially in the intermediate regime as Nakar & Piran (2004) have pointed out. The estimates based on Equation 2.8 provide a better approximation for all three

correction factors in the intermediate regime. The red dashed lines in the three panels indicate the numerical fitting formulae $C_t = N_t + \xi_0^{-2}$ with $N_t \sim 0.2$, $C_m = N_m + \xi_0^{-3}$ with $N_m \sim 5 \times 10^{-3}$ and $C_F^{-1} = N_F + M_F \xi_0^{-P_F}$ with $N_F \sim 1.5$, $M_F \sim 5$ and $P_F \sim 1.3$.

Figure 2.4 illustrates wide band spectra at the peak time. We here consider three numerical cases with $\xi_0 = 0.1, 1$ or 10. The black line indicates the conventional estimate in which the typical frequency $\nu_{m,r}$ of the reverse shock emission is lower by a factor of Γ_0^2 than that of the forward shock emission, and the peak flux $F_{\nu,max,r}$ of the reverse shock emission is higher by a factor of Γ_0. However, our numerical results show that in the thin shell regime $\nu_{m,r}$ is lower by a further factor of $\sim 10^2$ than the conventional estimate (the red line) [5], and that in the intermediate regime the peak flux $F_{\nu,max,r}$ would be lower by a factor of several (the green line). These indicate that the reverse shock emission would be elusive if the typical frequency of the forward shock is around the optical band and if the forward and reverse shock have the same microscopic parameters (Nakar & Piran 2004; Mimica et al. 2010; Melandri et al. 2010). In the thick shell regime, the peak frequency of the reverse shock emission is closer to that of the forward shock emission $\nu_{m,r}/\nu_{m,f} \sim \xi_0^{-3}\Gamma_0^{-2}$ (the blue line). We might have a better chance to detect the reverse shock component in early afterglow, although the light curve peaks earlier than in the thin shell regime.

2.5.3 Initial Lorentz Factor and Magnetisation Parameter

The initial Lorentz factor can be evaluated by using the peak time $t_p \sim t_d$,

$$\Gamma_0 = \left(\frac{C_t l}{c t_p}\right)^{3/8} \tag{2.10}$$

where l is a known quantity from the prompt gamma-ray and late-time afterglow observations, and the estimate depends very weakly on more fundamental parameters $\Gamma_0 \propto l^{3/8} \propto (E/n_1)^{1/8}$, and we had obtained numerical result $C_t \sim 0.2 + \xi_0^{-2}$. In

[5] If the typical frequency $\nu_{m,r}$ is as low as $\sim 10^{12}$Hz, the spectrum of the reverse shock emission would peak at the synchrotron self-absorption frequency (Nakar & Piran 2004).

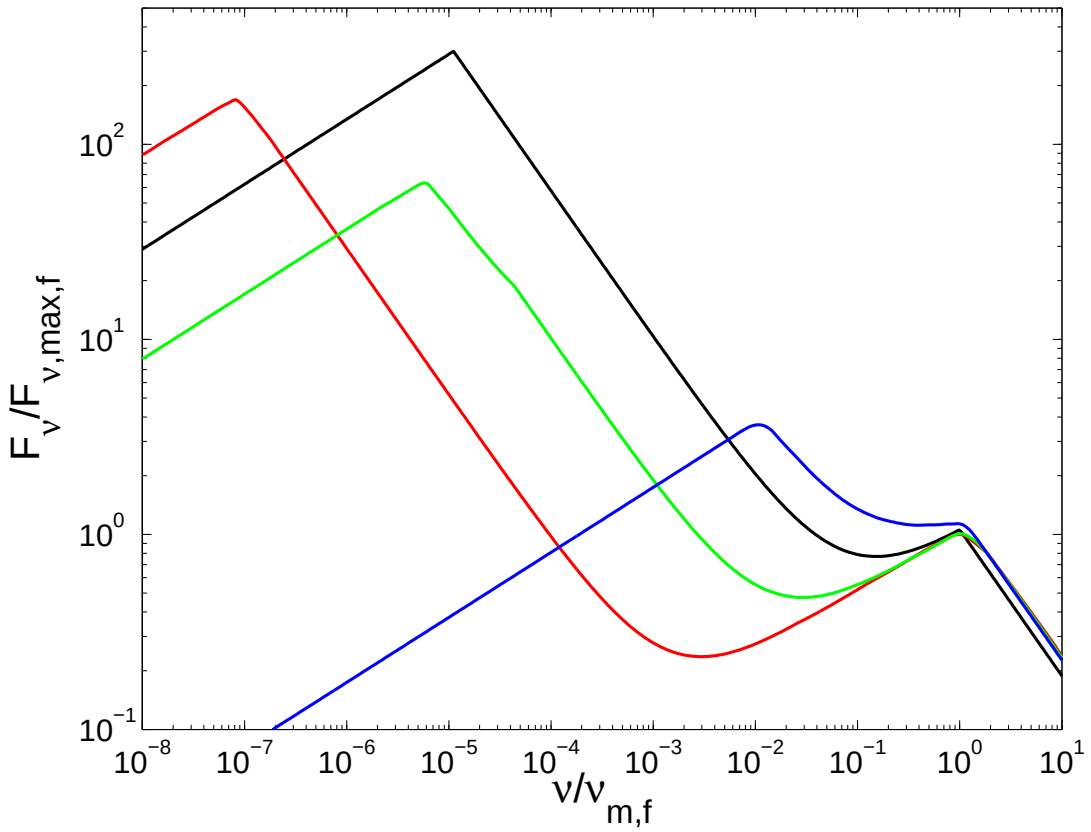

Figure 2.4: Numerical wide band spectra at the peak time: $\xi_0 = 0.1$ (blue line), 1 (green line) and 10 (red line). The black line shows the conventional estimate (thin shell case). The frequency and flux are normalised by the typical frequency and peak flux of the forward shock emission, respectively. $\Gamma_0 = 300$ and $\Delta_0 \sim 3 \times 10^9$cm (red line), $\sim 3 \times 10^{11}$cm (green line), or $\sim 3 \times 10^{13}$cm (blue line) are assumed.

principle, we can estimate ξ_0 from observable quantities. Since the duration T of the prompt gamma-rays gives a rough estimate of the width $\Delta_0 \sim cT$ (Kobayashi et al. 1997), using Equation 2.10 and the numerical $C_t(\xi_0)$, we obtain $\xi_0 \sim 5^{1/2}\sqrt{(t_p/T)-1}$ and $C_t \sim 0.2(1-T/t_p)^{-1}$. In the thin shell regime, an early afterglow peaks well after the prompt gamma-ray emission (Sari 1997), and we have $C_t \sim 0.2$. However, in the thick shell regime, the peak time is almost equal to the width Δ_0/c. The approximation $\Delta_0 = cT$ might not be accurate enough to discuss the exact value of ξ_0. Since the flux before the optical peak t_p is sensitive to the initial profile of the shell and in particular to ξ_0, the rising index of the light curve might be used to break the degeneracy of the ξ_0 estimate in the thick shell regime. Nakar & Piran (2004) have numerically estimated the rising index for a homogeneous shell in a range of $0.05 < \xi_0 < 5$ as $\alpha_{rise} \sim 0.6\,[1+\hat{p}(\xi_0 - 0.07\xi_0^2)]$. A slow (rapid) rise is a signature of the thick (thin) shell regime (Kobayashi 2000).

The magnetisation parameter R_B can be estimated by using Γ_0 R_t, and R_F. For the typical decay index of the reverse shock emission $\alpha = 2$, the conventional estimate is $R_{B,con} = (R_F^3\Gamma_0/R_t^3)^{2/5}$ in the thin shell regime where $\Gamma_0 = (l/ct_p)^{3/8}$. Then, we obtain a correction factor for the magnetisation parameter as

$$\frac{R_B}{R_{B,con}} = \frac{C_t^{3/20}}{C_F^{6/5}C_m^{4/5}}. \tag{2.11}$$

This shows that the estimate is rather insensitive to C_t. In Figure 2.5, the numerical results are plotted with the approximations. For a typical GRB ($\xi_0 \sim 1$), the conventional approximation (black solid line) underestimates the magnetisation parameter by a factor of ~ 10. A more extreme discrepancy occurs in the thin shell regime, and the magnetisation parameter is underestimated by a factor of $\sim 10^2$. The estimate based on Equation 2.8 (black dashed line) describes the numerical results reasonably well in the intermediate and thick shell regimes.

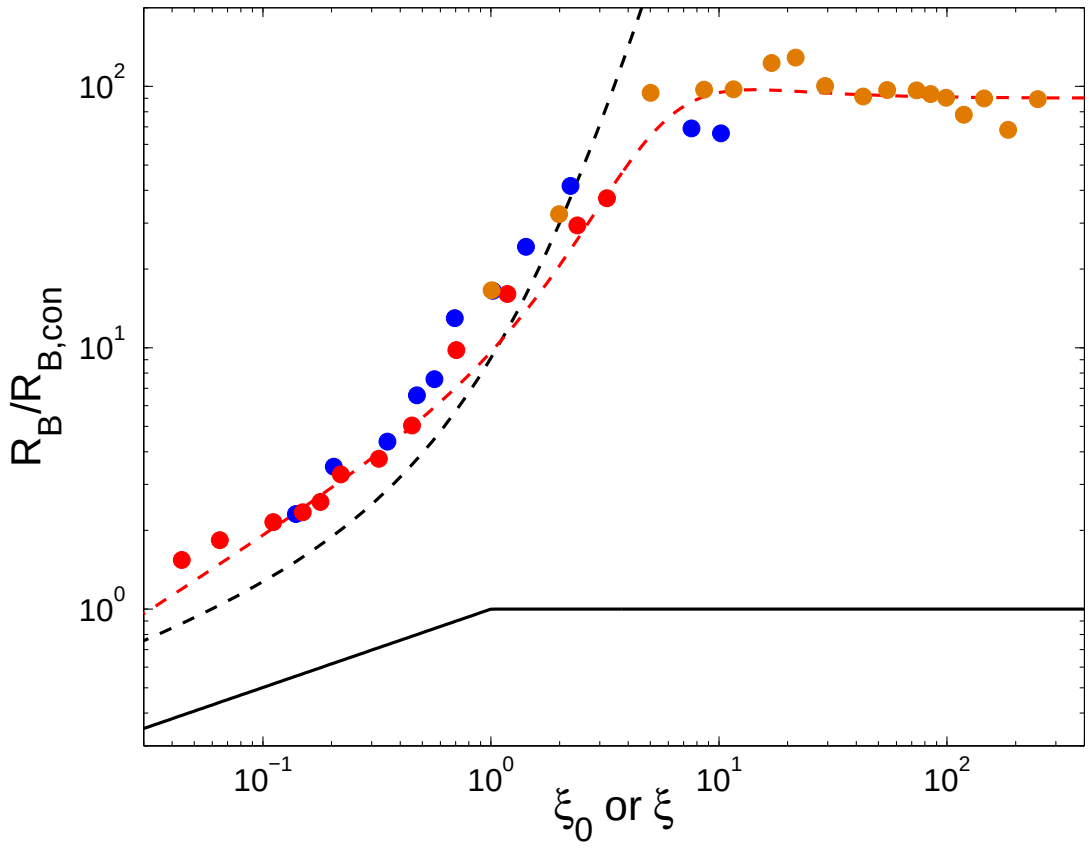

Figure 2.5: The correction factor for the magnetisation parameter $R_B/R_{B,con}$ as a function of ξ_0 or ξ. The legend is the same as Figure 2.3 with the best fit equation (red dashed line) obtained by the combination of the best fits to C_t, C_m and C_F. $\alpha = 2$ is assumed.

2.6 Case Studies

Swift revealed that the behaviour of early afterglows is more complicated than expected and there are indications of long-lasting central engine activity (e.g. flares and late-time energy injection; Zhang et al. 2006; Nousek et al. 2006; O'Brien et al. 2006). Although the nature of the central engine activity and additional components in early afterglows are interesting research subjects, in order to demonstrate our scheme which is based on an impulsive explosion model, we discuss early optical afterglows associated with GRB 990123 and GRB 090102. These light curves are described by a broken power-law with no flares (see Figure 2.6)

GRB 990123: This burst is one of the brightest GRBs observed so far. The basic parameters include $z = 1.6$, $E \sim 1.4 \times 10^{54}$ergs, and $T \sim 60$s (e.g. Kobayashi & Sari 2000 and references therein). The gamma-ray profile is dominated by two pulses, each lasting ~ 8s, separated by 12s. A bright optical flash was detected during the prompt emission (Akerlof et al. 1999), the optical emission peaked at $t_p \sim 50$s at 9 mag, and initially rapidly decayed and it became shallower at a late time $t_{p,f} < 0.1$ days. Using the bootstrap method for the light curve fitting, we find that $\alpha = 2.31 \pm 0.38$ and $\alpha_f = 1.09 \pm 0.07$ where the errors quoted are values to within 3 σ of the best fits. We have only one optical data point before the peak, and it provides a lower limit of both the rising index $\alpha_{rise} > 2$ and the peak flux. We conservatively assume that the peak flux is 9 mag. Since the optical peak is comparable to the GRB duration (especially to the duration of the main two pulses) and the rising is rapid, this is an intermediate case $\xi_0 \sim 1$, with the correction factors $C_t \sim 1.2$, $C_m \sim 1$ and $C_F \sim 0.16$. Using Equation 2.10 with a time-dilation correction, we obtain an initial Lorentz factor of about $\Gamma_0 \sim 460 n_1^{-1/8}$. Assuming $t_{p,f} = 0.1$days, one has $R_t \sim 170$ and $R_F \sim 5000$, Equation 2.5 gives the magnetisation parameter $R_B \sim 6300^{6600}_{6000}$ where the subscript and superscript indicate the range of the value when the error in α is taken into account. Since the forward shock peak is masked by the reverse shock emission, the peak time $t_{p,f}$ is rather uncertain. As we have discussed in Section 2.3, the magnetisation estimate depends on $t_{p,f}$ as $R_B \propto t_{p,f}^{6(1+\alpha_f-\alpha)/(1+2\alpha)} \sim t_{p,f}^{-0.23}$. If the forward shock emission also

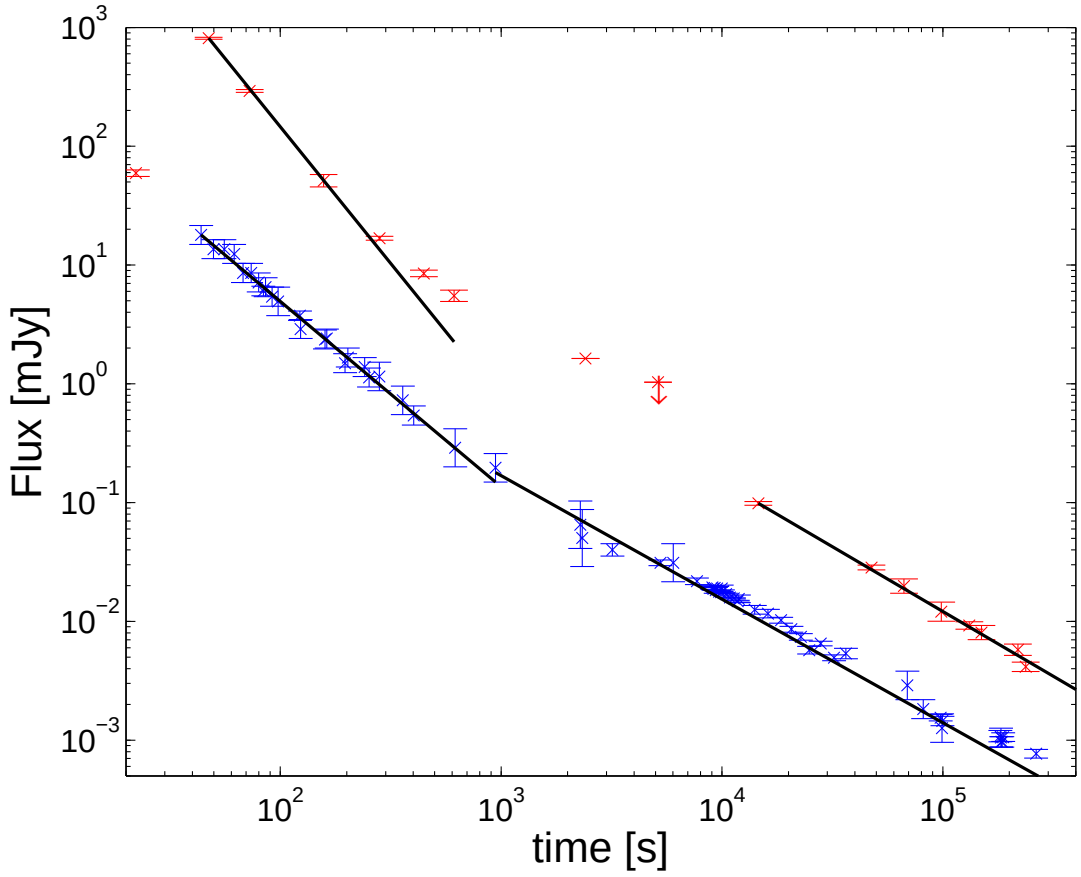

Figure 2.6: Light curves of early optical afterglows: GRB 990123 (red points) and GRB 090102 (blue points). The solid lines depict power-law fitting to the forward shock and reverse shock emission components. Data are from Kulkarni et al. (1999); Kobayashi & Sari (2000); Gendre et al. (2010) and references therein.

peaks at $t_{p,f} \sim 50$s, the magnetisation parameter R_B is larger by a factor of ~ 3. Since Zhang et al. (2003) found a magnetisation parameter of $R_B \sim 15^2 = 225$ based on the conventional approximation with $\xi_0 \sim 1$, our magnetisation estimate is larger by more than an order of magnitude.

GRB 090102: This burst shows a significant polarisation at the 10% level in the early optical afterglow and it suggests a magnetised fireball (Steele et al. 2009). The basic parameters include $z = 1.5$, and $E \sim 5.8 \times 10^{53}$ergs (e.g. Gendre et al. 2010 and references therein). The prompt gamma-ray emission lasts for 27s and comprises four overlapping peaks starting 14s before the GRB trigger. The optical light curve, beginning at 13 mag, 40s after the GRB trigger, can be fitted by a broken power-law whose flux decays as a function of time ($F \propto t^{-\alpha}$) with a gradient $\alpha = 1.56 \pm 0.06$ that then flattens to $\alpha_f = 1.04 \pm 0.09$ (shown as solid lines in Figure 2.6; a break time is assumed to be 10^3s). If we assume that the optical emission peaks at the first data point (the mid-time, of which is is $t_p \sim 60$s after the beginning of the GRB) and $t_{p,f} = 10^3$s, we obtain $\xi_0 \sim 2.4$ and the correction factors: $C_t \sim 0.3, C_m \sim 8 \times 10^{-2}$, and $C_F \sim 0.3$. Using $R_t \sim 17, R_F \sim 91$ and $\Gamma_0 \sim 230 n_1^{-1/8}$, we obtain $R_B \sim 220^{310}_{150}$. Since the optical emission is already declining at the beginning of the observations, the actual peak time t_p might be earlier. If we assume that it peaks at the end of the prompt gamma-ray emission $t_p \sim 30$s, it would be in the intermediate regime $\xi_0 \sim 1$ and $\Gamma_0 \sim 290 n_1^{-1/8}$. Assuming $t_{p,f} = 10^3$s, we obtain $R_B \sim 140^{180}_{110}$. The magnetisation estimates depend on $t_{p,f}$ as $R_B \propto t_{p,f}^{0.7}$. If $t_{p,f} = 10^2$s, R_B is smaller by a factor of ~ 5.

The σ parameter: The broadband afterglow emission of GRB 990123 is modelled to find $\epsilon_{B,f} \sim 10^{-6}$ (Panaitescu & Kumar 2004). Although there are no estimates available for GRB 090102, the broadband modelling generally shows that it is in a range of $\epsilon_{B,f} = 10^{-5} - 10^{-1}$ (Panaitescu & Kumar 2002). Using the estimated value of the magnetisation parameter R_B, the ratio of magnetic to kinetic energy flux is $\sigma \sim 10^{-3}(g/0.25)(R_B/6300)(\epsilon_{B,f}/10^{-6})$ for GRB 990123 where $g \equiv (\bar{\Gamma}_d - 1)/\bar{\Gamma}_d \sim 0.25$ for $\xi_0 \sim 1$. For GRB 090102, assuming $g \sim 0.15$ ($\xi_0 \sim 2.4$) and $R_B \sim 220$, it is in a range of $\sigma \sim 3 \times 10^{-4} - 3$. Although magnetic pressure would suppress the formation of a reverse shock if $\sigma \gtrsim 0.1$ (Giannios et al. 2008; Mimica et al. 2009), the low

values are consistent (or the result is consistent with these parameter estimates) with the basic assumption in our analysis (i.e. magnetic fields do not affect the reverse shock dynamics). If a future event indicates a high value $\sigma \gtrsim 0.1$, an interesting possibility to reconcile the problem is that the prompt optical emission (and prompt gamma-rays) would be produced through dissipative MHD processes rather than shocks (Giannios & Spruit 2006; Lyutikov 2006; Giannios 2008; Zhang & Yan 2011).

Our magnetisation estimates are slightly lowered if the blast wave radiates away a significant fraction of the energy in the early afterglow, and hence $E \propto t^{-17\epsilon_e/16}$ (Sari 1997). For $\epsilon_e = 0.1$, the blast wave energy becomes smaller by a factor of 1.7 between $t = 50$s and 0.1 days, by a factor of 1.3 between $t = 60$s and 10^3s, then the estimates of R_B and σ are reduced by a factor of $1.5 - 2$.

2.7 Conclusions

We have discussed a revised method to estimate the magnetisation degree of a GRB fireball. We use the ratios of observed properties of early afterglows so the poorly known parameters for the shock microphysics (e.g. ϵ_e and $\hat{p}$) would cancel out. Since the estimate depends only weakly on the explosion energy and the fireball deceleration time, the estimate does not require the exact distance (redshift) to the source as an input parameter. Since most observed events fall in the intermediate regime between the thin and thick shell extremes, we have provided a new approximation for the spectral properties of the forward shock and reverse shock emission, which well describes the numerical results in the intermediate regime. The previous standard approach underestimates the degree of fireball magnetisation R_B by a factor of $10 \sim 100$. We have estimated $\sigma \sim 10^{-3}$ for GRB 990123. For GRB 090102, it is not well constrained due to the uncertainty in $\epsilon_{B,f}$, and it is in a range of $\sigma \sim 3 \times 10^{-4} - 3$.

In the GRB phenomena, extreme relativistic motion with $\Gamma_0 > 100$ is necessary to avoid the attenuation of hard gamma-rays. The acceleration process is likely to induce a small velocity dispersion inside the outflow $\Delta\Gamma \sim \Gamma$ (e.g. thermal acceleration).

If internal shocks are responsible for the production of the prompt gamma-rays, the dispersion should be even larger (Beloborodov 2000; Kobayashi & Sari 2001). The velocity dispersion leads to the spreading of the shell structure in the coasting phase and the ξ parameter decreases as $\xi \propto \Delta^{-1/2}$. As an order-of-magnitude estimate, when the initial value $\xi_0 > 1$, the reverse shock always becomes mildly relativistic $(\xi \sim 1)$ at the deceleration radius and the reverse shock temperature $(\bar{\Gamma}_d - 1)$ is expected to be insensitive to the initial value ξ_0. However, it is difficult to analytically quantify the asymptotic reverse shock temperature. We have numerically shown that the spreading effect becomes significant at rather high values $\xi_0 \gtrsim$ several, and that the asymptotic value is $(\bar{\Gamma}_d - 1) \sim 8 \times 10^{-2}$.

We have confirmed that, especially in the intermediate regime $\xi_0 \sim 1$, the reverse shock emission is much weaker than the standard estimates as Nakar & Piran (2004) pointed out, and that in the thin shell regime the typical frequency of the reverse shock emission is much lower than the standard estimates. If the fireball is not magnetised $R_B = \epsilon_{B,r}/\epsilon_{B,f} = 1$, the reverse shock emission more easily falls below the forward shock emission. The lack of optical flashes from most GRBs might be partially explained in a revised non-magnetised model. If the fireball shell does not spread even in the thin shell regime (i.e. the velocity distribution is completely uniform), only a small fraction of the kinetic energy of the shell is converted to thermal energy in the reverse shock, and the reverse shock emission is practically suppressed in the thin shell regime $\xi_0 \gg 1$.

Chapter 3

Wind and ISM Medium Magnetisation Estimate of an Optical Flash Selected GRB Sample

3.1 Introduction

GRB afterglows are generated by a relativistic blast wave propagating through an external medium (Blandford & McKee 1976). The simplest functional form of the external density profile is $n_1 \propto R^{-k}$ (Granot 2012; Yi et al. 2013) with two specific cases being associated with GRBs: (1) $k = 0$ for the homogeneous interstellar medium (ISM) case (Sari et al. 1998) (2) $k = 2$ for a stellar wind environment (Dai & Lu 1998; Mészáros et al. 1998; Chevalier & Li 2000; Panaitescu & Kumar 2000). The later model is motivated by the idea that the progenitor of a GRB is a massive star (Woosley 1993).

The composition of the relativistic jet is still highly contested with competition between a baryonic jet (Mészáros 2002; Piran 2004) or highly magnetised outflow (e.g. Drenkhahn & Spruit 2002). Measurements of polarisation in the optical (Steele et al. 2009; Uehara et al. 2012) and prompt emission (Kalemci et al. 2007; McGlynn et al. 2007; Götz et al. 2009; Yonetoku et al. 2011) indicate that the outflow contains

ordered magnetic fields, while is still unknown whether they are sufficiently strong to affect the dynamics. Understanding the magnetic energy content gives the ability to distinguish between the two models, providing insight into the acceleration process of the outflow. Efforts have been made in this direction (Fan et al 2002; Zhang et al. 2003; Kobayashi & Zhang 2003; Gomboc et al. 2008; Granot 2012; Harrison & Kobayashi 2013) prompting this study into the magnetisation degree of several events which exhibit the early steep decay phase associated with reverse shock emission (Akerlof et al. 1999; Sari & Piran 1999; Mészáros & Rees 1999; Soderberg & Ramirez-Ruiz 2002; Li et al. 2003; Fox et al. 2003; Nakar & Piran 2005).

Standard estimates of magnetisation degree are based on relative strength of forward and reverse shock emission (Zhang et al. 2003). However as shown by Nakar & Piran (2004) and more recently Harrison & Kobayashi (2013), simplified shock dynamics are insufficient to be applied to most GRBs, which are found in the intermediate regime (between thick and thin shell limits). This regime requires an improved analytical and numerical estimate to accurately calculate the relative emission strengths. Here we investigate the influence on the standard magnetisation estimate (Zhang et al. 2003; Kobayahsi & Zhang 2003; Harrison & Kobayashi 2013) when considering an external wind type environment, in Section 3.2. In Section 3.4 we set out a framework for generic calculation of magnetisation, and apply this formula to a sample of GRBs in Section 3.5. Finally we discuss these results in Section 3.6.

3.2 Magnetisation Degree In Wind Medium

We re-derive the magnetisation estimate accounting for the outflow expanding into a wind type environment ($n_1 = AR^{-2}$) following the same procedure set out in Chapter 2 (Harrison & Kobayashi 2013). Let us consider a coasting fireball shell of energy E, initial width Δ_0 and Lorentz factor Γ_0. The deceleration is described by two shocks, a forward shock propagating into the wind medium and a reverse shock propagating through the shell. The reverse shock evolution is determined by the dimensionless parameter $\xi_0 = (l/\Delta_0)^{1/2}\Gamma_0^{-2}$, with $l = E/4\pi m_p c^2 A$ being the Sedov length (Sari &

Piran 1995; Kobayashi & Zhang 2003; Granot, J. 2012; Yi et al. 2013). By equating the energy in the shocked ambient medium with E we get the deceleration radius $r_d \simeq l/\Gamma_0^2$. The observer sees the shell decelerate at time,

$$t_d = C_t \frac{l}{c\Gamma_0^4}, \tag{3.1}$$

with $C_t \sim (\Gamma_d/\Gamma_0)^{-4} \sim \max(1, \xi_0^{-2})$ being the corrective factor relative to the conventional thin shell estimate and Γ_d being the Lorentz factor of the shocked region at deceleration. Taking the magnetisation parameter as $R_B \equiv \epsilon_{B,r}/\epsilon_{B,f}$ it has been shown that the typical frequencies and maximal fluxes from the two shock regions are related as

$$\frac{\nu_{m,r}(t_d)}{\nu_{m,f}(t_d)} = C_m \Gamma_0^{-2} R_B^{1/2}, \quad \frac{F_{\nu,max,r}(t_d)}{F_{\nu,max,f}(t_d)} = C_F \Gamma_0 R_B^{1/2}, \tag{3.2}$$

at the deceleration time (Kobayashi & Zhang 2003; Zhang et al. 2003). Although these approximations are originally obtained for ISM external medium, they hold for wind medium also. This is because they are obtained by using shock jump conditions and energy conservation. Here the corrective factors are given by $C_m \sim (\Gamma_d/\Gamma_0)^{-4} \sim \max(1, \xi_0^{-2})$ and $C_F \sim (\Gamma_d/\Gamma_0)^2 \sim \min(1, \xi_0)$ in the conventional estimates. We have assumed that the electron equipartition parameter ϵ_e and electron power-law index $\hat{p}$ remain constant between the two shocked regions.

3.2.1 Relativistic/Newtonian Reverse Shock

Heaton & Kobayashi (in prep) have investigated how the reverse shock ejecta evolves in the wind medium after the shock crossing using hydrodynamical simulations (see Kobayashi & Sari 2000 for the deceleration in an ISM medium). By assuming that the Lorentz factor of the shocked region evolves as a power-law $R \propto \gamma^{-g}$, fitting to the simulations they found for a wind-type medium over a large range of ξ_0, g varies as $0.5 < g < 1$. With adiabatic expansion, we have pressure as $p \propto R^{-4(3+g)/3}$ and density as $\rho \propto R^{-(3+g)}$ with the assumption that the temperature of the shocked ejecta is relativistic (sound velocity $\sim c$). Then a typical $\hat{p} = 2.3$ indicates that the reverse

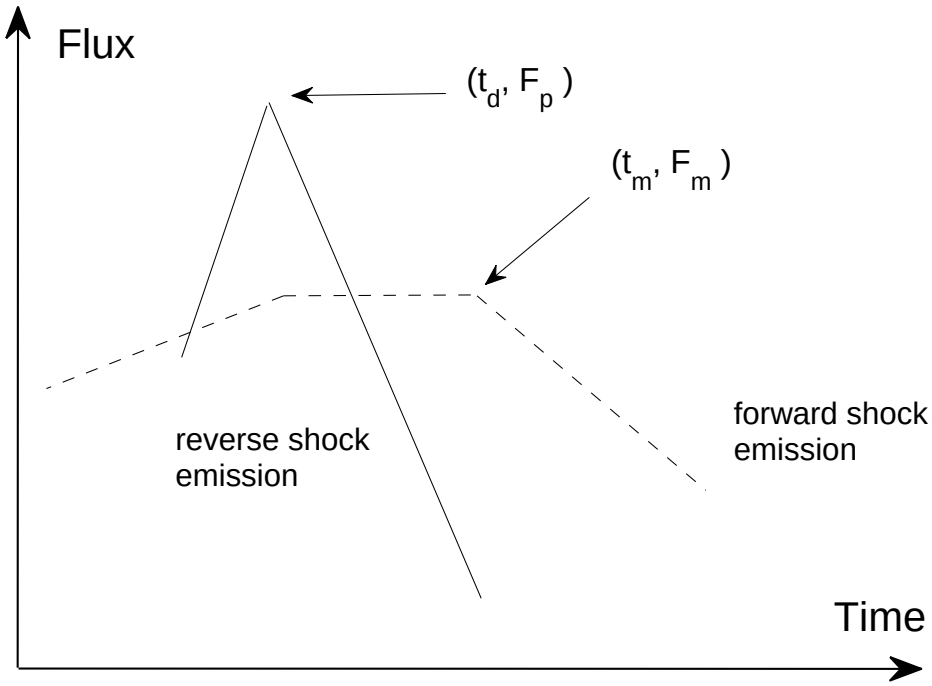

Figure 3.1: Optical afterglow composed of reverse (solid) and forward (dashed) shock emission for a wind medium in slow cooling regime. The light curve has one peak and a plateau phase associated with the passage of the forward shock typical frequency across observational band. If t_p occurs at earlier times the afterglow is seen as a flattening described by a two part broken power law.

shock decays as $\alpha \sim 2.6 - 3.1$ for $g = 0.5 - 1$ ($10^{-3} < \xi_0 < 10^2$), although this could be over a narrower range (e.g. $\alpha \sim 2.7 - 2.8$) if we consider that the GRB is described by the intermediate case $\xi_0 \sim 1$. Next, consider the case where the reverse shock is Newtonian and the temperature is now sub-relativistic, the sound speed is given by $(p/\rho)^{1/2}$ (Kobayashi & Sari 2000). Still assuming an adiabatic expansion, the pressure and density are now given by $p \propto R^{-8(3+g)/7}$ and $\rho \propto R^{-6(3+g)/7}$ respectively. Considering the same narrow range in g ($0.5 - 1$) gives $\alpha \sim 2.6 - 3.1$, comparable to the relativistic case. In the following framework we will use the decay index of the reverse shock emission as $\alpha \sim 5\hat{p}/4$ for the relativistic slow cooling case, as the Newtonian case is almost identical. This relation is a simplified approximation to the estimate presented by Heaton & Kobayashi (in prep).

3.2.2 Magnetisation Estimate

In the ISM regime it is possible to get two separated peaks for forward and reverse shock contribution (e.g. Figure 1 in Harrison & Kobayashi 2013). For the wind case observing separated forward and reverse shock components appears as in Figure 3.1, with the reverse shock peak is attributed to the deceleration of the fireball (t_d) and the forward shock peak is due to passage of the typical frequency across the observational band (t_m), except the forward shock emission is flat prior to t_m, for slow cooling regime (Chevalier & Li 2000). It is possible for the forward shock emission to decay as $t^{1/4}$ when considering the fast cooling regime, which we will discuss later, although observationally it may be not possible to distinguish between these cases. The flux and temporal ratios of the forward and reverse shock components (in the slow cooling regime) at the locations in Figure 3.1 are given by,

$$R_t \equiv t_m/t_d = \left[\frac{\nu_{m,f}(t_d)}{\nu_{opt}}\right]^{2/3}, \tag{3.3}$$

$$R_F \equiv F_p/F_m = \left[\frac{F_{\nu,max,r}(t_d)}{F_{\nu,max,f}(t_d)}\right] R_t^{1/2} \left[\frac{\nu_{opt}}{\nu_{m,r}(t_d)}\right]^{-(\hat{p}-1)/2} \tag{3.4}$$

using $\nu_{m,f} \propto t^{-3/2}$ and F_p is the peak flux of the reverse shock emission (steep component) and F_m is the flux of the forward shock emission at the temporal location when the typical frequency crosses the optical band, with t_d and t_m being the temporal locations of these fluxes respectively.

Combining Equations 3.2, 3.3 and 3.4 we find the magnetisation,

$$R_B = \left(\frac{R_F^{10} \Gamma_0^{8\alpha-20}}{C_F^{10} C_m^{4\alpha-5} R_t^{3(2\alpha-1)}} \right)^{2/(4\alpha+5)} \tag{3.5}$$

Here we estimate Γ_0 using the deceleration time (Equation 3.1). We note her that differences between the wind and the ISM estimate come from Equation 3.4 having an extra $R_t^{1/2}$ arising from the fact the forward shock maximal flux decaying as $F_{\nu,max,f} \propto t^{-1/2}$, and the reverse shock emission has $\alpha = 5\hat{p}/4$ instead of $\alpha_{ISM} \sim (3\hat{p}+1)/4$. We can also consider a case where the forward shock peaks at the deceleration time (i.e. $R_t = 1$). After the reverse shock decays sufficiently the forward shock emission will begin to dominate the light curve causing a flattening in the afterglow (R_t will now be determined relative to the location of flattening). In such a case we can only provide an approximate magnetisation degree as $t_m \leq t_{flat}$. At this location the reverse and forward shock emission should be comparable and we obtain that $R_F \sim R_t^{\alpha}$, such that

$$R_B = \left(\frac{R_t^{4\alpha+5/2} \Gamma_0^{8\alpha-20}}{C_F^{10} C_m^{4\alpha-5}} \right)^{2/(4\alpha+5)}, \tag{3.6}$$

with $R_t = t_{flat}/t_d$. By referring to the scalings $R_f \propto t_m^{\alpha_f}$ and $R_t \propto t_m$ we find the magnetisation (Equation 3.5) is independent on forward shock peak location $R_B \propto t_m^{(5+20\alpha_f-12\alpha)/(4\alpha+5)} \propto t_m^0$ for $\alpha_f = (3\hat{p}-1)/4$ (Gomboc et al. 2008; Harrison & Kobayashi 2013).

3.2.3 Fast Cooling

For a wind medium, the ambient density is high at early times, and the reverse shock emission might be in the fast cooling regime (Kobayahsi & Zhang 2003; see also

Laskar et al. 2013 for a low density wind model). In such a case the cooling frequency is expected to be located below the optical band, which means the optical reverse shock emission should disappear once the reverse shock crosses the shell. However we still detect the delayed high latitude emission after the deceleration time. In the local frame the spectral power (β) below the typical frequency is $\nu^{-1/2}$ and above the typical frequency $\nu^{-\hat{p}/2}$ (Sari et al. 1998). The temporal evolution of the reverse shock flux goes as $F_{\nu,r} \propto t^{-5/2}$ and $t^{-(\hat{p}+4)/2}$ for the high latitude component respectively (Kumar & Panaitescu 2000). This will modify the magnetisation estimate, as the spectral index in the final term of Equation 3.4 will change.

First we consider that the typical frequency $\nu_{m,r}(t_p)$ is located below the observational band (high frequency regime) such that the spectral index is $-\hat{p}/2$ and $\alpha_r = (\hat{p}+4)/2$. The forward shock evolution is slightly different as in Figure 3.1 the forward shock now decays as $t^{-1/4}$ prior to passage of the typical frequency across the observational band. Taking the location of the passage of the forward shock typical frequency as t_m with flux F_{ms} gives a magnetisation,

$$R_B = \left(\frac{R_F^2 \Gamma_0^{4\alpha-10}}{C_F^2 C_m^{2(\alpha-2)} R_t^{3\alpha-5}} \right)^{1/(\alpha-1)} , \tag{3.7}$$

and considering that the forward shock typical frequency passage is hidden by the reverse shock emission then,

$$R_B = \left(\frac{R_t^{5-\alpha} \Gamma_0^{4\alpha-10}}{C_F^2 C_m^{2(\alpha-2)}} \right)^{1/(\alpha-1)} . \tag{3.8}$$

When considering the dependence of this equation on the location of the forward shock typical frequency passage we get a stronger dependence $R_B \propto t_m^{-3/2(\alpha-1)}$ and $R_B \propto t_m^{3/4}$ taking $\hat{p} = 2$ with smaller dependence for increasing $\hat{p}$.

When considering the case where the reverse shock typical frequency is located above the observational band (low frequency regime) the decay index is $\alpha = 5/2$ and the

magnetisation estimate is

$$R_B = \left(\frac{R_F}{C_F C_m^{1/2} R_t^{5/4}} \right)^{4/3}, \tag{3.9}$$

taking the same forward shock configuration described for Equation 3.7. Here the direct dependence on initial Lorentz factor cancels however the estimate is secondarily dependent on Γ_0 as correction factors are functions of ξ. When considering that the forward and reverse shock components peak at the same time and the afterglow flattens when the reverse and forward shock components are comparable, the equation simplifies to $R_B = R_t^{5/3} C_F^{-4/3} C_m^{-2/3}$. We find that the magnetisation is independent of the forward shock typical frequency passage time if $\hat{p} = 3$ as $R_B \propto t_m^{(4\alpha_f - 5)/3}$ with $\alpha_f = (3\hat{p} - 1)/4$.

The spread in decay indices for the reverse shock emission in the fast cooling regime is comparable to the distribution in the slow cooling regime ($\alpha > 2.5$). In order to distinguish which regime a GRB is located based on optical afterglow alone, the evolution of the forward shock is needed. In the fast cooling regime the forward shock emission decays as $t^{-1/4}$ prior to crossing of the typical frequency ($t < t_m$) and steepens to $t^{-(3\hat{p}-2)/4}$ (Chevalier & Li 2000). This compares to the slow cooling case where prior to typical frequency crossing the observational band $F_{\nu,f} \sim$ constant and decays slightly steeper as $t^{-(3\hat{p}-1)/4}$ afterwards ($t > t_m$). Observationally it is not possible to distinguish between these two cases as the small differences could not be disentangled from the total flux when fitting reverse and forward shock components. To distinguish between the cases multi-wavelength observations would be required to distinguish based on the spectral profile.

3.2.4 Intermediate Reverse Shock Regime

The conventional estimates assume either ultra-relativistic or Newtonian reverse shock evolution, whereas typically observed GRBs are in the intermediate regime $\xi \sim 1$ prompting the application of corrective factors. By using shock jump conditions and

equality of pressure along the contact discontinuity (Nakar & Piran 2004; Harrison & Kobayashi 2013) we arrive at,

$$\xi^2 = \frac{8x^4}{(1-x)^2(2+3x+2x^2)}. \tag{3.10}$$

where $x = \Gamma_d/\Gamma_0$ is the ratio of the initial value Γ_0 and the value at the deceleration radius $r_d = l/2\Gamma_d^2$ (assuming the energy in the shocked wind medium at deceleration is $E/2$). We have followed the same process described in Harrison & Kobayashi (2013) considering the case for a wind medium. This can be used to estimate x (see the black line in the top panel of Figure 3.2) and the reverse shock temperature ($\bar{\Gamma}_d - 1$) (black line in the bottom panel of Figure 3.2), with $\bar{\Gamma}_d = 1/2(x + 1/x)$ being the Lorentz factor of the shocked shell relative to the unshocked shell, as functions of ξ_0. Equation 3.10 gives ξ for a given x at the deceleration radius, which in the thick shell regime ($\xi_0 < 1$) is equal to the initial value $\xi_0 \sim \xi$. Due to shell spreading in the thin shell regime $\Delta \sim \Delta_0 + r_d/\Gamma_0 \sim \Delta_0(1+\xi_0^2)$ and $\xi \sim \xi_0(1+\xi_0^2)^{-1/2}$ is always roughly unity at r_d (Sari & Piran 1995). This causes the flattening observed in Figure 3.2 as in the thick-intermediate regime $\xi \sim \xi_0$ and is about unity in the thin shell regime. We find that the conventional estimates are overestimated in the intermediate regime, with expected relations as $x = \xi_0^2$ and $\bar{\Gamma}_d = \xi^{-2}/2$ if $\xi_0 < 1$ and $\bar{\Gamma}_d = 1$ for $\xi_0 > 1$. We note that unlike the ISM intermediate estimate for the relativistic regime Equation 3.10 has no radial dependence.

3.3 Numerical Simulation

In order to estimate the correction factors we use a spherical relativistic Lagrangian code based on the Godunov method with an exact Riemann solver (Kobayashi et al. 1999). We do not account for MHD effects (purely hydrodynamic evolution), such that the results are valid, providing the magnetisation is not too large i.e. the ratio of magnetic to kinetic flux $\sigma \lesssim 0.1$ (Giannios et al. 2008; Mimica et al. 2009). We consider an explosion energy of $E_0 = 10^{52}$ ergs, wind density $A = 2 \times 10^{31}$ proton

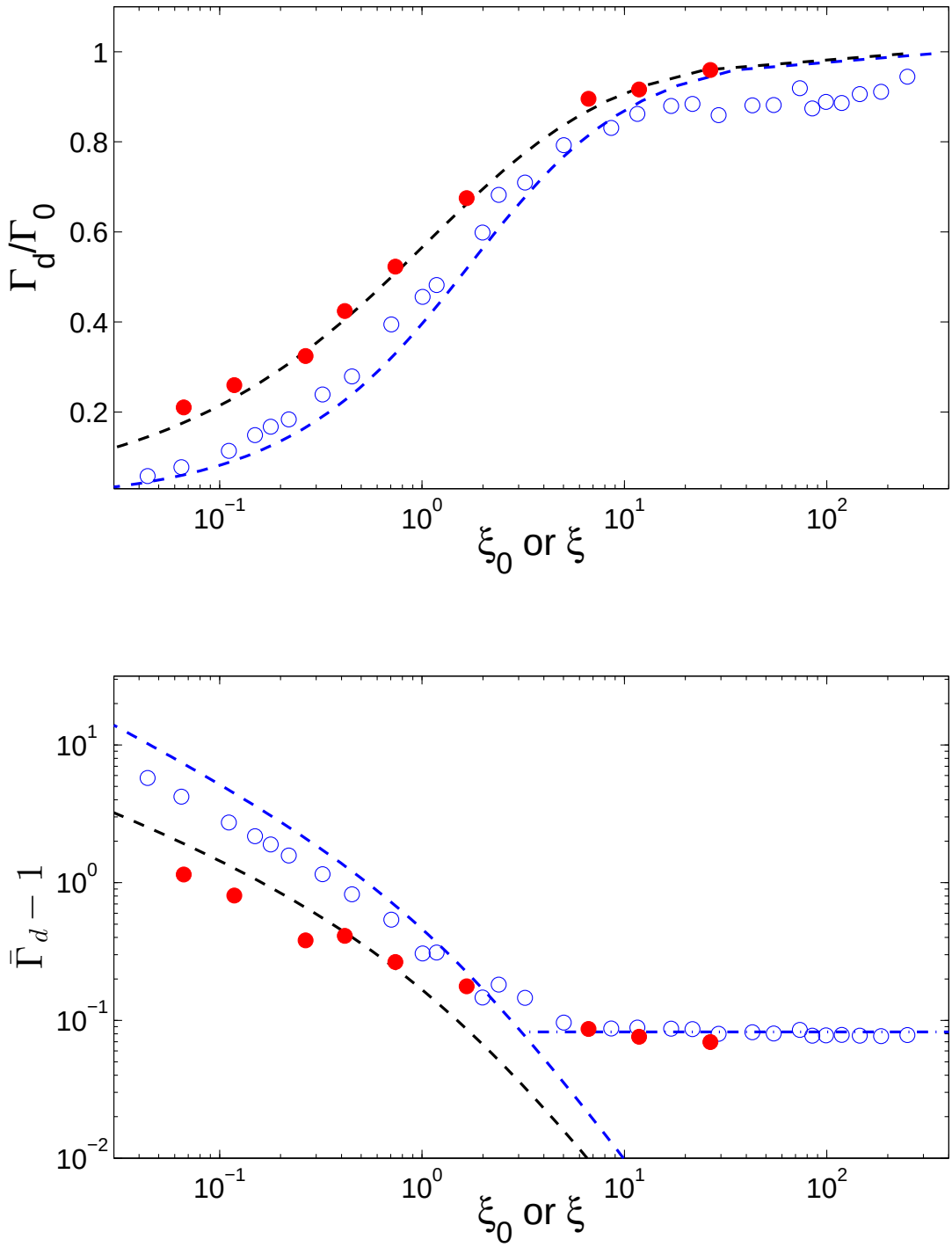

Figure 3.2: Γ_d/Γ_0 (top panel) and $(\bar{\Gamma}_d - 1)$ (bottom panel) as functions of ξ_0 or ξ. The approximation presented by Equation (3.10) (black dashed lines), and the numerical results are shown as filled red points. For comparison we have included the ISM estimate (the blue dashed line) and numerical results for the ISM case in open blue points (Harrison & Kobayashi 2013).

cm^{-1}, initial fireball size $\Delta = 6 \times 10^{12}$cm and a varying initial Lorentz factor $50 < \Gamma_0 < 1000$. This configuration allows a large coverage in $\xi_0 \propto \Gamma_0^{-2}$. We evaluate the correction factors for $R_B = 1$ and the results are valid as long as $\sigma \lesssim 0.1$.

Figure 3.2 shows the evolution of Lorentz factor Γ_d and reverse shock temperature ($\bar{\Gamma}_d - 1$) at the peak time t_p compared to the ISM case (blue; Harrison & Kobayashi 2013). All values here are averaged hydrodynamical quantities estimated by the light curve and spectrum construction described in Harrison & Kobayashi (2013). We use the peak in the reverse shock along with spectra constructed at that time to estimate the respective corrective factors as a function of ξ_0 (see Figure 3.3). Although the improved approximation accounting for the intermediate regime is a good estimate, as found previously we require numerical fitting to accurately reproduce the result of the simulations. Using the functional forms for the corrective factors we find that $C_t = N_t + \xi^{-2}$ with $N_t \sim 0.1$, $C_m = N_m + \xi^{-2}$ with $N_m \sim 4 \times 10^{-3}$ and $C_f^{-1} = N_F + M_F \xi^{-1}$ with $N_F \sim 1.4$ and $M_F \sim 1.4$. Coupling the C_t numerical fit with the equation for deceleration time we can estimate the dimensionless parameter ξ as a function of peak time and GRB duration $\xi \sim 10^{1/2}\sqrt{t_p/T_{90} - 1}$ (assuming $T_{90} = \Delta_0/c$).

3.4 Magnetisation Estimate Framework

We present a simple framework for estimating the magnetisation degree for any GRB with evidence of a reverse shock component. We consider that the emission can occur with a GRB expanding into an ISM or wind environment. We will go through the procedure to estimate the magnetisation for a single peak with late time flattening and two separated peaks (only for the ISM case). Having observations of the reverse and forward shock emission distinctly separated temporally is the ideal detection for accurately estimating magnetisation degree, although much rarer. As the magnetisation estimate has a weak dependence on the GRB energy and deceleration time, an exact distance is not required (although it is preferred). In the following procedures it is assumed that the GRB duration (T_{90}) isotropic equivalent energy (E_{iso}) and redshift (z) are known.

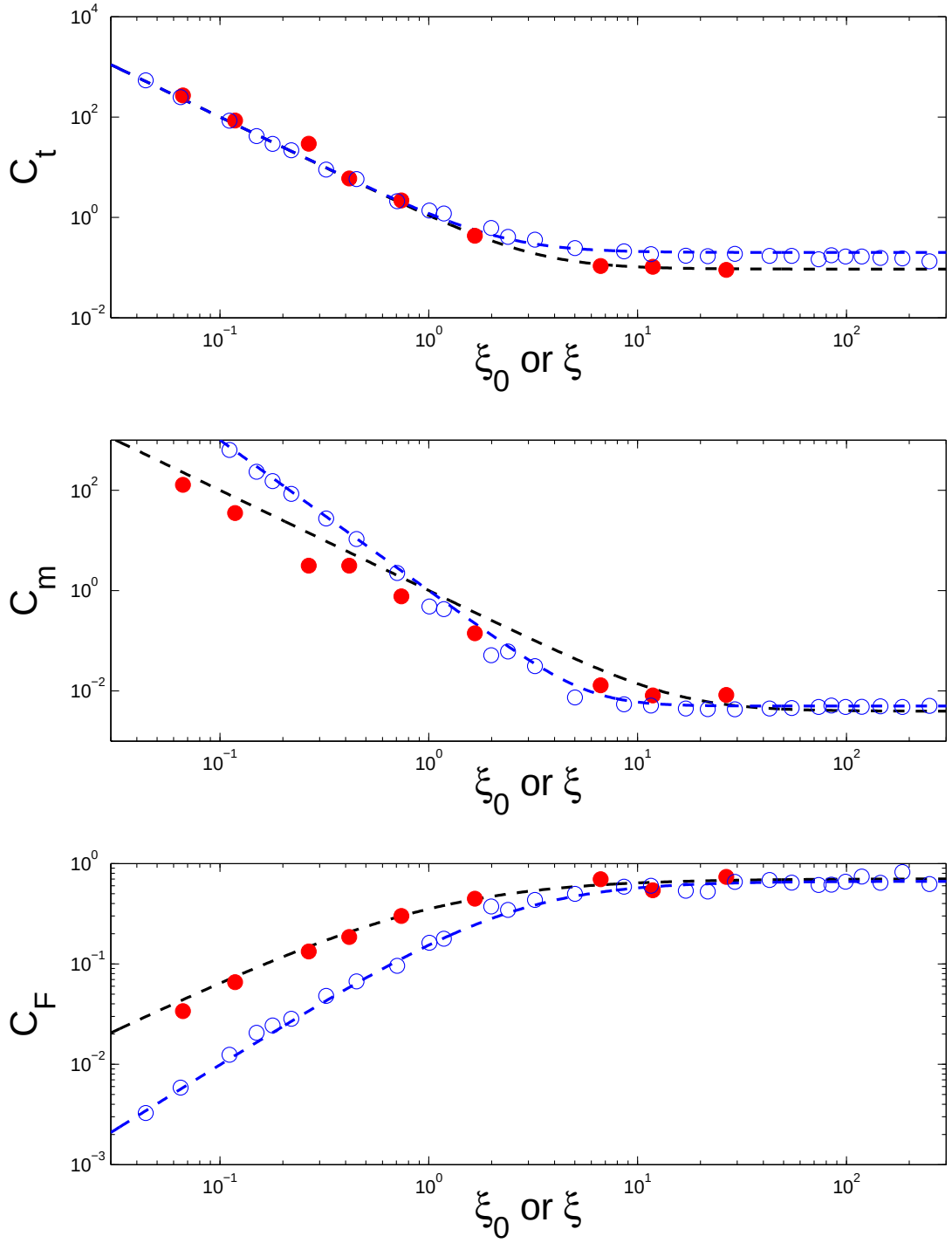

Figure 3.3: The correction factors as a function of ξ. Top panel: The normalised peak time C_t, middle panel: The normalised typical frequency ratio C_m, and bottom panel: The normalised peak flux ratio C_F. The results of the numerical simulations are filled red points and for comparison the ISM study results are in open blue points. The dashed lines give the result of numerical fitting to the correction factors (black - wind medium and blue - ISM). See the text for the fit details.

The peak (first data point if no peak is observed) of the reverse shock component is taken as the deceleration time (t_d). For all GRBs we will not constrain the external medium to ISM or wind type and calculate all parameters for each case where possible. For consistency with the previous sections we will use standard notation of wind parameters, however when specifying ISM results the parameter will be subscripted with ISM. It is possible to estimate the relativistic nature of the reverse shock emission as $\xi_{ISM} = 5^{1/2}\sqrt{t_d/T_{90} - 1}$ for an ISM and $\xi \sim 10^{1/2}\sqrt{t_d/T_{90} - 1}$ for a wind medium. If the optical afterglow peaks before the end of the prompt gamma-ray emission then we can only estimate an upper limit on $\xi < 1$. It is immediately possible to estimate the initial Lorentz factor for the ISM case, $\Gamma_{0,ISM} = (C_{t,ISM} l_{ISM}/ct_p)^{3/8}$ with $C_{t,ISM} = 0.2 + \xi_{ISM}^{-2}$ and $l_{ISM} = (3E_{iso}/4\pi m_p n_1 c^2)^{1/3}$, or $\Gamma_0 = (C_t l/ct_p)^{1/4}$ for the wind case. As we need to understand the temporal evolution of the afterglow to estimate the magnetisation we will be performing two different power law fits, using the chi-squared minimisation technique to find the best result.

3.4.1 Single Peak

For wind models a single peak is always seen and we will first consider the most common case were the passage of typical frequency is masked by the reverse shock emission. This afterglow can also be reproduced using the ISM model under the same assumption. We fit a simple broken power-law with two segments measuring the decay indices α_1 and α_2 for the first and second component respectively. This gives a shallow limit on the decay indices as it does not account for the fact that the data is a cumulative flux of two components. Also if we consider the possibility that the passage of the forward shock typical frequency across the optical band is coincident with the break in the power law, the early emission could be entirely dominated by reverse shock component with $\alpha = \alpha_1$, as the forward shock component is rising/flat prior to this time dependent on ISM/wind assumption. The peak time and peak flux are simply obtained from the data, with the flattening time and flux coming from the break location in the broken power law fit, meaning $R_{F,bpl} = F_p/F_{break}$ and $R_{t,bpl} = t_{break}/t_d$.

A second fit will assume that late time afterglow emission is purely forward shock in nature. From the visual location of the break in the afterglow, a fit is made to the data at $\gtrsim 10t_{br}$ taking this as pure forward shock emission with decay rate α_{fs}. This fit is extrapolated back to the peak and subtracted from the data to leave behind the steep component. Fitting to this subtracted afterglow will yield the reverse shock decay α_{rs}. If the forward shock peaks at the same time as the reverse shock this extrapolation would be a true representation. However if the forward shock is weaker because of the location of the typical frequency crossing time being above the deceleration time, then too much flux will have been subtracted and α_{rs} should be shallower giving a steep limit. The peak time and flux of the reverse shock component is given by the subtracted afterglow and the flattening time and flux are given by the intersection of the two components, such that $R_{f,2cf} = F_{p,sub}/F_{2cf,int}$ and $R_{t,2cf} = t_{2cf,int}/t_d$.

The magnetisation estimate for the ISM model is given by,

$$R_{B,ISM} = \left(\frac{R_t^3 \Gamma_{0,ISM}^{4\alpha-7}}{C_{F,ISM}^3 C_{m,ISM}^{2(\alpha-1)}} \right)^{2/(2\alpha+1)} \tag{3.11}$$

with the correction factors $C_{F,ISM} = (1.5 + 5\xi_{ISM}^{-1.3})^{-1}$ and $C_{m,ISM} = 5 \times 10^{-3} + \xi_{ISM}^{-3}$ determined numerically. For the wind case the magnetisation degree is calculated using Equations 3.6, 3.8 and flattening equivalent of 3.9 to consider the slow and fast cooling regimes. The wind correction factors are given in Section 3.3. Using both fits to estimate different magnetisation parameters yields the expected range of the true value.

Consider the single peak emission is only described by the wind medium and the afterglow appears as a three part broken power-law with a plateau phase separating a steep and shallow decay. In this case, at the end of the plateau phase the typical frequency of the forward shock crosses the observational band. As prior to this the forward shock is either flat or decaying, a simple broken power-law fit would not suffice as there will be significant forward shock contamination in the reverse shock emission. Therefore for this case we fit to the late time data as pure forward shock emission and estimate the decay α_{fs} (for $\hat{p}$ consistency compare reverse and forward shock predictions). From the peak to plateau phase the extrapolated forward shock emission assuming a $F_{fs} \propto t^0$

and $F_{fs} \propto t^{-1/4}$ profile (for slow and fast cooling regime respectively) and subtract from the data. This will leave a reverse shock component for the slow and fast cooling regime, which can be fitted to obtain $\alpha_{rs,sc}$ and $\alpha_{rs,fc}$. $\alpha_{rs,sc}$ can then be used in conjunction with Equation 3.5 and $\alpha_{rs,fc}$ with Equations 3.7 and 3.9 to calculate the magnetisation degree of the outflow.

3.4.2 Two Peaks

As the forward and reverse shock peaks are separated it is possible to constrain R_t and R_F using the temporal location and flux at these locations. The first fit is the simplest in that a broken power law is directly fitted to the data with three components: (1) first peak decay α_1 (2) transition to second peak $\alpha_2 < 0$ (3) and the second peak decay α_3. This will give a shallow limit on the true temporal evolution as the real afterglow is a cumulative flux of two components. The aim of the second fit is to attempt to calculate the individual reverse shock component decay. By fitting to the transition to the second peak (α_2), it is possible to extrapolate this evolution back to t_p and subtract the expected forward shock emission from the data, giving the decay index of the reverse shock α_{rs}. If their is no discernible minimum between the peaks an assumption that the forward shock has rise $\alpha_2 = 0.5$ prior to the second peak will be made to estimate α_{rs}.

The magnetisation parameter in the ISM case can be estimated using Equation 3.12 (Equation 5 in Harrison & Kobayashi 2013).

$$R_{B,ISM} = \left(\frac{R_F^3 \Gamma_{0,ISM}^{4\alpha-7}}{C_{F,ISM}^3 C_{m,ISM}^{2(\alpha-1)} R_t^{3(\alpha-1)}} \right)^{2/(2\alpha+1)} \tag{3.12}$$

with $C_{F,ISM} = (1.5 + 5\xi_{ISM}^{-1.3})^{-1}$ and $C_{m,ISM} = 5 \times 10^{-3} + \xi_{ISM}^{-3}$ are both numerical correction factors. The detection of two distinct peaks is unique in the ability to easily distinguish wind vs ISM as it is only expected under the ISM model.

3.4.3 σ Parameter

In order to understand whether the degree of magnetisation is significant enough to affect the jet dynamics (and whether our non MHD estimates are consistent) we evaluate the σ parameter (ratio of magnetic to kinetic energy). For this purpose we need the forward shock microphysical parameter $\epsilon_{B,f}$. However due to degeneracies in afterglow modelling between ϵ_e, n_1 and $\epsilon_{B,f}$ (Kobayashi & Zhang 2003) it is difficult to constrain without having spectral evolution, e.g. optical and radio data. With an estimate of $\epsilon_{B,f}$ it is possible to constrain $\sigma \simeq (\bar{\Gamma}_d - 1)\epsilon_{B,f} R_B / \bar{\Gamma}_d$. If $\epsilon_{B,f}$ cannot be constrained it can be assumed to lie within typically observed values of $\epsilon_{B,f} = 10^{-7} - 10^{-2}$ for ISM events (Panaitescu & Kumar 2002) and $\epsilon_{B,f} = 10^{-8} - 10^{-3}$ for wind type events (Santana et al. 2013).

3.5 GRB Sample

Only a handful of GRBs have early optical afterglow detections, here we apply the framework set above to a sample of 10 GRBs: GRB 990123 (Akerlof et al. 1999; Kulkarni et al. 1999), GRB 021004 (Pandet et al. 2003; Bersier et al. 2003), GRB 021211 (Fox et al. 2003), GRB060111B (Klotz et al. 2006; Stratta et al. 2009), GRB 061126 (Gomboc et al. 2008), GRB 080319B (Racusin et al. 2008), GRB 081007 (Jin et al. 2013), GRB 090102 (Gendre et al. 2010), GRB 090424 (Jin et al. 2013) and GRB 091024 (Virgili et al. 2013). Only GRB 091024 has a definite double peak structure with GRB 021004 having a two peak structure inferred from literature (Kobayashi & Zhang 2003). We will discuss these cases in more detail later. In Table 3.1 we present the redshift, isotropic equivalent energy and duration of each GRB along with the result of fitting a broken power law (α_1 and α_2) and fit after subtraction of late time forward shock component (α_{rs} and α_{fs}). Generally $\alpha_2 \sim \alpha_{fs}$, with differences arising due to reverse shock contamination in the fit of α_2. For the purpose of this study we assume that the wind normalisation A has a typical value of $m_p A \sim 5 \times 10^{11} g\ cm^{-3}$ for all GRBs in the sample. As the initial Lorentz factor $\Gamma_0 \propto A^{-1/4}$ depends weakly on A

for a given peak time t_p, as does the magnetisation and our estimates are not affected by this assumption.

Table 3.1: GRB Fits

GRB	z	$E_{\gamma,iso,52}$	T_{90}	α_{rs}	α_{fs}	α_1	$\alpha_{2/3}$
021004*	2.33	5.6	100	1.3 (1.0)	1.3	0.4	1.3
091024	1.09	42	90	2.2	1.3	1.3	1.0
990123	1.6	140	60	2.8	1.2	2.2	1.2
021211	1.004	1	5	2.2	1.0	1.8	1.2
060111B	2	5.8	60	3.7	1.2	2.1	1.2
061126	1.16	7.4	19	1.7	0.9	1.6	0.9
080319B	0.937	13	57	3.2	1.3	2.1	1.3
081007	0.53	0.15	8	1.9	0.6	1.3	0.6
090102	1.5	57.5	27	1.9	1.0	1.6	1.1
090424	0.54	4.3	48	2.2	0.8	1.3	0.8

Here we present the parameters for each GRB we consider and the result of the two fitting routines run on the optical afterglow. α_1 and α_2 correspond to the reverse and forward shock decay based on a power-law fit and α_{rs} and α_{fs} using the late time forward shock subtraction technique. *For the two component fit we have assumed at the break that the forward shock emission evolves as the slow cooling wind case, with bracketed value for assuming a rising ISM component.

3.5.1 Results

In Figures 3.4, 3.5 and 3.6 we show the optical light curves (r or R band) for each event in our sample along with resultant fit for the broken power law (dashed line) and subtracted forward shock component (solid line). We show in Table 3.2 the ranges for the two fits $R_{B,2cf} - R_{B,bpl}$ with $R_{B,2cf}$ from to the subtracted forward shock emission fit and $R_{B,bpl}$ for the simple broken power-law fit. In Table 3.3 are the magnetisation and Lorentz factor estimates assuming that the external density is a ISM. To distinguish between whether the emission is arising due to an external ISM or a wind medium, we use the expected $\hat{p}$ value to exclude models using the assumption that it must lie in the range $2 < \hat{p} < 3$ and that both forward and reverse components should give consistent values. For the wind medium we have three possible scenarios for the emission: slow cooling, fast cooling high frequency $\nu > \nu_m$ and fast cooling low frequency $\nu < \nu_m$.

After t_d the forward shock decay is independent of ξ and can be used to estimate $\hat{p}$:

Table 3.2: Wind Magnetisation Estimates

GRB	ξ	Γ_0	$R_{B,sc}$	$R_{B,fc}(\nu > \nu_m)$	$R_{B,fc}(\nu < \nu_m)$	σ
021004	6.8	$>$22	-	-	-	-
990123	1	150	**91-20**	80-5$\times10^3$	**115**-130	9$\times10^{-8}$-0.004
021211	13	$>$20	**35**-3	2.5-0	190-275	3$\times10^{-9}$-0.03
060111B	1	80	250-**4**	5$\times10^3$-0.3	5-24	9$\times10^{-9}$-16
061126	1.9	$>$60	0.1-2$\times10^3$	0-2$\times10^7$	13-2$\times10^6$	2$\times10^{-9}$-5$\times10^4$
080319B	1	$>$130	**1.2 $\times$ 10^3**-94	**4.3$\times$10^3**-30	73-30	1$\times10^{-7}$-25
081007	12.8	18	4-0.2	0.002-0	108-840	2.3$\times10^{-12}$-0.1
090102	2.5	$>$84	2.5-0.5	0.002-0	110-660	3$\times10^{-11}$-1
090424	3.1	$>$30	**20**-1	3-0	76-6.4$\times10^3$	1$\times10^{-8}$-8

Result of the wind magnetisation fits for different scenarios with magnetisation limits as $R_{B,2cf} - R_{B,bpl}$. Upper and lower limits of $\epsilon_{B,f}$ are taken as $10^{-8} - 10^{-3}$ (Santana et al. 2013) and used to estimate upper and lower limits on σ except where refined values are known: GRB 990123 (Panaitescu & Kumar 2002), GRB 021004 (Kobayashi & Zhang 2003) and GRB 080319 (Pandety et al. 2009). For completeness we use the smallest and largest possible R_B across all scenarios in the σ estimate. In bold are the favoured estimates based on the afterglow modelling.

$\hat{p} = 4\alpha_f/3 + 1$ for the ISM model, with $\hat{p} = (4\alpha_f + 2)/3$ for the slow cooling wind model and $\hat{p} = (4\alpha_f + 1)/3$ for fast cooling case, assuming always that at late times $\nu > \nu_{m,f}$. For the reverse shock component $\hat{p} = (4\alpha - 1)/3$ for the ISM model, while $\hat{p} = 4\alpha/5$ in the slow cooling wind model. When considering the fast cooling wind model it is only possible to estimate $\hat{p} = 2\alpha - 4$ when $\nu > \nu_{m,r}$ as in the low frequency regime the decay index is constant $\alpha = 5/2$. When quoting ranges in predicted $\hat{p}$ for specific models we will state the range as reverse shock to forward shock estimate ($\hat{p} = \hat{p}_{rs} - \hat{p}_{fs}$) if the difference is significant $\Delta\hat{p} \geq 0.1$. We will first present the fit result associated with the two-component cases (GRB 021004 and GRB 091024) followed by the typically observed single peak afterglows with a flattening following a steep decay phase.

Table 3.3: ISM Magnetisation Estimate

GRB	ξ	Γ_0	$R_{B,2cf}$	$R_{B,bpl}$	σ
021004*	4.8	>75	**(35)**	-	3×10^{-4}-0.004
091024	4.6	87	**380**	0.005	2×10^{-6}-0.15
990123	1	470	1.9×10^{4}	**4100**	1×10^{-4}-0.6
021211	9.2	>94	**6900**	260	3×10^{-7}-0.8
060111B	1	>400	2.7×10^{5}	**880**	3×10^{-5}-850
061126	1.3	>320	**7**	**170**	1.6×10^{-7}-0.4
080319B	1	> 386	1.8×10^{5}	**9000**	3×10^{-4}-1000
081007	9	76	**475**	4	5×10^{-9}-0.05
090102	1.8	>310	**440**	60	1×10^{-6}-0.74
090424	2.19	>129	**2200**	30	4×10^{-7}-3

Same as Table 3.2 assuming an ISM model, with a marginally higher range in $\epsilon_{B,f} = 10^{-7} - 10^{-2}$ (Panaitescu & Kumar 2000; Santana et al. 2013). *σ estimate is based on the afterglow ISM fit from Kobayashi & Zhang (2003).

GRB 021004

This case presented difficulty a in fitting forward-reverse shock components to the afterglow as the reverse shock emission was always too shallow. Kobayashi & Zhang (2003) fit the afterglow with a two component model assuming that the forward shock peaks at $t_m \sim 5 \times 10^3$seconds with prior emission rising as $F_{\nu,f} \propto t^{1/2}$. This case does reproduce the afterglow reasonably although it overestimates the forward shock region

which is rectified by considering a more rounded spectral shape (Granot et al. 1999). Our broken power law fit yields decay indices that cannot be explained by either an ISM or wind reverse shock emission as α_1 is too shallow. Considering a subtraction model and removing late time emission assuming a peak around the afterglow break, we get $\alpha_{rs} \sim 1$ and $\alpha_{rs} \sim 1.3$ for ISM and slow cooling wind model assumptions respectively (see Figure 3.4). Both of these fits are too shallow to be well explained by the reverse shock model, giving magnetisation estimates $R_B \lesssim 1$. We can, however, estimate magnetisation for the ISM case by applying the model from Kobayashi & Zhang (2003), $R_B \sim 35$ with $\Gamma_0 \sim 25$ implying a magnetised outflow. The result of this burst will not be included in our sample analysis due to the unconfirmed presence of a reverse shock, although radio detection supports reverse shock emission in the slow cooling regime from an ISM density (Kobayashi & Zhang 2003). The radio detections allow calculation of the microphysical parameter $\epsilon_{B,f} \sim 3 \times 10^{-3}$, with the above magnetisation estimate implying $\sigma \sim 2 \times 10^{-3}$. The magnetic field would not be strong enough to change the dynamics of the reverse shock evolution. It has been proposed that this event could be described by the energy injection model (Björnsson et al 2004; de Ugarte Postigo et al 2005), which could account for the poor afterglow fit with a two component model.

GRB 091024

GRB 091024 is the only GRB observed with two distinct peaks, which offers simple distinction as ISM type due to the rise of the forward shock emission. It also allows good constraints to be placed on the magnetisation and emission detected prior to the reverse shock peak, which means the Lorentz factor is well defined. As two separated peaks are observed, this event can be immediately classified as in the ISM regime and considering the subtracted fit we get $\hat{p} = 2.6 - 2.8$ with a magnetisation of $R_B \sim 380$.

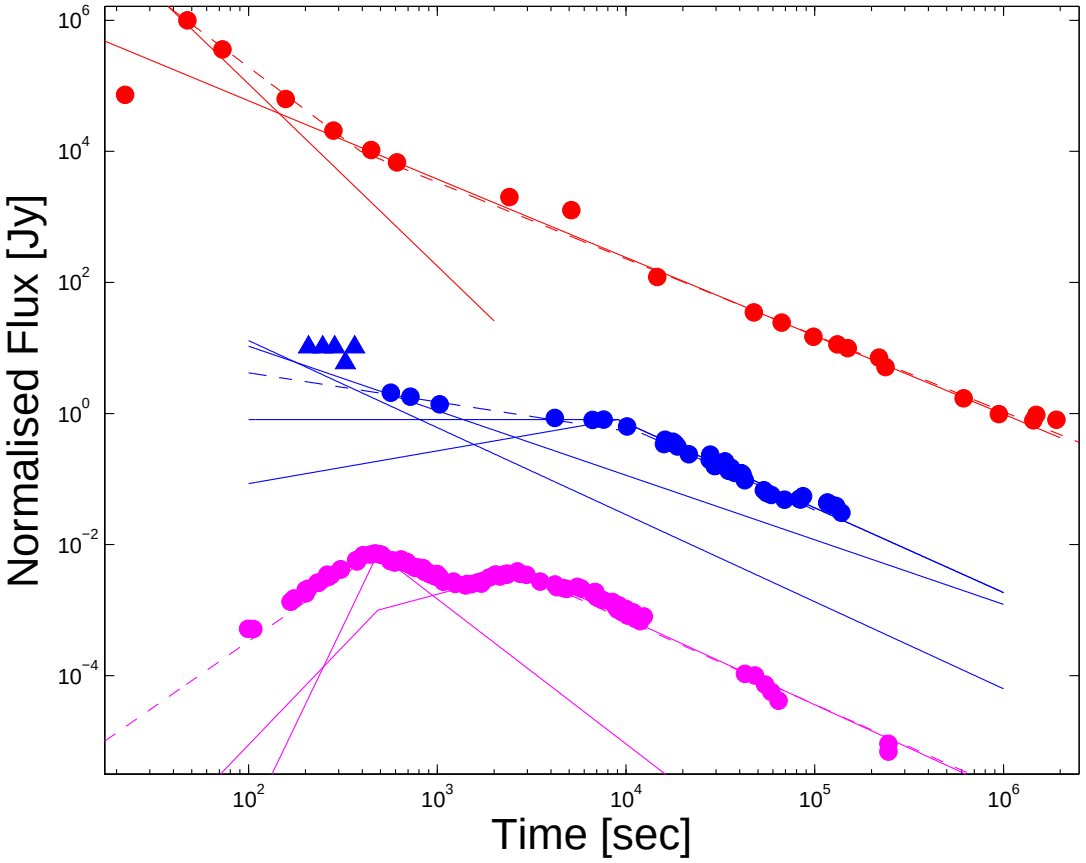

Figure 3.4: Examples of various fitting routines as applied to GRB 091024 (magenta), GRB 021004 (blue), GRB 990123 (red). The solid lines show the result of the two component fit after with forward shock subtraction of the extrapolated late time forward shock emission. The dashed line represents a simple broken power law fit. The afterglows are normalised to the peak flux and offset for plotting purposes. For GRB 021004 the origin of the emission (ISM or WIND) so we assume two cases with the emission rising and being flat prior to the forward shock break.

GRB 990123

The peak time t_d is well constrained as the afterglow had a single detection prior to the peak, with the Lorentz factor estimate for the wind medium being a factor ~ 3 smaller than the ISM estimate. This GRB is the classical reverse shock (optical flash) example with a well sampled early time steep decay. Fitting a simple broken power law gives a decay corresponding to an ISM medium with $\hat{p} \sim 2.6$, and $\hat{p} = 1.8 - 1.9$ for the slow cooling wind regime. The fast cooling regime is not applicable, as the model predicts $\alpha > 2.5$. The broken power law fit corresponds to the scenario with the forward shock peak lying close to the flattening location and gives magnetisation estimates which are acceptable and considerably smaller in the wind case. By considering the fit to the forward-shock-subtracted light curve the reverse shock component becomes steeper, favouring the wind model as $\hat{p} \sim 2.2 - 2.6$ for the slow cooling wind model and $\hat{p} \sim 3.4 - 1.8$ for the ISM model, ruling the latter out. The fast cooling high frequency model is ruled out as this estimates $\hat{p} \sim 1.6$, however the decay rate is consistent with the low frequency regime. For the subtracted afterglow fit we would expect the wind model of slow cooling and fast cooling (low frequency) to be consistent with observed decay rates. The wind model offers significantly smaller magnetisation degrees, however the reverse shock could not be suppressed by high magnetisation as $\epsilon_{B,f} \sim 10^{-6}$ is low (Panaitescu & Kumar 2004) and $\sigma \lesssim 0.1$. This event could be explained by the forward shock peaking close to the flattening with slow cooling wind or ISM models. Alternatively if $t_m \sim t_d$ then either the slow or fast (low frequency) cooling wind models could apply.

GRB 021211

The very late peak nature of this event provides a below average lower limit on the initial Lorentz factor with the wind model prediction indicating a rlow Lorentz factor outflow $\Gamma_{0,wind} > 20$. The two component fit implies a $\hat{p} = 1.8 - 2$ for the slow cooling wind model and $\hat{p}$ being much smaller for the broken power law fit. However the ISM model is well explained by both regimes as $\hat{p} \sim 2 - 2.7$ for the broken power law fit

and $\hat{p} \sim 2.6 - 2.4$ for the subtracted forward shock fit. The two component fit ISM model and slow cooling wind model appear as best fits for this event with the later having a magnetisation estimate 2 orders of magnitude smaller.

GRB 060111B

For this event both reverse shock fits give steep estimates on the decay rate. For the broken power law fit the decay indices indicate $\hat{p} \sim 2.5$ for the ISM model and $\hat{p} \sim 1.7 - 2.2$ for the slow cooling wind model, and α_1 is too shallow to accommodate the fast cooling regime. For the two component fit the steep nature rules out the ISM model ($\hat{p} = 4.6 - 2.6$), the slow cooling wind model gives $\hat{p} \sim 3.0 - 2.3$ and the high frequency fast cooling case $\hat{p} \sim 3.4 - 1.9$, with α_r being too steep for the low frequency case. This indicates that the forward shock peak is likely to be closer to the break in the afterglow (broken-power law fit giving best estimate), meaning we consider the magnetisation estimates of $R_B = 880$ and 4 for the ISM and slow cooling wind models respectively.

GRB 061126

Both fitting routines return a shallow reverse shock component which rules out the wind model as $\hat{p} < 1.4$. There is very little difference in the temporal fit of each technique with ISM magnetisation difference arising in the estimates of R_t and R_F (see Figure 3.5, red lines). The temporal evolution indicates that $\hat{p} \sim 1.8 - 2.2$ with a magnetisation in the range $R_B \sim 7 - 170$ for an ISM type circumburst density.

GRB 080319B

The broken power law fit implies that $\hat{p} \sim 2.3 - 2.7$ for an ISM density profile and $\hat{p} \sim 1.7 - 2.4$ for a wind medium in the slow cooling regime. The decay is too shallow to accommodate the fast cooling regime. This fit favours the ISM model which predicts a high magnetisation degree of $R_B \sim 9000$. However when considering the

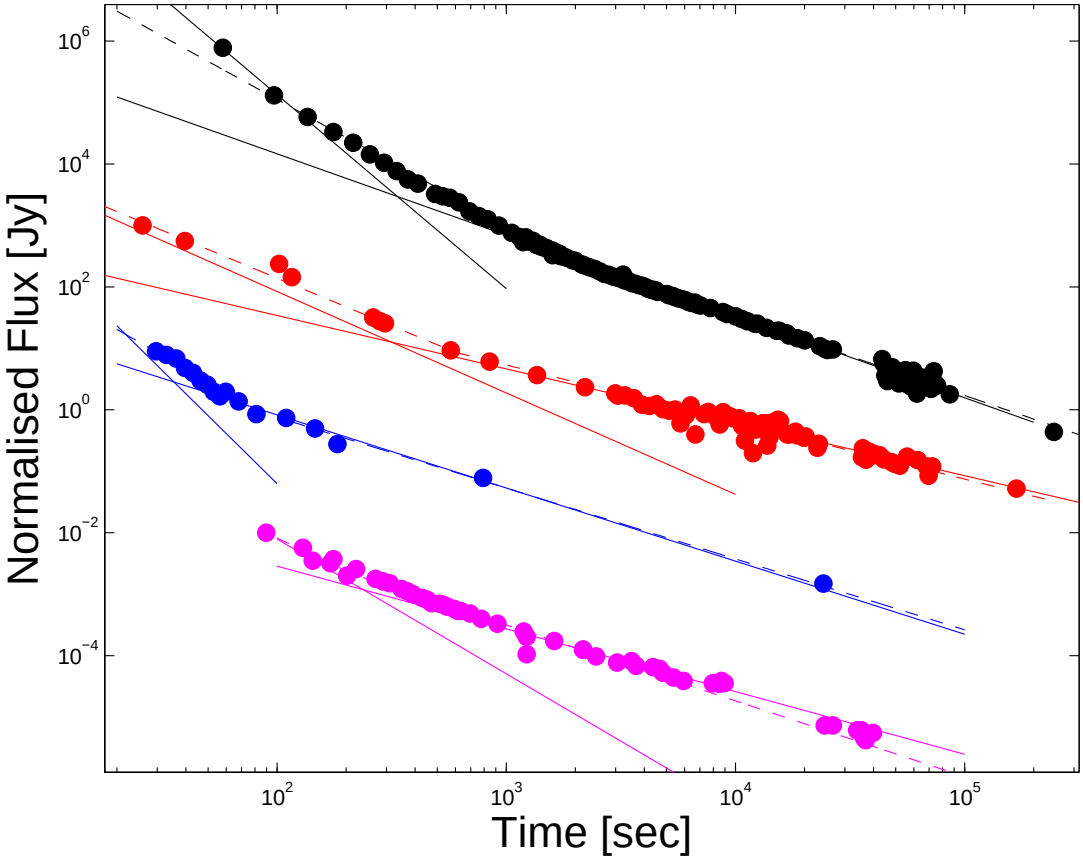

Figure 3.5: Same as Figure 3.4 except for GRB 021211 (magenta), GRB 060111B (blue), GRB 061126 (red) and GRB 080319B (black).

two component fit we see the wind model is favoured due to the steeper reverse shock component. The slow cooling wind medium requires $\hat{p} \sim 2.6 - 2.4$ and for the fast cooling regime we require the high frequency regime and $\hat{p} \sim 2.1$. The reverse shock emission decay is too steep for the low frequency case. The magnetisation should be high although poorly constrained.

GRB 081007

Similar to GRB 061126, both fits give a decay that is too shallow to be associated with a wind type medium ($\hat{p} < 1.6$). For the broken power law fit $\hat{p} \sim 1.4 - 1.8$ and for the two component fit $\hat{p} \sim 2.2 - 1.9$ with the ISM model. This indicates that the forward shock peak is likely close to the reverse shock peak and the magnetisation is $R_B \sim 475$.

GRB 090102

GRB 090102 was the first GRB to have a large optical polarisation detection (Steele et al. 2009) indicating a magnetised outflow, as the emission was associated with an early reverse shock component. For both fits the reverse shock decay indicates that for any wind model $\hat{p} < 1.6$, ruling out these magnetisation estimates. Considering an ISM model, $\hat{p} \sim 2.2 - 2.4$ for the two component fit and $\hat{p} \sim 1.75 - 2.4$ for the broken power law fit. Suggesting that the two component fit gives the best approximation, with the forward and reverse shock peaking at t_d and a magnetisation of $R_B \sim 440$.

GRB 090424

The decay indices for the broken power law fit are too shallow to be explained well by either ISM or wind models as $\hat{p} < 1.4$. This indicates that the forward shock is likely to peak at a similar time to the reverse shock component, making the two-component fit more realistic. With the two-component fit the ISM model predicting $\hat{p} \sim 2.6 - 2.1$ and the slow cooling wind model gives $\hat{p} \sim 1.8$. The fast cooling regime decays too

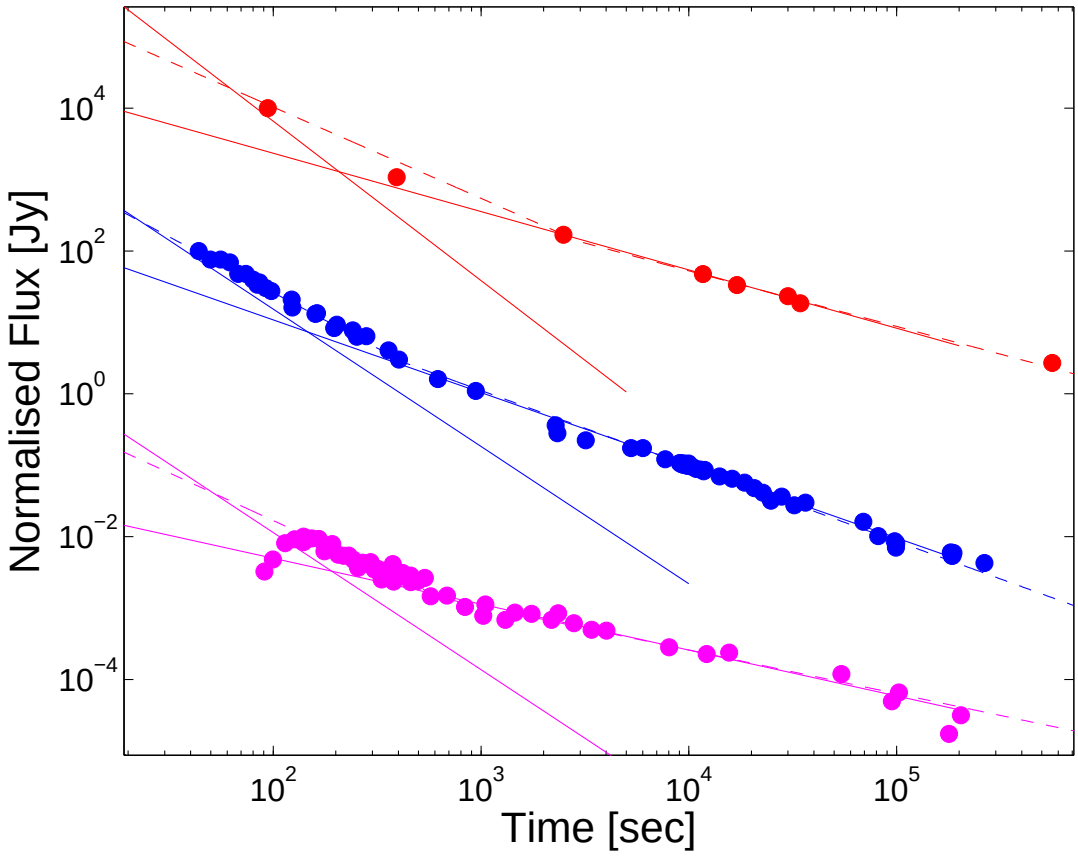

Figure 3.6: Same as Figure 3.4 except for GRB 081007 (magenta), GRB 090102 (blue) and GRB 090424 (red).

quickly to explain this case.

3.6 Discussion and Conclusions

We have derived an improved method to estimate the GRB fireball magnetisation in a wind type medium ($n_1 = AR^{-2}$). By using ratios of observed afterglow properties, the weaky constrained microphysical parameters cancel (ϵ_e and $\hat{p}$) allowing accurate estimates of the magnetisation degree. Combining this result with that of Harrison & Kobayashi (2013) have allowed us to calculate the expected wind and ISM magnetisation degrees for a sample of 10 GRBs that exhibit an early steep decay phase indicative of reverse shock emission. In Tables 3.2 and 3.3 we show the wind and ISM magnetisation fits for different scenarios and in bold face highlight the favoured values based on the optical data. Although the ISM model produces acceptable fits for all cases, 5 of the 10 can be explained by a wind medium, which offers much smaller magnetisations. As $\epsilon_{B,f}$ is poorly constrained from optical observations alone (Panaitescu & Kumar 2000; Santana et al. 2013), it is difficult to tightly constrain the σ parameter. Considering the ISM case, GRB 021004 and GRB 061126 are best favoured for a purely baryonic outflow inferred from magnetisation estimates as even with a large range in $\epsilon_{B,f}$, we still have $\sigma \lesssim 0.1$. If GRB 990123, GRB 021211, GRB 060111B and GRB 090424 are best described by the wind model (afterglow can be fitted with both cases), then these can also be constrained as purely baryonic jets from their small magnetisation estimates.

It is immediately apparent from the result of fitting to the GRB data, that the Lorentz factor and magnetisation estimates are intrinsically smaller when considering the wind model over the ISM case. The main difference in magnetisation arises from the evolution of the forward shock flux. In the wind regime the maximal forward shock flux ($F_{\nu,max,f}$) decays with time as $t^{-1/2}$, meaning at later times we expect a stronger reverse shock component relative to the forward shock when compared with the ISM model (as $F_{\nu,max,f}$ is constant) requiring a smaller magnetisation. A second difference comes in the determination of $\hat{p}$ from α, and using the wind estimate always yields a

lower $\hat{p}$ for fixed α. The correctional factors are generally equivalent for the two cases i.e. for $\xi \sim 1$ (C_F is slightly smaller) the additional R_t dependence coupled with the lower $\hat{p}$ are causing the drastically smaller R_B for the wind model. In the fast cooling case there are added complications as the spectral dependence changes.

Within our sample 4 of the 10 GRBs (091024, 061126, 090102 and 081007) seem to be well explained by the ISM model. The other cases cannot be directly ruled out and depend on the assumptiosn going into the data fitting (e.g. forward shock peak location). We conclude that the fraction of events classified as wind interacting can be $\lesssim 5$ of the 10 of our sample. This division is consistent with studies of general GRB afterglows with the relative fraction of wind type events being $> 7/16$ GRBs (Zeh et al. 2006), although studies such as Panaitescu & Kumar (2003) indicate that a homogeneous medium better explains most GRB events. A recent study by Yi et al. (2013) considered the case of a general external medium profile that the outflow propagates into $n_1 = (R/R_0)^{-k}$. From a sample of 19 GRBs they imply that these have a typical density profile index of $k \sim 1$, and conclude that this indicates a potential new mass loss evolution for the progenitor star. This result is also consistent with the study by Liang et al. (2013) and detailed modelling by Leventis et al. (2013). The forward shock evolution always goes as $\nu_m \propto t^{-3/2}$, independent of the external profile such that differences arise from the maximal flux of the forward shock evolution $F_{\nu,max,f} \propto t^{-k/2(4-k)}$ and dependence of $\hat{p}$ on α. Given that we consider $k = 0$ and 2 cases, this potential new mode would intuitively have magnetisation estimates located between cases considered here, which would still imply a magnetised outflow ($R_B > 1$).

For GRB 091024 we derive a slightly higher magnetisation compared to Virgili et al. (2013), as they use information from the rising index of the reverse shock emission to better constrain ξ, giving a lower value than that inferred from t_d and T_{90} alone and a smaller ξ leads to a lower R_B estimate. GRB 990123 was difficult to distinguish between the ISM and wind case based on the optical afterglow alone, however this was also a unique case with radio emission which can place further constraints on the GRB jet parameters (Kulkarni et al. 1999). By including the radio observations the

wind model is ruled out as in this case $\nu_c < \nu$ which would cause the reverse shock predictions to fail (Nakar & Piran 2005). However, Panaitescu & Kumar (2004) argue that the wind model matches the data reasonably well, except for the expected wind density required A being smaller than the progenitor expected values by a factor of 10. GRB 021211 was originally classified as an ISM type burst as the presence of a long-lived reverse shock argued against the wind model because ν_c should be below the optical band causing the reverse shock emission to decay quicker (Fox et al. 2003). However additional multi-colour observations indicate the possibility that the event could be well described also by the wind model (Nysewander et al. 2006). Based on optical fitting alone it is not possible to distinguish between the two cases. As the wind regime predicts $\Gamma_0 > 20$ with a value of $\Gamma_0 \sim 35$ if $t_d = T_{90}$ being small compared to typical GRBs and the modelling seems to favour the ISM such that $R_B \sim 260 - 6900$. The large range in allowed decay indices for the reverse shock component in GRB 060111B makes constraining the nature of the circumburst medium difficult, although the outflow likely has a large magnetisation. GRB 061126 had a magnetisation degree estimated as $R_B \sim 50$ (Gomboc et al. 2008) which lies in the range of values expected from our fitting routine ($R_B \sim 7 - 170$) with the expected initial Lorentz factor being greater $\Gamma_0 > 320$. For GRB 080319B, even with multi-wavelength observations, the nature of the surrounding medium could not be constrained to either wind or ISM density (Pandey et al. 2009). Both magnetisation estimates indicate that the outflow should be highly magnetised. Pandey et al. (2009) constrain $\epsilon_{B,f} < 3 \times 10^{-3}$, and taking the highest limit in $R_B < 1.8 \times 10^5$ indicates $\sigma < 170$. Given that both $\epsilon_{B,f}$ is an upper limit and R_B could be as small as 30, $\sigma < 0.1$ is likely satisfied and the jet would be baryonic in nature. In the case of GRB 081007, the likely scenario is the expansion into an ISM density with a forward shock peak at a similar time to the reverse shock. This gives a large magnetisation of $R_B \sim 475$, much greater than the value predicted by Jin et al. (2013) of $R_B \sim 10$, indicating a highly magnetised outflow. Finally for the GRB 090424 afterglow fitting indicates that the GRB has a forward shock peak close to the reverse shock peak in an ISM or wind type medium. The ISM model is slightly favoured due to the smaller value of $\hat{p}$ compared to the wind model. For the ISM case we expect a very highly magnetised outflow $R_B \sim 2200$,

greater than that found by Jin et al. (2013) who obtained $R_B \sim 10$. It is possible to obtain a lower magnetisation by considering the wind case with $R_B \sim 31$.

Due to the unknown nature of the emission, some cases have poorly constrained magnetisation degrees meaning there is difficulty in understanding the dynamics. With radio detections available for a few of cases (GRB 990123, 201004, 080319B), the estimate of $\epsilon_{B,f}$ for the whole sample is difficult due to degeneracy in the synchrotron parameter estimation in the optical regime (Sari et al. 1998; Kobayashi & Zhang 2003). This means that only limits can be placed on σ using typical ranges in $\epsilon_{B,f} \sim 10^{-8} - 10^{-2}$ (Panaitescu & Kumar 2002; Santana et al. 2013), which are insufficient to constrain any of our sample in the definitive high $\sigma \geq 0.1$ regime, which would imply a Poynting flux dominated flow. This result is potentially due to the fact that we require reverse shock emission to measure the magnetisation and the fact we observe the reverse shock implies the magnetic field is insufficient to quench this component, biasing our sample.

As a consequence of the magnetisation estimate we find for this sample that the initial Lorentz factors span a range of $\Gamma_0 \sim 75 - 500$ for an ISM model and $\Gamma_0 \sim 20 - 150$ for a wind type medium. However, we note that the constant A parameter used means that Γ_0 for the wind medium could change by a factor ~ 1.8 if A changes by an order of magnitude from $5 \times 10^{11} g\ cm^{-3}$.

Here we have assumed the evolution of a simple impulsive fireball explosion. One may also consider the scenario with a central engine that launches material with a range of velocities such that as the quicker material initially decelerates, and the shell is 'refreshed' as slower moving material provides additional energy (Rees & Mészáros 1998; Kumar & Piran 2000; Sari & Mészáros 2000; Zhang & Mészáros 2001). This would cause the temporal decay of the afterglow to be shallower in the reverse and forward shock components and could apply to the cases of GRB 091024, 021004, 061126, 081007 and 090424. Equation 3.2 would remain unchanged when considering the energy injection scenario, as it would only influence post deceleration dynamics, assuming the model of Sari & Mészáros (2000). The post-deceleration temporal decay could have several breaks associated with the energy injection switching off along with the

usual transitions considered in this chapter. Therefore the inclusion of energy injection would affect the assumption in post deceleration spectral and temporal evolution of the forward and reverse shock components that go into the magnetisation estimate.

Chapter 4

Very Early Afterglow Dependence on the GRB Outflow Profile

4.1 Introduction

GRB optical afterglows have been modelled by fading emission (e.g. Kann et al. 2008). However, recently observations have been taken early enough to discuss the rising portion of the afterglow. Recent studies have started to generate samples of GRB afterglows detected before they peak (onset of afterglow), allowing extra insights into the operation of the GRB central engine. At early times the optical component can contain emission comparable to the gamma-ray component (Verstrand et al. 2005) as well as standard afterglow features (Akerlof et al. 1999). Panaitescu & Vestrand (2008) uncovered two classes of early afterglow for events which show the onset of afterglow. These are fast rising with an early peaking afterglow and slow rising with a late peak. Melandri et al. (2010) investigated the deceleration time t_p for a sample of 19 GRBs. They find that GRBs with $t_p \sim T_{90}$ (T_{90} is the gamma-ray duration of the event), have steeper rising indices compared to GRBs with a high t_p/T_{90} (thin shell case). Standard theory predicts that the forward (reverse) shock emission should have a steep rise in the thin shell regime and shallow rise in the thick shell regime prior to the fireball deceleration (Kobayashi 2000). Nakar & Piran (2004) show that a second

order polynomial fits well the evolution of the reverse shock rising index between these two regimes, implying a smooth evolution. The standard theory therefore predicts a positive correlation between the rising index and t_p/T_{90}. A positive correlation was not seen by Melandri et al. (2010), however there was an indication of a negative corralation.

These predictions are based on the standard assumption that a GRB outflow has homogeneous density and velocity profiles. As deceleration occurs after the coasting phase, the outflow is cold and the pressure profile is irrelevant in the afterglow evolution although is expected to follow the density profile. Let us consider the internal shock scenario with gamma-ray emission originating from collisions of shells. In this case the velocity profile could be roughly homogeneous at late times when the reverse and forward shocks form. However, the density profile would be inhomogeneous due to the shell collisions causing variations in the afterglow (Nakar & Piran 2005; Maxham & Zhang 2009; Vlasis et al. 2011; Harrison et al. in prep), such as flaring. In this chapter, we will consider the effect of non-uniform shell density profiles on the afterglow evolution prior to deceleration (compared to recent studies which investigate post deceleration effects e.g. Vlasis et al. 2011).

In Section 4.2 we will set up a model to predict the pre-deceleration evolution of the relativistic outflow as a function on the initial conditions (energy, shell width and velocity, which define the relativistic nature of the GRB) and the density profile of the shell. In Section 4.3 we describe the numerical simulations used to test our model and present the results in Section 4.4. Finally we discuss this result in Section 4.6.

4.2 Shock Evolution

GRB afterglows can be well explained by the deceleration of a relativistic outflow (e.g. Piran 2004; Zhang & Mészáros 2004) with the formation of shocks dissipating internal energy through synchrotron radiation. The key focus for understanding GRBs comes from the nature of their generated relativistic outflow. In the standard model, the out-

flow is assumed to be baryonic in nature (see also Komissarov et al. 2009 for Poynting flux dominated models). Initially, multiple hot fireballs (or a highly irregular fireball) expand into a homogeneous interstellar medium (ISM). The system goes through a phase of acceleration creating highly relativistic shells. When the shell's internal energy is consumed, the system transforms to coasting shells of total width Δ, which reflects the central engine operation time (Kobayashi et al. 1999). During this phase inhomogeneities in the velocity profile of the shells cause internal shocks, generating the observed prompt emission (Rees & Meszaros 1994; Kobayashi et al. 1997; Daigne & Mochkovitvh 1998). After the internal shock phase the velocity irregularities are levelled off, with the density irregularities expected to remain. However, for the standard model it is assumed that the shell is hydrodynamically homogeneous after this phase. At later times when a significant fraction of the outflow energy is transferred to the ISM, the outflow decelerates. Two shocks are formed: a forward shock that propagates into the ISM and a reverse shock that propagates into the shell. The forward shock is always ultra-relativistic (Sari & Piran 1995) however the reverse shock nature can be defined by the dimensionless parameter $\xi_0 = (l/\Delta)^{1/2}\Gamma_0^{-4/3}$. There are two extremes with $\xi_0 << 1$ being in the thick shell regime and $\xi_0 >> 1$ in the thin shell regime. This occurs at $R_\gamma \sim l/\Gamma_0^{2/3}$ for the thin shell regime and $R_\Delta \sim l^{3/4}\Delta^{1/4}$ for the thick shell case.

For homogeneous shells the rising index of the GRB afterglow depends on ξ_0, and is t^6 and t^3 for reverse and forward shock respectively in the thin shell regime and $t^{0.5}$ and $t^{0.5}$ in the thick shell regime (Kobayashi 2000; Nakar & Piran 2004). Here we give the rising index of the afterglow peak by assuming that the outflow has a density gradient. This model is primarily in terms of reverse shock evolution, although we will discuss how the result can also be easily applied to model forward shock emission.

4.2.1 Density Profile

We consider a simple deviation from the standard assumption on the outflow profile, to investigate its influence on the afterglow evolution. We assume that the density profile

has a gradient, and we discuss how this gradient affects the rising index of the reverse and forward shock emission, with velocity and pressure assumed to be uniform in the outflow. We will first consider that the inner part of the outflow has a higher density than the outer (leading) edge, such that the reverse shock encounters a higher density profile (inner high density case: IH) compared to the standard homogeneous outflow model. We will then consider the opposite case, with the density decreasing from outer to the inner region (outer high density case: OH). Since observed GRBs are typically in the intermediate regime, shell spreading is not relevant (Sari & Piran 1995) and the outflow is assumed to have a constant width prior to deceleration.

Inner High Density Case

Here the density of the shell at the inner edge (ρ_Δ) is higher than that at the outer (leading) edge (ρ_0), IH case. We consider the following density distribution,

$$\rho_4 = \rho_N \left(\frac{r}{\delta} + 1\right)^n \quad (n > 0). \tag{4.1}$$

r is the distance from the contact discontinuity and runs from 0 to $\Delta \sim cT_{90}$, δ is a normalisation factor that controls the density ratio between the inner and outer edges of the outflow (ρ_Δ/ρ_0) and $\rho_N \equiv \kappa E/(4\pi R^2 \Gamma_0^2 \Delta c^2)$ is the overall density normalisation. By assuming that the inner ($r = \Delta$) and outer ($r = 0$) edges of the outflow have initial densities (ρ_Δ and ρ_0 respectively) with a fixed ratio we arrive at $\delta = \Delta[(\rho_\Delta/\rho_0)^{1/n} - 1]^{-1}$. The coefficient κ is chosen such that the outflow has a total mass of $E/\Gamma_0^2 c^2$ (equivalent to the total mass for a homogeneous shell), and $\kappa = (n+1)(\Delta/\delta)[(1 + \Delta/\delta)^{n+1} - 1]^{-1}$. We use the standard notation to describe the shocked and un-shocked regions: (1) un-shocked ISM, (2) forward shocked ISM, (3) reverse shocked shell and (4) un-shocked shell. Using the outflow density profile it is possible to estimate the Lorentz factor of the shocked region for a given radius R and a reverse shock location r.

$$\xi^3 = \frac{24x^4}{\kappa(1-x)^2(2+3x+2x^2)} \left(\frac{r}{\delta} + 1\right)^{-n} \left(\frac{R}{R_\Delta}\right)^2 \tag{4.2}$$

We have assumed that the outflow is cold i.e. the internal energy is negligible and the initial Lorentz factor is constant through the outflow Γ_0, and $x = \Gamma/\Gamma_0$ is the ratio of the Lorentz factor at a given radius R. We also operate under the assumption the shell has a mildly (intermediate case)-relativistic reverse shock evolution, such that Δ and therefore ξ are constant with radius. Since the location of a reverse shock r is a function of R, the solution of Equation 4.2 gives x as a function of R for given parameters: l, Δ, Γ_0, ρ_Δ/ρ_0 and n.

Outer High Density Case

By considering that the outer edge of the shell has higher density that the inner boundary $\rho_0 > \rho_\Delta$, then the reverse shock encounters an ever-decreasing density (OH case). This can be achieved by replacing r in Equations 4.1 and 4.2 with $(\Delta - r)$, n is still a positive constant. In the following calculations we will consider the IH case ($\rho_\Delta > \rho_0$), with a full description of the OH scenario in appendix B.

4.2.2 Afterglow Analytic Estimate ($n = 1$)

In order to calculate the afterglow light curve before the deceleration time ($t \lesssim t_p = \Delta/c$), we need the location r of the reverse shock as a function of the shock radius R. The time it takes for the reverse shock to cross a distance dr in the shell material can be given in the following form

$$dR \simeq \mu\Gamma_0 \left(\frac{\rho_4}{\rho_1}\right)^{1/2} dr \tag{4.3}$$

(Sari & Piran 1995; Kobayashi 2000) μ is an order of unity constant. R is the radius of the shell and since the motion of the shell is highly relativistic, we can regard R/c as time in the lab frame. Here we consider the case where $n = 1$ for simplicity. By

integrating Equation 4.2.2 we obtain,

$$r = \delta \left[\left(\frac{R^2}{\mu} \left(\frac{27\Delta}{16\kappa l^3 \delta^2} \right)^{1/2} + 1 \right)^{2/3} - 1 \right]. \tag{4.4}$$

This can then be used in conjunction with Equation 4.2 to get the shocked region Lorentz factor as a function of radius R. By integrating Equation 4.2.2 between 0 and Δ we obtain the shock crossing radius R_Δ.

$$R_\Delta = \left(\frac{16\kappa l^3 \Delta^2}{27\delta\mu^2} \right)^{1/4} \tag{4.5}$$

This represents the radius that we will consider the afterglow peaking at (also known as the onset of afterglow), and by calculating the afterglow up to this point, gives the rising index. Evolution after this point will be in accordance to standard deceleration models (e.g. Kobayashi 2000) and is not considered here.

The shock jump conditions provide the pressure and density in the reverse shock shell as $\rho_3 \sim \rho_4(4\bar{\Gamma} + 3)$, and $p_3 \sim \rho_3(\bar{\Gamma} - 1)c^2$ (Blandford & McKee 1976). The spectral characteristics of the reverse shock synchrotron emission are given by using the hydrodynamical quantities as $\nu_{m,r} \propto \Gamma p_3^{5/2} \rho_3^{-2}$ and $F_{\nu,max,r} \propto \Gamma p_3^{1/2} N_{e,r}$ (Sari et al. 1998). The number of electrons in the shocked region is $N_{e,+} = (E\kappa)/(\Gamma_0^2 \Delta)(r + r^2/2\delta)$. We assume that the typical frequency is below the observational frequency such that $F_{\nu,r} = (\nu_{obs}/\nu_{m,r})^{-(\hat{p}-1)/2} F_{\nu,max,r}$. To convert the emission from lab frame to observer frame we integrate $dt_{obs} \sim dR/2c\Gamma^2$ with the assumption that all photons in the shell are emitted at the contact discontinuity (leading edge). This framework provides a semi-analytical model giving how the reverse shock emission should depend on the initial conditions ξ and the density profile of the ejecta (n and δ) prior to deceleration.

If we consider forward shock emission then $\gamma_2 = \Gamma$ with $\rho_2 \sim 4\rho_1\Gamma$ and $p_2 \sim \rho_2 \Gamma c^2$. The synchrotron dependency is the same ($\nu_{m,f} \propto \Gamma p_2^{5/2} \rho_2^{-2}$ and $F_{\nu,max,f} \propto \Gamma p_2^{1/2} N_{e,f}$), however the number of electrons in the forward shock region evolves as $N_{e,f} \propto R^3$ with $F_{\nu,f} = (\nu_{obs}/\nu_{m,f})^{-(\hat{p}-1)/2} F_{\nu,max,f}$ for our preferred frequency range ($\nu_m < \nu_{obs} < \nu_c$).

The coefficient μ in Equation 4.2.2 actually weakly depends on the strength of the reverse shock. It varies between the relativistic and Newtonian reverse shock limits, $\mu = 1/2$ and $\sqrt{9/14}$ respectively (Sari & Piran 1995). It can be easily shown that this coefficient at the deceleration radius varies smoothly as a function of ξ between these two limits with $\mu \sim 0.7$ for $\xi \sim 1$. The coefficient depends on radius also because in the thick shell or intermediate regime the reverse shock evolves from Newtonian in coasting phase ($\Gamma = \Gamma_0$) to relativistic (or intermediate) by deceleration ($\Gamma = \Gamma_d$). At smaller radii ($R << R_\Delta$) the reverse shock is always Newtonian such that $\mu \sim \sqrt{9/14}$. As radius increases towards the deceleration radius, if the initial conditions are in the thin shell regime μ will not change much, however when in the thick shell regime, by the deceleration radius μ will evolve smoothly from $\sim \sqrt{9/14}$ to $\sim 1/2$. For simplicity, we have assumed $\mu = 0.7$ in Equation as we consider the intermediate case GRBs ($\xi \sim 1$). The detection of a rising index is expected to occur just prior to the peak time optically, such that μ is not expected to vary much with a small change in radius making our assumption of $\mu = 0.7$ reasonable.

4.2.3 Limiting Case

Let us return to Equation 4.1 and consider the limit where $\rho_\Delta/\rho_0 >> 1$ and $\Delta/\delta >> 1$, meaning that the density equation simplifies to $\rho_4 = \rho_N (r/\Delta)^n$ with $\kappa = 1 + n$. In Equation 4.2 $(r/\delta + 1)^{-n}$ is replaced with $(r/\Delta)^{-n}$ and the location of the reverse shock is given by

$$r = \left[\frac{n+2}{2} \frac{R^2}{\mu} \left(\frac{3\Delta\delta^n}{\kappa l^3} \right)^{1/2} \right]^{2/(n+2)} . \tag{4.6}$$

The afterglow evolution now becomes dependent on n alone. For simple comparison, consider the thick and thin shell limits with the reverse shock typical frequency below the observational frequency in the slow cooling regime. Prior to deceleration the shocked region Lorentz factor for the reverse shock goes as $\Gamma \propto R^0$ for the thin shell estimate and $\propto \rho_4^{1/4}$ in the thick shell case. Following this we derive $\alpha_{rs} \sim 3\hat{p} - 3/2 + \frac{5n(1-2\hat{p})}{2(n+2)}$ for the thin shell reverse shock and $\alpha_{rs} \sim 5n/4 + 1/2$ for the thick shell limit. For $n = 0 - 4$ the rising index lies in the range $\alpha \sim -1$ to

6. Considering our model and assuming $\xi \sim 1$, then for the IH density regime with $n < 5$ gives $1.3 < \alpha_{rise} < 4$ and $0.7 < \alpha_{rise,fs} < 5$ allowing for steep forward and reverse shock emission also. However, when considering a power law density profile with large density contrast between inner and outer shell boundaries, leads to a difficulty in defining the effective width of the shell. The steep nature of the power-law profile causes most of the mass to be associated with a very small region of the outflow, and the size must be re-evaluated and the density profile would no longer be consistent with the gamma-ray profile.

4.3 Numerical Simulations

We employ a spherical relativistic Lagrangian code based on the Godunov method including an exact Riemann solver to simulate the relativistic outflow (Kobayashi et al. 1999). The simulation starts at $R \sim R_{\Delta}/100$ when the outflow is in the coasting phase. We consider the density distribution described in Equation 4.1, while the Lorentz factor is assumed to be uniform. As the ejecta is in the coasting phase, it is cold, and we assume $p_4 \sim \rho/10^6$, and the evolution does not depend on whether the pressure is homogeneous or follows the density profile. Relativistic beaming causes the observer to see only a fraction of the fireball around the line-of-sight and as we consider the early afterglow phase, we do not have to consider the jet break (this occurs at much later times) making the spherical model a good approximation. We considered the simple case of line-of-sight emission, however it has been shown that for rising afterglow evolution, high latitude emission does not vary the appearance of the afterglow (Granot et al. 1999), such that omitting this effect from our study will not affect the results.

We first investigate how the early afterglow evolution depends on the initial conditions with a homogeneous density profile (this includes a numerical resolution convergence test), followed by investigating the effect of non-uniform outflow density. Most observed GRBs are found to be in the intermediate reverse shock regime (e.g. $\xi \sim 1$). For this reason we consider how the rising index behaves for homogeneous shell cases with $\xi = 0.5, 1$ and 2. Taking $E = 10^{52}$ ergs, $\Delta = 6 \times 10^{11}$ cm corresponding to

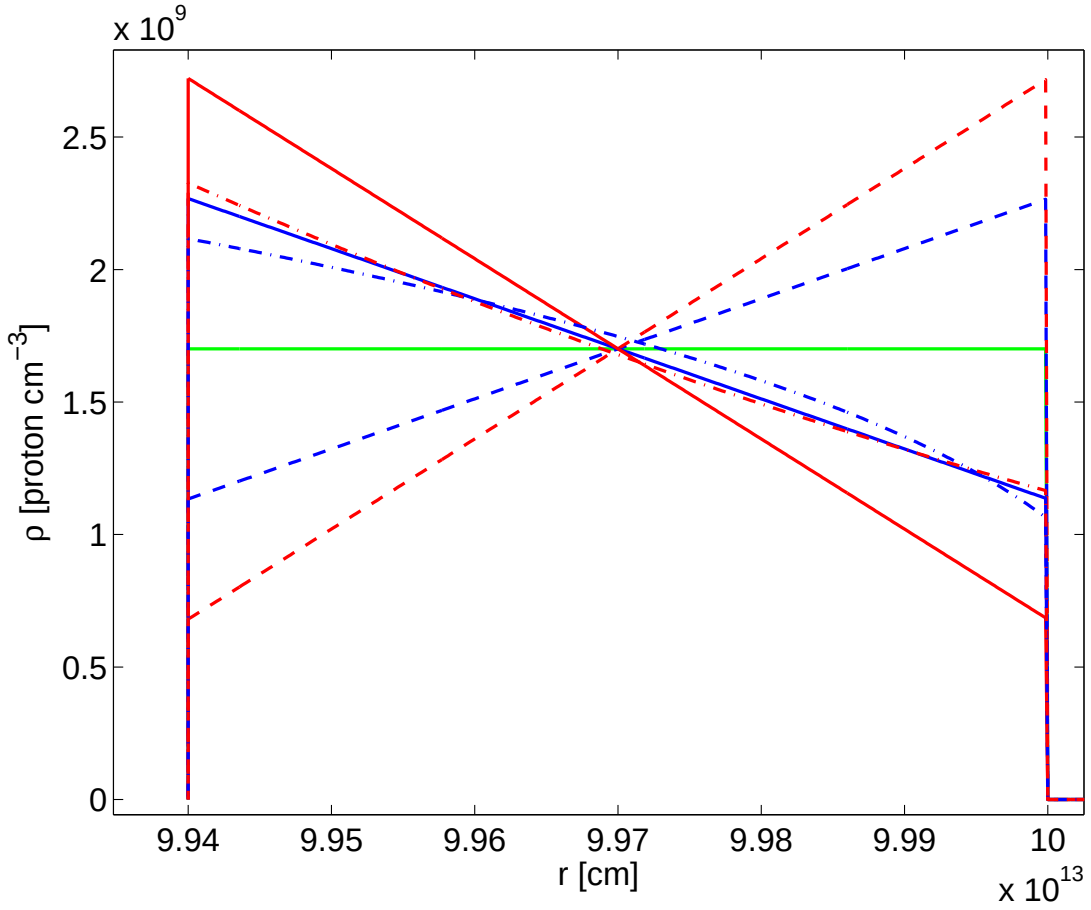

Figure 4.1: This figure shows the density profiles used as initial conditions in the numerical simulations. In solid we see the IH linear ($n = 1$) density with a density difference of 2 (blue) and 4 (red), the same colour code is used for the OH linear density as dashed lines. For comparison in green is the homogeneous density profile for $\xi = 1$, the dot-dashed line represents the varying power index n for the IH case with a density contrast of 2, with red for $n = 3$ and blue for $n = 1/3$. The same ejecta mass, shell width are assumed for all cases.

$\Gamma_0 = 384, 228$ and 136 respectively. We then consider the influence of a slight perturbation to the simple homogeneous density model with $\xi = 1$. For a linear profile ($n = 1$) we fixed the density contrast (ρ_Δ/ρ_0 or ρ_0/ρ_Δ for IH and OH cases respectively) to 2 and 4. To test the influence of the power index n we also consider $n = 3$ and $1/3$ for the $\rho_\Delta/\rho_0 = 2$ IH case. For all density perturbations we consider the case with $\xi = 1$. In Figure 4.1 we show the initial density profile for the $\xi = 1$ simulations.

4.4 Results

To calculate the afterglow for the reverse and forward shock regions we treat each mesh in the Lagrangian simulation as a single fluid element that starts emitting photons after being heated by a shock wave. Each photon is emitted from the inner boundary of each cell neglecting the size of the fluid element. We calculate the flux emitted by each shocked element using its hydrodynamic properties to estimate synchrotron flux according to Sari et al. (1998). Assuming that the flux of each element evolves linearly between numerical time steps we calculate the energy emitted over a given lab time and deposit this across the equivalent observer time and accumulate the flux in this manner for every shocked mesh (see Harrison & Kobayashi 2013 for the details). As we are investigating the temporal profile of the afterglow, the precise values of microphysical parameters ϵ_e and ϵ_B does not affect our results. The forward and reverse shock emission follow the same constraint presented in Section 4.2.2 such that $\nu_{obs} > \nu_m$ in the slow cooling regime, this condition applies to most optical GRB afterglows. All afterglows are normalised relative to the peak flux and location of the $\xi = 1$ homogeneous shell case. In the very early forward and reverse shock afterglows there is a point when the flux sharply rises before settling onto the measured smooth rising portion. This sharp rise is a numerical error associated with the first cells in the simulation being shocked and are therefore inaccurate representations as the resolution is not sufficient to track the shock at very early phases. This emission will be ignored and the resolved emission used based on numerical convergence test.

Previous numerical studies of forward and reverse shock emission are carried out in

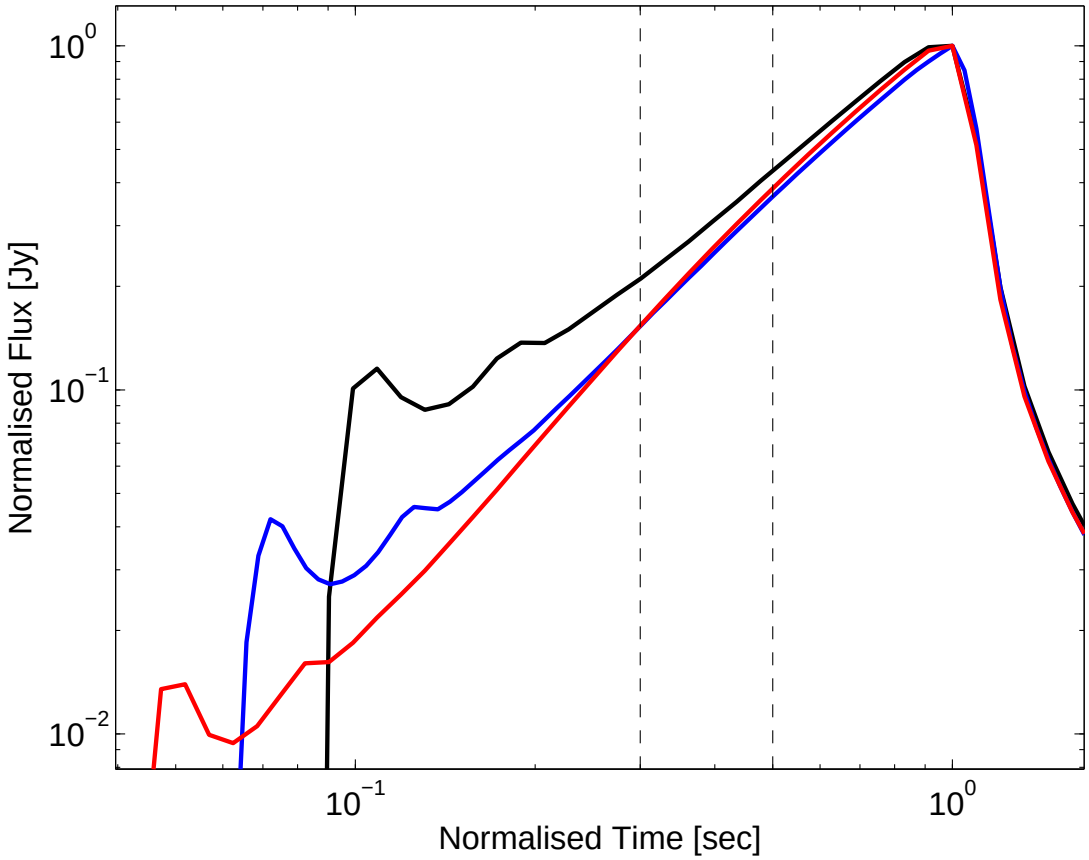

Figure 4.2: Normalised reverse shock emission for $\xi = 1$ case with different numerical resolutions (black for 600 cells, blue for 1200 cells and red for 2400 cells). The dashed lines represent the locations of $t/t_p = 0.3$ and $t/t_p = 0.5$.

the decay phase after reverse shock crossing (e.g. Kobayashi & Sari 2000). As we are interested in the pre-deceleration phase we require higher resolution to properly track the location of the reverse and forward shock fronts. By considering three different resolutions, 600, 1200 and 2400 meshes for complete evolution (200, 400 and 800 cells assigned for the ejecta), the numerical convergence can be tested based on the afterglow appearance (see Figure 4.2). We see convergence between 1200 and 2400 mesh resolution when $t/t_p > 0.3$, with earlier times being unresolved in the 1200 mesh simulation. Using low resolution (e.g. 600 meshes) causes the rising afterglow to appear shallower due to the lower number of meshes in the shocked region. For this study we consider a resolution of 1200 calculating afterglow rising indices for $0.5 < t/t_p < 1$ (see dashed lines Figure 4.2) using the least squares method. We will state a rising index to one decimal place as this was the accuracy that GRBs have been measured (Melandri et al. 2010).

First let us consider how varying ξ between 0.5 and 2 can affect the rising index of the reverse and forward shock component for a homogeneous outflow. In Figure 4.3 we show the reverse shock emission for the $\xi = 0.5, 1$ and 2 cases (blue, green and red respectively), normalised relative to the afterglow peak for $\xi = 1$ case, with rising indices of $\alpha_{rs} \sim 0.9, 1.4$ and 2.3 respectively. Rising index is calculated by performing a least squares fit to the numerical afterglow between the limits $0.5 < t/t_p < 1$. Figure 4.4 shows the same figure for the forward shock component with rising indices $\alpha_{fs} \sim 0.5, 0.7$ and 1.2. The dashed lines in all plots represent the evolution achieved by integrating our model described in Section 4.2, taking an outflow with homogeneous density and match with the numerical result. We have considered the case where $\hat{p} = 2.3$ and these values could vary by $\pm 20\%$, if $\hat{p}$ changes by ± 0.5. In the relativistic limit the expected peak time is $t_p = \Delta/c$ (20 seconds for our simulations) and the Newtonian limit $t_p = l/c\Gamma_0^{8/3}$ with a smooth evolution between the two for the Intermediate regime, which is why the afterglow peaks for $\xi = 0.5$ and 2 are offset in Figures 4.3 and 4.4.

The subsequent models have the same initial conditions as the $\xi = 1$ case with a gradient in the density profile. For the IH case ($\rho_\Delta > \rho_0$) we investigate the influence

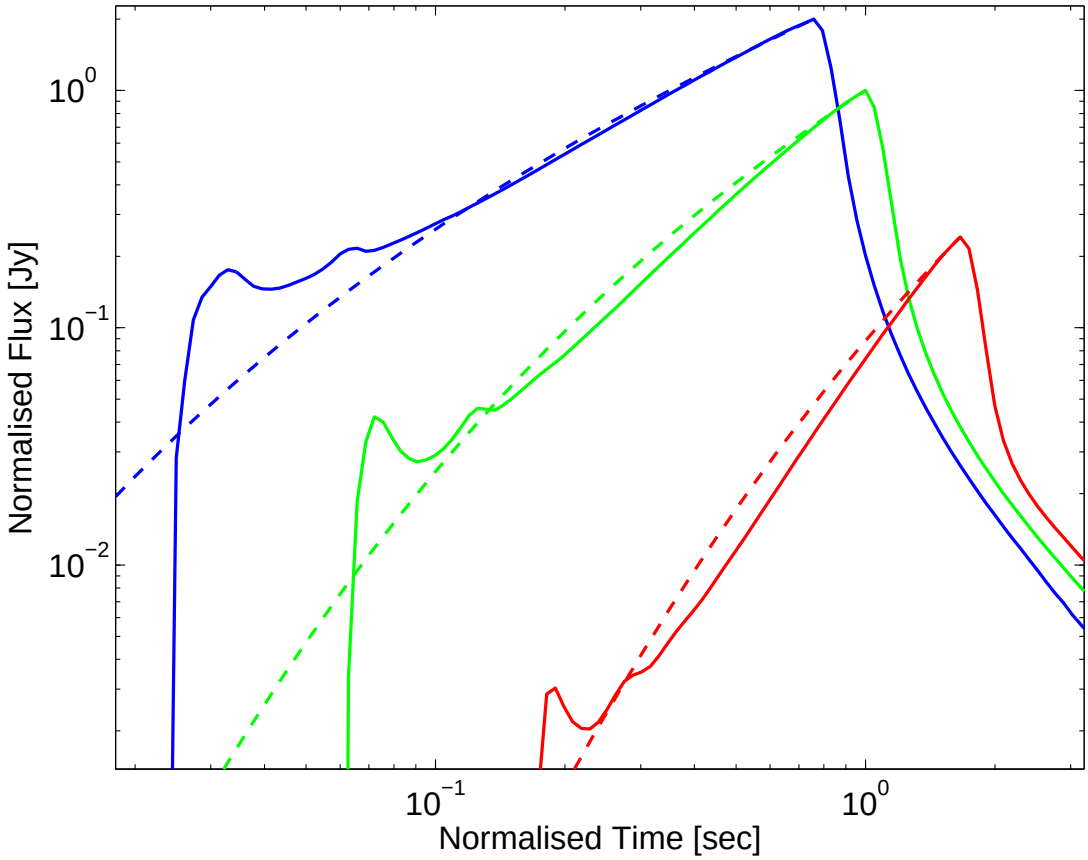

Figure 4.3: Normalised reverse shock light curves for $\xi = 0.5, 1$ and 2 cases (blue, green and red respectively), along with model predictions for pre-peak evolution (dashed lines). In all light curve plots we normalise relative to the peak time and flux of the $\xi = 1$ case.

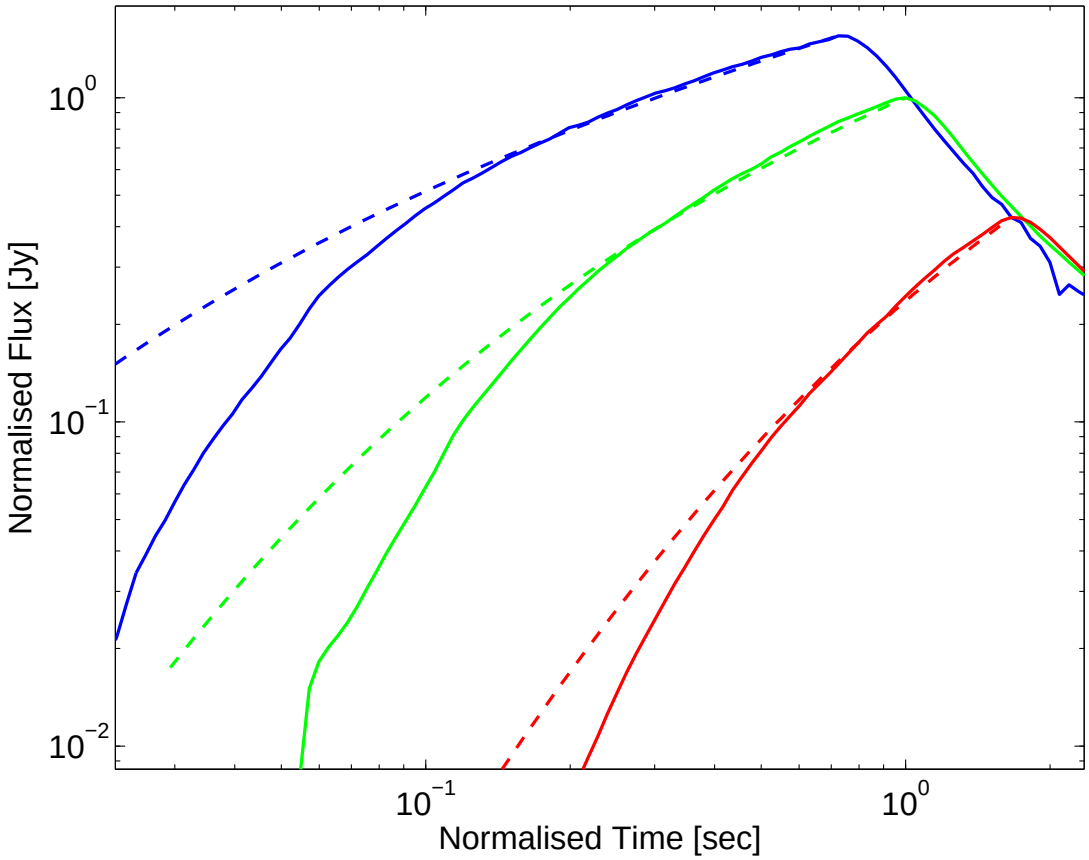

Figure 4.4: Same as Figure 4.3, except for forward shock emission.

on reverse shock emission for two density contrasts (see Figure 4.5). In these cases the density profile is linear (i.e. $n = 1$) and we find that increasing the density contrast to $\rho_\Delta/\rho_0 = 2$ and 4 causes the rising index to steepen from $\alpha_{rs} \sim 1.4$ to $\alpha_{rs} \sim 1.8$ and 1.9 respectively. The dashed line shows the analytical estimate is in good agreement with the numerical simulations. The cause of the steepening is because more of the outflows mass is associated with the inner region, and as the reverse shock encounters more mass (compared to the homogeneous case) the flux emitted increases causing the steeper index. By considering the forward shock emission we see the rising index increasing from $\alpha_{fs} = 0.7$ to 1.1 and 1.4 as we progress from the homogeneous outflow to a density contrast of $\rho_\Delta/\rho_0 = 2$ and 4 respectively. This shows that increasing ρ_Δ/ρ_0 to 4 for an inhomogeneous $\xi = 1$ gives index similar to the homogeneous $\xi = 2$ case. Still considering the IH case taking $\rho_\Delta/\rho_0 = 2$, we vary the power index n in Equation 4.1 to investigate the dependence on the density inhomogeneity shape. By considering a rising index of $n = 3$ and $1/3$ we see a change from the linear case of $+0.1$ and-0.1 respectively with a maximum deviation in flux along the rising portion of 6% indicating that n has no significance at low density contrasts.

In Figure 4.6 we show the result of the OH case where the reverse shock encounters an ever decreasing density. We consider a linear profile ($n = 1$ in Equation B.1) with two density contrasts similar to the IH case, $\rho_0/\rho_\Delta = 2$ and 4. The rising portion of the afterglow is made shallower to $\alpha_{rs} \sim 1$ and 0.9 for the density contrast 2 and 4 cases respectively. Again the analytical model (presented in appendix B) shows good agreement with the numerical simulations and we see the peak moving to earlier times as the density difference is increased. As most of the shell mass is associated with a smaller portion of the ejecta, and the reverse shock crosses this region before crossing the shell, causing the peak to move towards earlier times. Again, a similar evolution is seen in the forward shock emission with the peak flux location becoming rounded and moving to earlier times ($t_p < T_{90}$). The rising index softens from $\alpha_{fs} \sim 0.7$ to 0.5 for homogeneous to increasing density contrast.

For all cases the numerical simulation (solid lines) rising index and the model light curves (dashed lines) gave consistent answers to the accuracy presented here (one dec-

imal place) over the same temporal range. All numbers quoted in the above text come from the numerical simulation least squares fit although the model predictions give the same values to one decimal place.

4.5 Comparison with Previous Work

We aim to reconcile the result presented by Melandri et al. (2010), with the apparent finding that the rising index of afterglow emission is not correlated with the dimensionless parameter ξ (see Figure 4.7). From standard theory we expect the forward (reverse) shock emission to rise as $\alpha = 3(6)$ for homogeneous thin shell and $0.5(0.5)$ thick shell regime respectively. It has been shown to behave as a smooth function of ξ between these two limits (Nakar & Piran 2004), predicting a positive correlation. We use $\xi \sim 5^{1/2}\sqrt{t_p/T_{90} - 1}$ to estimate ξ ensuring that if $t_p \lesssim T_{90}$ then $\xi = 1$ (Harrison & Kobayashi 2013). Given that the rising component is detected the peak time could be well constrained however the assumption that $T_{90} \sim \Delta/c$ could lead to uncertainties in ξ as shown by Virgili et al. (2013) with prolonged central engine activity being masked due to instrumental detection limits. Alternatively one might consider that the outflow has velocity inhomogeneities at the leading edge (giving rise to the prompt emission) and a tail of emission with homogeneous velocity giving no further prompt emission making $T_{90} < \Delta/c$. These uncertainties indicate that ξ could be smaller such that the predicted rising index can be shallower. We could assume that all events in Melandri et al. (2010) are in the intermediate regime, and that this uncertainty reduces high ξ events to the intermediate case. In order to achieve this we require that the $\xi > 1$ have underestimated shell width by on average a factor of 20, $\bar{T}_{90} = 20\bar{\Delta}/c$. This factor seems unrealistically large for the error associated with this estimate. We can then discuss these events in terms of our numerical simulations. The observed rising indices vary in the range $0.3 < \alpha < 4$ ($1 < \xi < 10$ with $2/3$ of the GRBs having $\xi < 5$) with a single outlier at $\alpha \sim 9$, see Figure 4.7. The outlier is possibly associated with prompt optical flaring, which is expected to be very steep and the afterglow rise itself should be shallower. Omitted from this figure are two data points from Melandri et al.

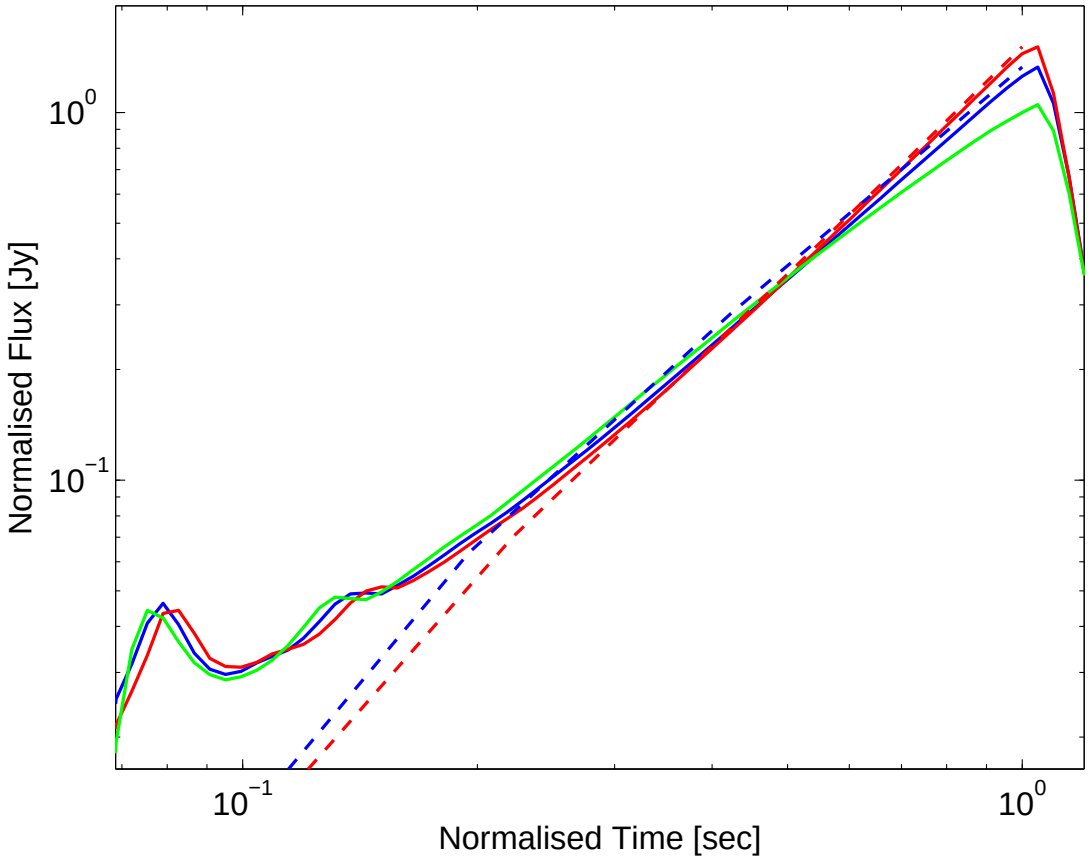

Figure 4.5: Reverse shock afterglow for the IH case with $\xi = 1$ and $n = 1$ (linear density gradient). For comparison in green we see the homogeneous case and in blue the density difference of 2 and in red the difference of 4. The dashed line represents the model predictions.

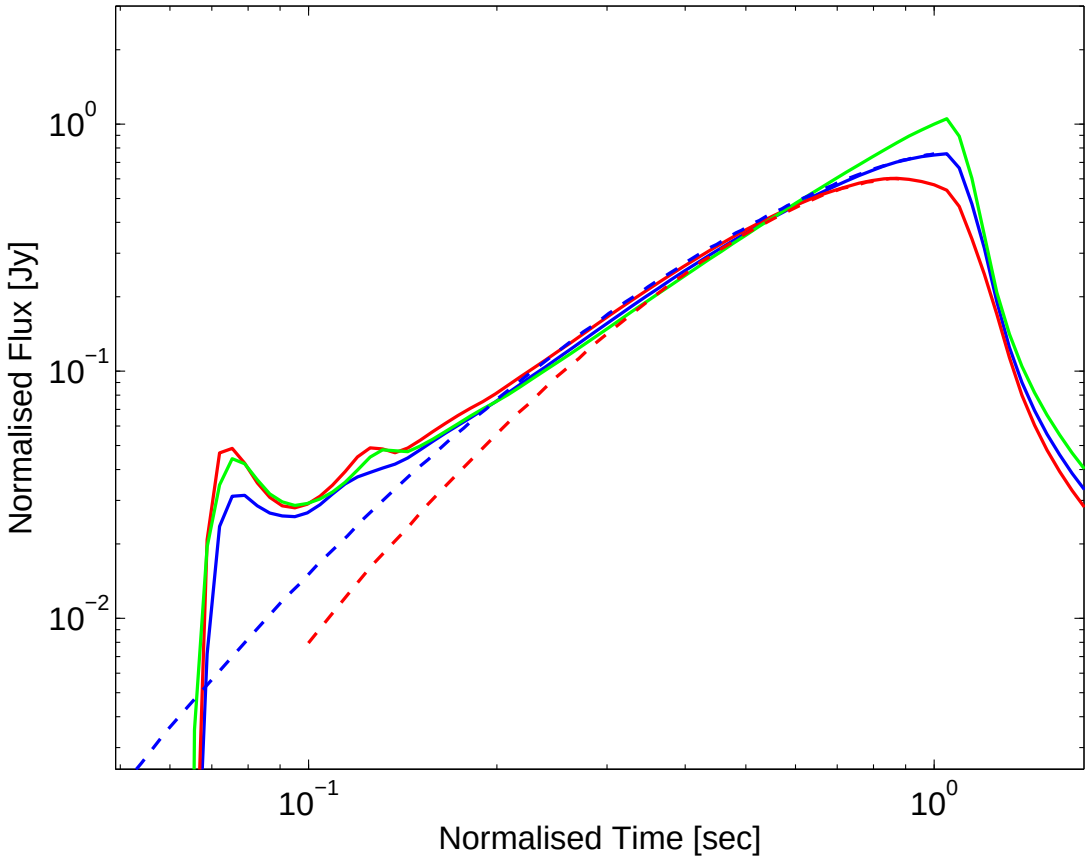

Figure 4.6: Here we have the same set up as Figure 4.5 considering the OH cases.

(2010) as they have very high ξ values not typical of GRBs (one point associated with an X-ray flash) and therefore not pertinent to this study. A similar result was detected by Panaitescu & Vestrand (2008) as early peak afterglows tended to have steeper rising indices when compared to afterglows which peak at later times. If we consider the emission as reverse shock in origin then the pre-peak rising index could vary as $\alpha_{rise} = 0.5 - 6$ (Kobayashi 2000; Nakar & Piran 2004) as we go from the thick to thin shell estimates with $\alpha_{rs} \sim 1.3$ corresponding to $\xi = 1$ (according to our model and simulations). Varying ξ between 0.5 and 2 changes the rising index by $\sim \pm 0.7$ which is not large enough to account for the steep rises observed (Melandri et al. 2010; Panaitescu & Vestrand 2008). Instead we considered a small perturbation to the density profile of the ejecta. We consider IH and OH density cases (see Equations 4.1 and B.1), and investigate small variations across the shell. By considering that the density contrast for the IH and OH cases increases by up to a factor of 4, we observe a rising index that varies between $\alpha_{rs} \sim 0.8 - 2$. If the emission is forward shock in origin then the early rising index (pre-deceleration) can vary between $\alpha_{fs} = 0.5 - 3$ for homogeneous thick to thin shell cases respectively, with typical $\xi = 1$ GRBs rising with $\alpha_{fs} \sim 0.7$. Changing ξ by a factor of 2 can change the rising index by $\sim \pm 0.3$. We have shown that the forward shock emission is influenced by an inhomogeneous density profile, similar to the reverse shock, and changing $\rho_\Delta/\rho_0(\rho_0/\rho_\Delta)$ up to 4 changes the rising index by $\alpha_{fs} \sim 1.4(0.5)$ for IH (OH) cases. Late time forward shock emission could rise with a shallow index $\alpha_{fs} \sim 0.5$ and be in the thin shell regime if the observational frequency is located below the typical frequency (ν_m). Then the peak is due to the passage of the typical frequency across the observational band (Sari et al. 1998). This could be distinguished from the deceleration peak as its location would vary at different frequencies.

This result is not extreme enough to increase the ring index to values of $\alpha_{rise} \sim 4$ observed by Melandri et al. (2010) as even considering a small density perturbation at different ξ we expect the rising index is not sufficiently changed to explain Figure 4.7. In order to increase the density influence and reverse/forward shock evolution further we must increase the inner and outer edge density contrast. If ρ_Δ/ρ_0 is very large the

result becomes independent of the density ratio and becomes a function of the power index n, see Section 4.2.3. The solution for this case can be analytically solved in the thick and thin shell extremes, with a semi-analytical approach required for intermediate regimes. Figure 4.8 shows the result for three reverse shock cases, thick shell (red), thin shell (blue) and intermediate $\xi = 1$ case (black). When estimating the thin shell rising index we assume spreading with $\Delta \sim R$. This result shows how the rising index is expected to evolve with n for the three cases and for fixed n the rising index is expected to vary smoothly between the two limits (thin and thick shell). Discounting the $\alpha \sim 9$ case in figure 4.7, we observe a roughly flat distribution in rising index with a typical value of $\bar{\alpha} \sim 2$ corresponds to a coincidence at $n \sim 5/4$ (almost linear with a large density contrast between inner and outer boundaries of the shell). This however is true if all the rising index were given by reverse shock emission. For forward shock emission we would expect the density profile to influence the rising portion only in the relativistic to intermediate regime. When in the Newtonian regime the evolution is independent of outflow density and the afterglow should rise as t^3.

4.6 Conclusions

Within this chapter we have presented a new analytical approach to create GRB afterglows when considering an ejecta with a density gradient. This model was then tested using numerical simulations, with the analytical and numerical results having good agreement in the rising index of the forward and reverse shock emission. We have shown that a slight density gradient for an intermediate regime GRB ($\xi = 1$) could be equivalent to changing ξ by a factor of 2. However, when comparing with Melandri et al (2010) we note that a small density gradient is insufficient to vary the theoretical rising index sufficiently to match the observed values. It is possible to match the range of rising index by considering a large density contrast between the inner and outer shell boundaries such that the afterglow depends on n alone.

Our result indicates that it is possible to get a small scatter in the rising index of GRB afterglow by considering variation in the initial conditions (ξ) and a slight variation in

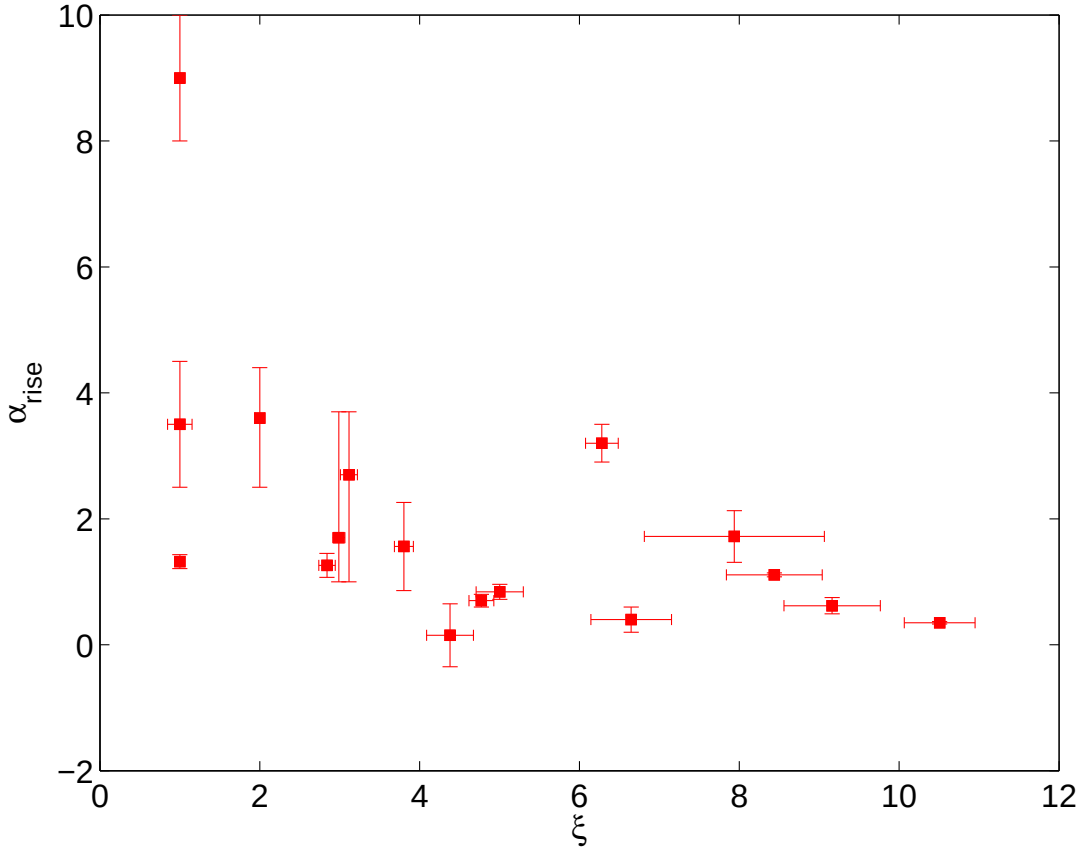

Figure 4.7: Here we show the data collected by Melandri et al. (2010) showing rising index α_{rise} as a function of ξ.

the density profile of the outflows (ρ_4). There are uncertainties in modelling these two variables, as changing ξ by a factor of 2 from unity is equivalent to having a density difference between the inner and outer edge of the shell equal to 4. This however is only sufficient to raise the rising index of the afterglow to $\alpha_{rise} \sim 2$ and in order to achieve steeper values we must consider that there is a large density difference. If we were to consider a large density difference between the inner and outer region and a high power law profile ($n > 1$), then essentially most of the mass associated with the shell will be confined to a small region at the head or tail of the shell. At this point the model would break down as the shell can now be considered as a narrower outflow with the same mass which would increase ξ and make the rising index steeper. The structure of this narrow shell would have to be redetermined. In this case the afterglow rising index may match the observation but the profile inferred by the density structure would not match that of the gamma-ray emission as the shell width would be much smaller than the observed T_{90}.

We assume that the outflow has a homogeneous profile in velocity space throughout this work, however Uhm et al (2012) investigated the afterglow dependence on the velocity structure of the outflow and found that the velocity influences the deceleration phase. This causes late time re-brightening and prolonging reverse shock emission, but does not affect the pre-peak afterglow evolution as the rising index remains constant. A recent study by Vlasis et al. (2011) investigated the optical signature that arises when a shell collides with a decelerating blast wave. The sharp profile of this shell causes a optical flare at later times due to the deceleration of the shell.

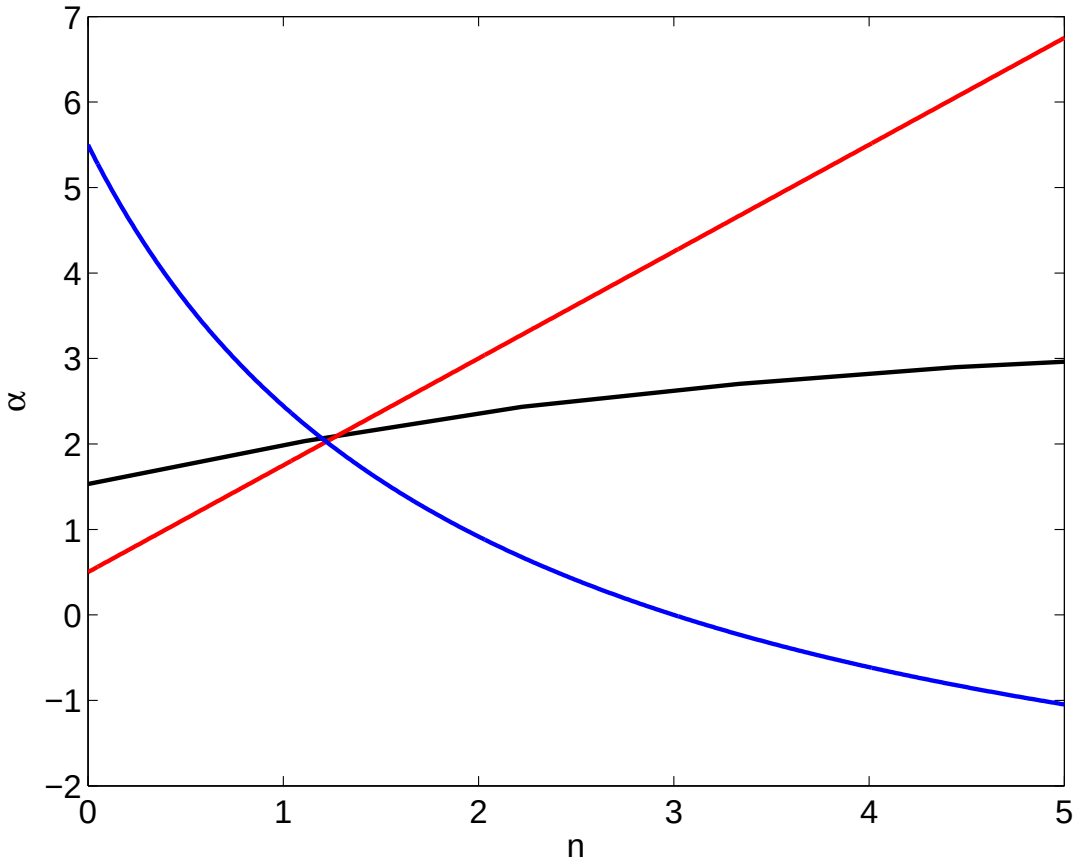

Figure 4.8: We show the rising index as a function of n for the thick and thin (red and blue respectively) shell cases when considering the limiting regime for IH case (see Equation 4.6). In black we show the intermediate $\xi = 1$ result based on numerical integration of Equation 4.6.

Chapter 5

Conclusions

Within this thesis we have tackled issues related to the early afterglow phase associated with GRBs, focusing on the optical regime. By using numerical simulations we have improved analytical estimates for afterglow emission when considering the relative strength of the reverse shock to forward shock components, in terms of magnetisation. We also consider how the profile of the GRB outflow can influence the very early afterglow.

Using numerical simulations we studied how to improve the magnetisation estimate for GRB afterglows based on the discovery that, for typical GRBs ($\xi \sim 1$), the standard reverse shock estimate overpredicts the flux (Nakar & Piran 2004). We found that this led to an underestimate of the magnetisation degree by a factor of $10 - 100$ compared to previous estimates (Zhang et al. 2003; Gomboc et al. 2006). We used our numerical result to improve the existing framework by applying corrective factors as a function of ξ. The main cause to this underestimate comes from the difficulty in defining the reverse shock temperature when spreading is effective, resulting in an overall lower typical frequency and maximal flux for the reverse shock component. This partially answers the lack of "optical flash" GRBs, as we only get an optical tracer of the reverse shock if the magnetisation degree is high, as typically this emission should peak at lower frequencies.

We then expanded on the magnetisation model for an ISM type environment to account

for the ejecta propagating through a wind medium. We found that by considering a wind medium, the magnetisation degree is smaller when compared to an ISM estimate by a significant amount. As the maximal forward shock flux in the wind model decays with time as $t^{1/2}$, and at later times we expect a weaker forward shock emission relative to the reverse shock component when compared to the ISM case (as the maximal flux is constant). This instantly requires a smaller magnetisation to boost the reverse shock component as the predicted forward shock emission is much weaker. By applying both wind and ISM magnetisation estimates to 10 GRBs exhibiting a reverse shock component, we find that 5 of the 10 cases can be described by the ISM model with the nature of the other cases being unclear. Based on typical values of the fraction of energy stored in the magnetic fields, it is likely all cases can be well described assuming a baryonic jet.

The evolution of the reverse shock component primarily depends on the initial conditions of the system (E_{iso}, Δ_0 and Γ_0) along with the density profile of the fireball. We showed how the initial conditions can affect the early appearance of afterglow emission (pre-peak), which can be well described by a semi-analytical solution of reverse shock evolution. Here we also consider how a simple first order perturbation to the standard homogeneous density profile assumption can change the afterglow profile. We show that the density profile assumed can drastically change the rising index of early emission. This has consequences for the interpretation of early detections (Melandri et al. 2010), as the rising index is degenerate. The density profile does however lend itself to explaining irregular afterglow behaviour (e.g. afterglow emission peaking before the end of the prompt phase).

Within the internal shock model we expect the collision of shells to create density irregularities that will affect the reverse shock evolution, making the simple top hat distribution inappropriate for observed GRBs. We plan to take this work one step further by simulating the collision of shells and the resulting afterglow as the reverse shock crosses density irregularities. Through this method it is possible to directly link afterglow features with prompt emission features (Nakar & Piran 2005; Maxham & Zhang 2009; Vlasis et al. 2011).

Appendix A

Hydrodynamical Code

A.1 Introduction

We use a spherical relativistic Lagrangian code based on the Godunov method, including an exact Riemann solver to evaluate the complete evolution of a fireball (Kobayashi et al., 1999). As we are only interested on the early afterglow, which occurs well before the jet break, a spherical model is a good approximation.

A.2 Spherical System

Let us consider a conical section of some spherical outflow. The energy, momentum and mass of the j-th cell are

$$E_j = \Omega_0 \int_{r_{j-1/2}}^{r_{j+1/2}} \gamma^2 (e + \beta^2 p) r^2 dr \tag{A.1}$$

$$P_j = \Omega_1 \int_{r_{j-1/2}}^{r_{j+1/2}} \gamma^2 (e + p) \beta r^2 dr \tag{A.2}$$

$$M_j = \Omega_0 \int_{r_{j-1/2}}^{r_{j+1/2}} \gamma \rho r^2 dr \tag{A.3}$$

where $\Omega_0 = 2\pi(1 - cos\,\theta_0)$ and $\Omega_1 = \frac{\pi}{2}(1 - cos\,2\theta_0)$. Ω_1 accounts for the vector nature of the momentum with an integrated projected factor. As the flow is radial Ω_0 and Ω_1 are constant. So we use the hydrodynamic quantities to show conserved quantities at a time step, and when we recover these quantities in the subsequent time step, we normalise the cell's qualities by the same solid angles.

For motion of a relativistic fluid the conservation laws are

$$\nabla_\mu(\rho u^\mu) = 0, \;\; \nabla_\nu T^{\mu\nu} = 0 \tag{A.4}$$

here u_i is the four velocity and $T^{\mu\nu}$ is the stress-energy tensor ($\mu, \nu = 0, 1, 2, 3$).

$$T^{\mu\nu} = (e + p)u^\mu u^\nu + pg^{\mu\nu} \tag{A.5}$$

Using the above equations we find that

$$\frac{dE_j}{dt} = (\beta pS)_{j-1/2} - (\beta pS)_{j+1/2} \tag{A.6}$$

$$\frac{dP_j}{dt} = \left(\frac{\Omega_1}{\Omega_0}\right)[(pS)_{j-1/2} - (pS)_{j+1/2}] \int_{r_{j-1/2}}^{r_{f+1/2}} 2rpdr \tag{A.7}$$

$$\frac{dM_j}{dt} = 0 \tag{A.8}$$

A.2.1 Time Evolution

Each cell is assumed to be homogeneous at each time step.

$$E_j(t_i) = \gamma_j^2(e_j + \beta_j^2 p_j)V_j \tag{A.9}$$

$$P_j(t_i) = \gamma_j^2(e_j + p_j)\beta_j V_j \tag{A.10}$$

$$M_i = \gamma_j \rho_j V_j = const. \tag{A.11}$$

with $V_j(t_i) = 1/3(r_{j+1/2}^3 - r_{j-1/2}^3)$ being the volume of cell j. As the code will span many orders of magnitude during a simulation (e.g. 10^{11} cm to 10^{17} cm) and the width

of each cell could become much smaller than the fireball then $r_{j+1/2}$ and $r_{j-1/2}$ could be practically the same. As computers can only handle finite values we introduce a new variable ($c = 1$) to avoid cancellation error.

$$x_{j+1/2}(t_i) = r_{j+1/2}(t_i) - t_i \tag{A.12}$$

As the cells travel relativistically $x_{j+1/2}$ changes slower than $r_{j+1/2}$. At each time step Δt we have $\Delta x = (\beta_* - 1)\Delta t = -\Delta t \gamma_*^{-2}(1 + \beta_*)^{-1}$ where β_* and γ_* are the velocity and Lorentz factor of the boundary at t_i.

The volume of our jth-cell is given by

$$V_j = \frac{1}{3}(x_{j+1/2}^3 - x_{j-1/2}^3) + t(x_{j+1/2}^2 - x_{j-1/2}^2) + t^2(x_{j+1/2} - x_{j-1/2}) \tag{A.13}$$

During $\Delta t = t_{i+1} - t_i$ the cell obtains energy

$$\begin{aligned} \Delta E_j &= \int_{t_i}^{t_{i+1}} \frac{dE_j}{dt} dt & \text{(A.14)} \\ &= \int_{t_i}^{t_{i+1}} \left\{ (\beta p S)_{j-1/2} - (\beta p S)_{j+1/2} \right\} dt & \text{(A.15)} \\ &= \left\{ (\beta p \bar{S})_{j-1/2} - (\beta p \bar{S})_{j+1/2} \right\} \Delta t & \text{(A.16)} \end{aligned}$$

$$\bar{S}_{j+1/2} \equiv r_{j+1/2}^2(t_i) + r_{j+1/2}(t_i)\beta_{j+1/2}\Delta t + \frac{\beta_{j+1/2}^2}{3}\Delta t^2 \tag{A.17}$$

The boundary velocity and pressure are assumed to be constant during Δt. The additional momentum is given by

$$\begin{aligned} \Delta P_j &= \int_{t_i}^{t_{i+1}} \frac{dP_j}{dt} dt & \text{(A.18)} \\ &= \left\{ (p\bar{S})_{j-1/2} - (p\bar{S})_{j+1/2} \right\} \Delta t + \int_{t_i}^{t_i + \Delta t} dt \int_{r_{j-1/2}}^{r_{j+1/2}} dr 2rp & \text{(A.19)} \end{aligned}$$

When considering a planar source the second term is ignored as it relates to a geomet-

rical source term. The internal pressure can be approximated as a constant p_{ave}[1].

$$\Delta P_j = \left\{(p_{j-1/2} - p_{ave})\bar{S}_{j-1/2} - (p_{j+1/2} - p_{ave})\bar{S}_{j+1/2}\right\}\Delta t \tag{A.20}$$

If we assume that the hydrodynamic quantities in each cell are homogeneous at t_{i+1}

$$\gamma_j^2(e_j + \beta_j^2 p_j) = \frac{E_j(t_i) + \Delta E}{V_j(t_{i+1})} \tag{A.21}$$

$$\gamma_j^2(e_j + p_j)\beta_j = \frac{P_j(t_i) + \Delta P}{V_j(t_{i+1})} \tag{A.22}$$

$$\gamma_j \rho_j = \frac{M_j}{V_j(t_{i+1})} \tag{A.23}$$

where the left hand side quantities are defined at t_{i+1}.

Time Step

From initial data it is possible to find exact solution by piecing the solution of each Riemann problem defined by the jump at each boundary. The time step is set by the fact that waves from the Riemann problems do not cross the cell. If this is violated then r may change as neighbouring Reimann problem waves cross into the cell.

A.2.2 Sound Velocity

The first law of thermodynamics states $d\varepsilon = -pdV + Tds$, where ε is the specific internal energy, $V = 1/\rho$ is the specific volume and s is the specific entropy. For an adiabatic change ($ds = 0$) we obtain $d\varepsilon = pdV = pd\rho/\rho^2$. Combining with the differential form of the equation of state ($\varepsilon - 1 = p/\left\{(\hat{\gamma} - 1)\rho\right\}$),

$$d\varepsilon = \frac{1}{\hat{\gamma} - 1}\left(\frac{dp}{\rho} - \frac{p}{\rho^2}d\rho\right) \tag{A.24}$$

$$\frac{dp}{p} = \hat{\gamma}\frac{d\rho}{\rho} \tag{A.25}$$

[1] An analytical Riemann solver is used to find velocity and pressure at boundaries.

equivalent to $p/\rho^{\hat{\gamma}} = const$. The sound velocity in the local fluid frame is given by

$$c_s = c\sqrt{\left(\frac{\partial p}{\partial e}\right)_{ad}} \tag{A.26}$$

The suffix ad indicates this derivation is for an adiabatic process. This differs from the non-relativistic form as mass density is replaced by e/c^2. Using equation of state ($p = (\hat{\gamma} - 1)(e - \rho)$) and the adiabatic relation $d(p/\rho^{\hat{\gamma}}) = 0$, we obtain

$$c_s = c\sqrt{\frac{\hat{\gamma}}{\frac{\hat{\gamma}}{\hat{\gamma}-1} + \frac{\rho}{p}}} = \sqrt{\frac{\hat{\gamma}p}{w}} \tag{A.27}$$

with $w = e + p$.

Sound Crossing

A fluid cell has velocity β in the lab frame and a sound wave propagates with speed c_s in local fluid frame. The sound velocity in the lab frame is given by,

$$s_{\pm} = \frac{\pm c_s + \beta}{1 \pm c_s\beta} \tag{A.28}$$

with $+(-)$ representing the sound wave moving in positive (negative) r direction in local fluid frame. The crossing time for a cell is

$$dt_+ = \frac{dx}{s_+ - \beta} \; or \; dt_- = \frac{dx}{\beta - s_-} \tag{A.29}$$

dt_+ corresponds to a sound wave propagating from the left boundary to the right with dt_- being the opposite direction.

$$dt_{\pm} = \left(\frac{dx}{c_s}\right)(1 \pm x_s\beta)\gamma^2 \, dt_s \equiv \left(\frac{dx}{c_s}\right)(1 - c_s|\beta|)\gamma^2 \tag{A.30}$$

Within the code we have the factor dx/c_s replaced with $dx/(c_s + v_{min})$ to prevent divergence in the case of a cold flow (e.g. $v_{min} = 10^{-20}$).

Boundary Crossing

If the left boundary propagates quicker than the right boundary then the possibility exists that they could collide within $dt_b = dx/(\beta_{*L} - \beta_{*R})$. We evaluate dt_s and dt_b for every cell and the minimum value gives the time step $\Delta t = t_{i+1} + t_i$. At each step dt is not increased significantly and is limited to 1% in the code.

As the shock waves must propagate quicker than a sound wave, then $dt < dt_s/3$ is required. The sound velocity in a hot fluid $c_s \sim c\sqrt{3}$ is (similar to the speed of light and is) appropriate for our study. A better treatment is required for a cold flow as the sound waves are much slower than the shocks. The Lorentz factor of the shock is given in terms of the Lorentz factor at the contact discontinuity

$$\Gamma = \frac{(\gamma_* + 1)^{1/2}(4\gamma_* - 1)}{(8\gamma_* + 10)^{1/2}} < \sqrt{2}\gamma_* \tag{A.31}$$

for $\hat{\gamma} = 4/3$. As we assume that the cells do not change significantly ($dt < dt_b/10$), our code should be able to handle a cold flow.

A.3 Shock Waves in Relativistic Fluid Dynamics

It is necessary for us to allow for relativistic effects for the case described above. We apply the relativistic equations for fluid dynamics. By considering a surface of discontinuity at rest with a flow perpendicular to it. The continuity equations for this system are

$$[n^x] = [nu^x] = 0, \tag{A.32}$$

$$[T^{xx}] = \left[w(u^x)^2 + p\right] = 0 \tag{A.33}$$

$$c\left[T^{0x}\right] = c\left[wu_0u^x\right] = 0 \tag{A.34}$$

denoting particle number, momentum and energy flux density conservations. Here we use $[nu^x] \equiv n_1u_1^x - n_2u_2^x$ with 1 and 2 denoting either side of the discontinuity surface. With $w = e + p$ is the heat function per unit volume , u^x 4-velocity vector and T^{xx}

being the energy momentum 4-tensor. After substitution of the 4-velocity component,

$$v_1\gamma_1/V_1 = v_2\gamma_2/V_2 \equiv j \tag{A.35}$$

$$w_1 v_1^2\gamma_1^2/c^2 + p_1 = w_2 v_2^2\gamma_2^2/c^2 + p_2 \tag{A.36}$$

$$w_1 v_1 \gamma_1^2 = w_2 v_2 \gamma_2^2 \tag{A.37}$$

here $\gamma = 1/\sqrt{1 - v_1^2/c^2}$ and $V = 1/n$.

Using Equations A.35 and A.36,

$$j^2 = \frac{(p_2 - p_1)c^2}{(w_1 V_1^2 - w_2 V_2^2)} \tag{A.38}$$

and A.35 allows us to re-write A.37

$$w_1^2 V_1^2 \gamma_1^2 = w_2^2 V_2^2 \gamma_2^2 \tag{A.39}$$

By substitution of Equations A.38 into A.35 we arrive at the relativistic version of the shock adiabatic (known as the Taub adiabatic)

$$w_1^2 V_1^2 - w_2^2 V_2^2 + (p_2 - p_1)(w_1 V_1^2 + w_2 V_2^2) = 0 \tag{A.40}$$

Through Equations A.36 and A.37 we get expressions for the flow velocity on either side of the discontinuity surface

$$\frac{v_1}{c} = \sqrt{\frac{(p_2 - p_1)(e_2 + p_1)}{(e_2 - e_1)(e_1 + p_2)}}, \quad \frac{v_2}{c} = \sqrt{\frac{(p_2 - p_1)(e_1 + p_2)}{(e_2 - e_1)(e_2 + p_1)}} \tag{A.41}$$

The relative velocity of flow on either side of our surface is given by the relativistic velocity addition rule

$$v_{12} = \frac{v_1 - v_2}{1 - v_1 v_2/c^2} = c\sqrt{\frac{(p_2 - p_1)(e_2 - e_1)}{(e_1 + p_2)(e_2 + p_1)}} \tag{A.42}$$

In the non-relativistic limit, we have $e \simeq mc^2 n = mc^2/V$, and neglecting p in comparison with e. If we consider the ultra-relativistic equation of state ($p = e/3$),

$$\frac{v_1}{c} = \sqrt{\frac{3e_2 + e_1}{3(3e_1 + e_2)}}, \quad \frac{v_2}{c} = \sqrt{\frac{3e_1 + e_2}{3(3e_2 + e_1)}} \tag{A.43}$$

We can plot the relativistic shock adiabatic in pV plane, with the variables as wV^2 and pc^2. j^2 gives the slope of the chord connecting two initial points on different adiabatics (see Figure A.1).

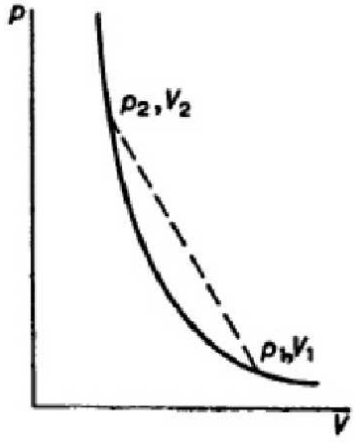

Figure A.1: The shock adiabatic (image taken from Landau & Lifshitz 1987). (p_1, V_1) corresponds to the state of flow in front of shock (initial point).

The extension of the relativistic regime for fluid dynamics can be found in Martí & Müller (1994; 1996).

Appendix B

Outer High Density

Here we consider the case where the reverse shock is encountering an ever decreasing density (OH CASE) such that the leading (outer) shell edge has larger density than the inner edge $\rho_0 > \rho_\Delta$. The density profile is given by

$$\rho_4 = \rho_N \left[\frac{(1-r)}{\delta} + 1\right]^n \quad (n > 0) \tag{B.1}$$

We will consider the case with $n = 1$ for simplicity. In this case $\delta = \Delta[(\rho_0/\rho_\Delta - 1]^{-1}$ assuming a fixed density ratio between inner and outer shell boundaries and $\kappa = \Delta(\Delta + \Delta^2/2\delta)^{-1}$ by equating the total mass to $E/\Gamma_0^2 c^2$. The definition for ξ changes in the final term of Equation 4.2 for this case

$$\xi^3 = \frac{24x^4}{\kappa(1-x)^2(2+3x+2x^2)} \left(\frac{(\Delta - r)}{\delta} + 1\right)^{-1} \left(\frac{R}{R_\Delta}\right)^2 \tag{B.2}$$

The general function of r on R is given by integrating Equation **??**,

$$r = \Delta - \delta \left[\left\{\frac{R^2}{\mu}\left(\frac{27\Delta}{16\kappa l^3 \delta^2}\right)^{1/2} + (\Delta/\delta + 1)^{3/2}\right\}^{2/3} - 1\right], \tag{B.3}$$

It follows that the shock crossing radius is given by

$$R_{\Delta} = \left[\mu^{-1} \left(\frac{16 \kappa l^3 \delta^2}{27 \Delta} \right)^{1/2} ((\Delta/\delta + 1)^{3/2} - 1) \right]^{1/2} \tag{B.4}$$

Finally to allow calculation of the pre-deceleration afterglow the number of electrons in the shocked region is

$$N_e = \frac{EA}{\Gamma_0^2 \Delta} \left(r(1 + \Delta/\delta) - \frac{r^2}{2\delta} \right) \tag{B.5}$$

The afterglow can then be calculated using the same assumptions set out for the IH case (e.g. $\nu_m < \nu_{obs}$).

Bibliography

Akerlof, C., Balsano, R., Barthelmy, S., et al. 1999, Nature, 398, 400

Arnold, D. M., Steele, I. A., Bates, S. D., Mottram, C. J., & Smith, R. J. 2012, Proc. SPIE, 8446,

Band, D., Matteson, J., Ford, L., et al. 1993, ApJ, 413, 281

Barkov, M. V., & Komissarov, S. S. 2008, International Journal of Modern Physics D, 17, 1669

Bersier, D., Stanek, K. Z., Winn, J. N., et al. 2003, ApJ, 584, L43

Björnsson, G., Gudmundsson, E. H., & Jóhannesson, G. 2004, ApJ, 615, L77

Blandford, R. D., & McKee, C. F. 1976, Physics of Fluids, 19, 1130

Blandford, R. D., & Znajek, R. L. 1977, MNRAS, 179, 433

Cavallo, G., & Rees, M. J. 1978, MNRAS, 183, 359

Cenko, S. B., Frail, D. A., Harrison, F. A., et al. 2010, ApJ, 711, 641

Chevalier, R. A., & Li, Z.-Y. 2000, ApJ, 536, 195

Coburn, W., & Boggs, S. E. 2003, Nature, 423, 415

Covino, S., Campana, S., Conciatore, M. L., et al. 2010, A&A, 521, A53

Dai, Z. G., & Lu, T. 1998, MNRAS, 298, 87

Daigne, F., & Mochkovitch, R. 1998, MNRAS, 296, 275

de Ugarte Postigo, A., Castro-Tirado, A. J., Gorosabel, J., et al. 2005, A&A, 443, 841

de Ugarte Postigo, A., Jakobsson, P., Malesani, D., et al. 2009, GRB Coordinates Network, 8766, 1

Drenkhahn, G., & Spruit, H. C. 2002, A&A, 391, 1141

Fan, Y.-Z., Dai, Z.-G., Huang, Y.-F., & Lu, T. 2002, ChJAA, 2, 449

Fenimore, E. E., & Ramirez-Ruiz, E. 2000, arXiv:astro-ph/0004176

Fermi, E. 1954, ApJ, 119, 1

Fermi, E. 1949, Physical Review, 75, 1169

Fox, D. W., Price, P. A., Soderberg, A. M., et al. 2003, ApJ, 586, L5

Fruchter, A. S., Pian, E., Thorsett, S. E., et al. 1998, Gamma-Ray Bursts, 4th Hunstville Symposium, 428, 509

Götz, D., Laurent, P., Lebrun, F., Daigne, F., & Bošnjak, Ž. 2009, ApJ, 695, L208

Gao, W.-H. 2011, Research in Astronomy and Astrophysics, 11, 1317

Gendre, B., Klotz, A., Palazzi, E., et al. 2010, MNRAS, 405, 2372

Gendre, B., Stratta, G., Atteia, J. L., et al. 2013, ApJ, 766, 30

Genet, F., Daigne, F., & Mochkovitch, R. 2007, MNRAS, 381, 732

Ghisellini, G., Ghirlanda, G., Nava, L., & Celotti, A. 2010, MNRAS, 403, 926

Ghisellini, G., & Lazzati, D. 1999, MNRAS, 309, L7

Giannios, D., Mimica, P., & Aloy, M. A. 2008, A&A, 478, 747

Giannios, D., & Spruit, H. C. 2006, A&A, 450, 887

Goldreich, P., & Julian, W. H. 1970, ApJ, 160, 971

Gomboc, A., Kobayashi, S., Guidorzi, C., et al. 2008, ApJ, 687, 443

Gomboc, A., Kobayashi, S., Mundell, C. G., et al. 2009, American Institute of Physics Conference Series, 1133, 145

Goodman, J. 1986, ApJ, 308, L47

Granot, J. 2012, MNRAS, 421, 2442

Granot, J. 2003, ApJ, 596, L17

Granot, J., Komissarov, S. S., & Spitkovsky, A. 2011, MNRAS, 411, 1323

Granot, J., & Kumar, P. 2003, ApJ, 591, 1086

Granot, J., Piran, T., & Sari, R. 1999, ApJ, 513, 679

Granot, J., & Taylor, G. B. 2005, ApJ, 625, 263

Gruzinov, A. 1999, ApJ, 525, L29

Gruzinov, A., & Waxman, E. 1999, ApJ, 511, 852

Harrison, R., & Kobayashi, S. 2013, ApJ, 772, 101

Jin, Z.-P., Covino, S., Della Valle, M., et al. 2013, ApJ, 774, 114

Kalemci, E., Boggs, S. E., Kouveliotou, C., Finger, M., & Baring, M. G. 2007, ApJS, 169, 75

Kann, D. A. 2008, American Institute of Physics Conference Series, 1065, 85

Klebesadel, R. W., Strong, I. B., & Olson, R. A. 1973, ApJ, 182, L85

Klotz, A., Gendre, B., Stratta, G., et al. 2006, A&A, 451, L39

Kobayashi, S. 2000, ApJ, 545, 807

Kobayashi, S., Piran, T., & Sari, R. 1999, ApJ, 513, 669

Kobayashi, S., Piran, T., & Sari, R. 1997, ApJ, 490, 92

Kobayashi, S., & Sari, R. 2001, ApJ, 551, 934

Kobayashi, S., & Sari, R. 2000, ApJ, 542, 819

Kobayashi, S., & Zhang, B. 2007, ApJ, 655, 973

Kobayashi, S., & Zhang, B. 2003, ApJ, 597, 455

Kobayashi, S., & Zhang, B. 2003, ApJ, 582, L75

Komissarov, S. S., Vlahakis, N., Königl, A., & Barkov, M. V. 2009, MNRAS, 394, 1182

Kouveliotou, C., Meegan, C. A., Fishman, G. J., et al. 1993, ApJ, 413, L101

Kulkarni, S. R., Djorgovski, S. G., Odewahn, S. C., et al. 1999, Nature, 398, 389

Kulkarni, S. R., Frail, D. A., Sari, R., et al. 1999, ApJ, 522, L97

Kumar, P., & Barniol Duran, R. 2009, MNRAS, 400, L75

Kumar, P. 1999, ApJ, 523, L113

Kumar, P., & Panaitescu, A. 2003, MNRAS, 346, 905

Kumar, P., & Panaitescu, A. 2000, ApJ, 541, L51

Landau, L. D., & Lifshitz, E. M. 1959, Course of theoretical physics, Oxford: Pergamon Press, 1959,

Laskar, T., Berger, E., Zauderer, B. A., et al. 2013, arXiv:1305.2453

Lazzati, D., & Perna, R. 2007, MNRAS, 375, L46

Leventis, K., van der Horst, A. J., van Eerten, H. J., & Wijers, R. A. M. J. 2013, MNRAS, 431, 1026

Li, W., Filippenko, A. V., Chornock, R., & Jha, S. 2003, ApJ, 586, L9

Li, Z.-Y., & Chevalier, R. A. 2003, ApJ, 589, L69

Liang, E.-W., Li, L., Gao, H., et al. 2013, ApJ, 774, 13

Lithwick, Y., & Sari, R. 2001, ApJ, 555, 540

Lyutikov, M. 2011, MNRAS, 411, 422

Lyutikov, M. 2003, MNRAS, 346, 540

Mészáros, P. 2002, ARA&A, 40, 137

Mészáros, P., & Rees, M. J. 1999, MNRAS, 306, L39

Maxham, A., & Zhang, B. 2009, ApJ, 707, 1623

McGlynn, S., Clark, D. J., Dean, A. J., et al. 2007, A&A, 466, 895

McKinney, J. C. 2006, MNRAS, 368, 1561

McKinney, J. C., & Blandford, R. D. 2009, MNRAS, 394, L126

Medvedev, M. V., & Loeb, A. 1999, ApJ, 526, 697

Meegan, C. A., Fishman, G. J., Wilson, R. B., et al. 1992, Nature, 355, 143

Melandri, A., Kobayashi, S., Mundell, C. G., et al. 2010, ApJ, 723, 1331

Melandri, A., Mundell, C. G., Kobayashi, S., et al. 2008, ApJ, 686, 1209

Meszaros, P., & Rees, M. J. 1997, ApJ, 476, 232

Meszaros, P., & Rees, M. J. 1992, ApJ, 397, 570

Meszaros, P., Rees, M. J., & Wijers, R. A. M. J. 1998, ApJ, 499, 301

Michel, F. C. 1969, ApJ, 158, 727

Mimica, P., Giannios, D., & Aloy, M. A. 2010, MNRAS, 407, 2501

Mimica, P., Giannios, D., & Aloy, M. A. 2009, A&A, 494, 879

Mochkovitch, R., Hernanz, M., Isern, J., & Martin, X. 1993, Nature, 361, 236

Mundell, C. G., Steele, I. A., Smith, R. J., et al. 2007, Science, 315, 1822

Nakar, E., & Piran, T. 2005, NCimC, 28, 431

Nakar, E., & Piran, T. 2005, ApJ, 619, L147

Nakar, E., & Piran, T. 2004, MNRAS, 353, 647

Nakar, E., Piran, T., & Waxman, E. 2003, JCAP, 10, 5

Narayan, R., Paczynski, B., & Piran, T. 1992, ApJ, 395, L83

Narayan, R., Piran, T., & Kumar, P. 2001, ApJ, 557, 949

Nishikawa, K.-I., Hardee, P., Richardson, G., et al. 2003, ApJ, 595, 555

Nousek, J. A., Kouveliotou, C., Grupe, D., et al. 2006, ApJ, 642, 389

Nysewander, M. C., Reichart, D. E., Park, H.-S., et al. 2006, ApJ, 651, 994

O'Brien, P. T., Willingale, R., Osborne, J., et al. 2006, ApJ, 647, 1213

Oates, S. R., Page, M. J., Schady, P., et al. 2011, MNRAS, 412, 561

Paczynski, B. 1986, ApJ, 308, L43

Paczynski, B. 1991, AcA, 41, 257

Panaitescu, A., & Kumar, P. 2004, MNRAS, 353, 511

Panaitescu, A., & Kumar, P. 2003, ApJ, 592, 390

Panaitescu, A., & Kumar, P. 2002, ApJ, 571, 779

Panaitescu, A., & Kumar, P. 2000, ApJ, 543, 66

Panaitescu, A., Spada, M., & Mészáros, P. 1999, ApJ, 522, L105

Panaitescu, A., & Vestrand, W. T. 2008, MNRAS, 387, 497

Pandey, S. B., Castro-Tirado, A. J., Jelínek, M., et al. 2009, A&A, 504, 45

Pandey, S. B., Sahu, D. K., Resmi, L., et al. 2003, Bulletin of the Astronomical Society of India, 31, 19

Piran, T. 1999, PhR, 314, 575

Piran, T. 2004, Reviews of Modern Physics, 76, 1143

Piran, T. 1995, arXiv:astro-ph/9507114

Piran, T., Sari, R., & Zou, Y.-C. 2009, MNRAS, 393, 1107

Racusin, J. L., Karpov, S. V., Sokolowski, M., et al. 2008, Nature, 455, 183

Racusin, J. L., Liang, E. W., Burrows, D. N., et al. 2009, ApJ, 698, 43

Rees, M. J., & Meszaros, P. 1998, ApJ, 496, L1

Rees, M. J., & Meszaros, P. 1994, ApJ, 430, L93

Rhoads, J. E. 1999, ApJ, 525, 737

Rossi, E. M., Lazzati, D., Salmonson, J. D., & Ghisellini, G. 2004, MNRAS, 354, 86

Ruderman, M. 1975, Seventh Texas Symposium on Relativistic Astrophysics, 262, 164

Rutledge, R. E., & Fox, D. B. 2004, MNRAS, 350, 1288

Rybicki, G. B., & Lightman, A. P. 1979, New York, Wiley-Interscience, 1979. 393 p.,

Sari, R. 1999, ApJ, 524, L43

Sari, R. 1997, ApJ, 489, L37

Sari, R., & Esin, A. A. 2001, ApJ, 548, 787

Sari, R., & Mészáros, P. 2000, ApJ, 535, L33

Sari, R., Narayan, R., & Piran, T. 1996, ApJ, 473, 204

Sari, R., & Piran, T. 1999, ApJ, 520, 641

Sari, R., & Piran, T. 1999, ApJ, 517, L109

Sari, R., & Piran, T. 1997, MNRAS, 287, 110

Sari, R., & Piran, T. 1995, ApJ, 455, L143

Sari, R., Piran, T., & Halpern, J. P. 1999, ApJ, 519, L17

Sari, R., Piran, T., & Narayan, R. 1998, ApJ, 497, L17

Shemi, A., & Piran, T. 1990, ApJ, 365, L55

Soderberg, A. M., & Ramirez-Ruiz, E. 2002, MNRAS, 330, L24

Spada, M., Panaitescu, A., & Mészáros, P. 2000, ApJ, 537, 824

Spitkovsky, A. 2008, ApJ, 682, L5

Steele, I. A., Bates, S. D., Carter, D., et al. 2006, Proc. SPIE, 6269,

Steele, I. A., Bates, S. D., Guidorzi, C., et al. 2010, Proc. SPIE, 7735,

Steele, I. A., Mundell, C. G., Smith, R. J., Kobayashi, S., & Guidorzi, C. 2009, Nature, 462, 767

Stratta, G., Pozanenko, A., Atteia, J.-L., et al. 2009, A&A, 503, 783

Tchekhovskoy, A., McKinney, J. C., & Narayan, R. 2008, MNRAS, 388, 551

Totani, T. 1997, ApJ, 486, L71

Uehara, T., Toma, K., Kawabata, K. S., et al. 2012, ApJ, 752, L6

Uhm, Z. L., Zhang, B., Hascoët, R., et al. 2012, ApJ, 761, 147

Vestrand, W. T., Wozniak, P. R., Wren, J. A., et al. 2005, Nature, 435, 178

Virgili, F. J., Mundell, C. G., Pal'shin, V., et al. 2013, arXiv:1310.0313

Vlasis, A., van Eerten, H. J., Meliani, Z., & Keppens, R. 2011, MNRAS, 415, 279

Wiersema, K., Curran, P. A., Krühler, T., et al. 2012, MNRAS, 426, 2

Wigger, C., Hajdas, W., Arzner, K., Güdel, M., & Zehnder, A. 2004, ApJ, 613, 1088

Wijers, R. A. M. J., Bloom, J. S., Bagla, J. S., & Natarajan, P. 1998, MNRAS, 294, L13

Willis, D. R., Barlow, E. J., Bird, A. J., et al. 2005, A&A, 439, 245

Woosley, S. E. 1993, ApJ, 405, 273

Yi, S.-X., Wu, X.-F., & Dai, Z.-G. 2013, arXiv:1308.6095

Yonetoku, D., Murakami, T., Gunji, S., et al. 2011, ApJ, 743, L30

Zeh, A., Klose, S., & Kann, D. A. 2006, ApJ, 637, 889

Zhang, B., Kobayashi, S., & Mészáros, P. 2003, ApJ, 595, 950

Zhang, B., & Mészáros, P. 2004, International Journal of Modern Physics A, 19, 2385

Zhang, B., & Pe'er, A. 2009, ApJ, 700, L65

Zhang, B., & Yan, H. 2011, ApJ, 726, 90

Zhang, F.-W., Shao, L., Yan, J.-Z., & Wei, D.-M. 2012, ApJ, 750, 88